Catalysis Science & Technology

ROYAL SOCIETY OF CHEMISTRY

REVIEW

View Article Online
View Journal | View Issue

Cite this: *Catal. Sci. Technol.*, 2025, **15**, 6318

Synthesis strategies of supported bimetallic catalysts for hydrogenation reactions: review and outlook

An Zhang, Kun Yang, Arthur Prewette and Weijian Diao *

Received 23rd May 2025,
Accepted 28th August 2025

DOI: 10.1039/d5cy00622h

rsc.li/catalysis

Catalytic hydrogenation reactions are widely utilized in the petrochemical and fine chemical industries. However, the complex activation mechanisms and adsorption/desorption behaviors associated with specific reactions impose stringent requirements on catalyst composition and structure. Supported bimetallic catalysts, which benefit from metal–metal and metal–support interactions, exhibit significant research value and potential for hydrogenation reactions. Building upon this foundation, a systematic comparison, analysis, and summary of the design strategies and synthetic methodologies of bimetallic systems can serve as a valuable reference for the development of novel catalytic materials. This review provides a comprehensive summary of bimetallic catalytic systems applied in various hydrogenation reactions over the past decade, focusing on their synthetic routes. The discussion encompasses nano-catalysts, single-atom catalysts, and the role of supports in enhancing bimetallic systems. Additionally, existing challenges in this research area are discussed, and potential directions for future research are proposed to guide advancements in bimetallic hydrogenation catalysis.

1. Introduction

Fossil fuels have been the basis of human development in past centuries and will continue to play an important role in the world's energy needs, derived fuels, and a vast array of essential petrochemicals in the years to come.[1–3] With the aim of sustainable development, numerous technologies have been developed to maximize the utilization of existing chemical raw materials.[3] Among them, hydrogenation reactions have been deeply investigated and play a vital role in many fields, such as food, chemicals, petrochemicals, and pharmaceuticals.[4] Hydrogenation reactions are so widely used that it has been estimated that up to a quarter of all chemical processes are related to at least one hydrogenation reaction.[5] Based on the nature of the reactants of the hydrogenation process, which are in the gas or liquid phase, these reactions are driven by heterogeneous solid catalysts, which can add hydrogen atoms to unsaturated compounds and transform them into saturated compounds.[4,6] For example, ethylene, a fundamental feedstock in the petrochemical industry, is mainly produced from cracking reactions industrially with a global production capacity of 214 million metric tons as of 2021.[7] However, the conventional process for ethylene production results in product streams with between 0.3–3% acetylene as an impurity, whose presence quickly poisons the Ziegler–Natta catalyst used in the polymerization of ethylene.[8] To purify the ethylene streams, the selective hydrogenation of acetylene is a key process for the production of polymers and fine chemicals.[9] Besides, the production of renewable chemicals, such as methanol, methane, and syngas, through the hydrogenation of carbon dioxide has great potential to decrease the emission of greenhouse gases.[10,11] For example, the reverse water gas shift (RWGS) reaction is considered one of the most promising hydrogenation processes with high potential efficiency.[12] And CO, as a desirable product, is an essential building block for synthetic fuels and oxygenates *via* Fischer–Tropsch or methanol synthesis reactions.[13] However, due to the endothermic nature of RWGS and the kinetic inertness of CO_2, CO_2 conversion in RWGS is being challenged by activating highly stable CO_2 molecules into CO.[14,15] It has been reported that the RWGS reaction requires over 1000 K to achieve 50% conversion of CO_2 under atmospheric pressure. In addition, the methanation process of over-hydrogenation on CO_2 molecules is another challenge that restricts the CO selectivity.[12] Therefore, great efforts have been made to boost the CO_2 conversion rate and CO selectivity in the CO_2 hydrogenation process.

For decades, with the deepening of understanding of the catalytic hydrogenation reaction, investigations have been conducted to improve the performance of heterogeneous catalysts, especially for supported metal catalysts; such investigations involve controlling the size of metal nanoparticles,[16,17] metal particles with specific crystalline

Department of Chemical and Biological Engineering, Villanova University, Villanova, PA 19085, USA. E-mail: Weijian.diao@villanova.edu

facet exposure,[18,19] the effect that different supports have on the catalytic behavior of metallic sites,[20] *etc.* Supported metal catalysts refer to the composites that contain ultra-small metal particles as active surface sites and mostly inert supports for fixing these particles as thermally stable substrates.[6] The types of active metals can generally be used as the basis for classifying supported metal catalysts. For monometallic catalysts, ultimately, the catalytic properties are dependent on the intrinsic activity of the particular metal, despite the availability of the various fine-tuning approaches mentioned above.[18,21] Applications for monometallic catalysts are generally limited to cases when different catalyst properties are desired, especially in case where either untraditional feeds, extreme reaction conditions, or stringent product stream requirements are involved.[18] However, with the addition of secondary (or tertiary) metal, bi(tri)metallic catalysts have attracted much attention because of their prominent catalytic performances in sustainable energy, environment, petrochemical industries, *etc.*[22–26] Take bimetallic systems as an example, the two active metal species can exist in the form of alloys, intermetallic compounds, or as a particulate mixture,[26–28] which provide specific functions or superior catalytic performance to that of their monometallic counterparts.[4,23]

This review aims to discuss the primary methodologies and advancements on synthesis routes of supported bimetallic catalysts for hydrogenation reactions. The first part will give an introduction to the properties of bimetallic catalysts, as well as a detailed discussion on the associated mechanisms. In this part, related bimetallic hydrogenation catalysts will be covered based on the available literature to aid in identifying targets for guiding the synthesis of catalysts. Then, specific synthetic strategies will be discussed in three main parts: controlling particle size, single-atom catalysts, and support effects for hydrogenation catalysts. Following this discussion, a reasonable prospect for the development of bimetallic catalysts will be given based on the comprehensive summary of representative research work in recent years.

2. Bimetallic effects on hydrogenation reactions

For hydrogenation reactions driven by supported bimetallic catalysts, significant effort has been devoted to overcoming three critical challenges: enhancing catalytic activity, modifying selectivity, and improving catalyst stability under specific reaction conditions. From a research perspective, it is critical to build a bridge between catalytic performance and the properties of the catalysts, including composition and structure.[29] Generally, the dramatically enhanced performance of bimetallic catalysts is often caused by one or more co-existing effects,[18] which can be categorized as geometric (or ensemble) effects, electronic (or ligand) effects, and synergistic effects.[18,30,31] As shown in Fig. 1, these effects are intimately related to changes in the physicochemical properties of the catalysts, such as active site dispersion, reactant adsorption strength, and modifications to catalytic reaction pathways.[31] Hence, a comprehensive understanding of these effects is crucial for guiding the rational design and synthesis of bimetallic catalysts.

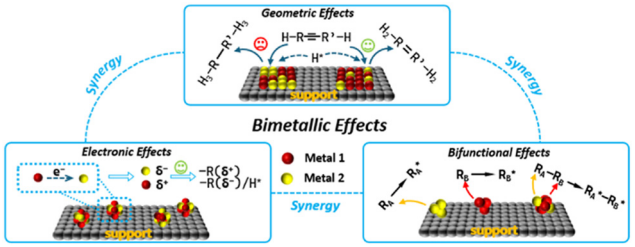

Fig. 1 Schematic representing the synergistic relationship of geometric effects, electronic effects and bifunctional effects.

2.1 Geometric effects

In bimetallic systems, geometric effects are known as the addition of the secondary metal, which can modify the size of the metal's active site ensembles, changing the adsorption geometry, which alters the catalytic selectivity.[18,30] For example, the selective hydrogenation of acetylene converts a triple bond (CH≡CH) into a double bond (CH_2=CH_2). However, as shown in Fig. 2(a), this process suffers from some unfavorable side reactions leading to undesired byproducts such as the over-hydrogenation product of ethane, the reforming product of butadiene, and the polymerization product of green oil (C_{4+}).[32] These side reactions arise from several identified adsorption modes on catalysts (Fig. 2(b) B to F), which lead to undesired reactions through complex hydrogenation pathways because of adjacent active sites on the catalyst surface.[33] The optimal mode of adsorption involves a π-bond interaction between CH≡CH and the catalyst surface (Fig. 2(b) A), allowing the triple bond to be easily activated by active sites, forming ethylene, which desorbs upon π-bond dissociation to prevent over-hydrogenation.[34] Hence, it is reasonable to believe that the selectivity of C_2H_2 hydrogenation can be controlled by adjusting ensemble sizes to affect adsorption modes. As shown in Fig. 2(c–e), Zhou *et al.* reported ~90% selectivity towards C_2H_4 and nearly 100% conversion of C_2H_2 at 60 °C with a PdZn intermetallic nanostructure catalyst containing regularly arranged Pd–Zn–Pd ensembles; this regular arrangement of Pd sites led to the moderate σ-bond between adsorbed C_2H_2 and neighboring Pd sites, as well as the weak π-bond between adsorbed C_2H_2 and single Pd sites.[27] Zhang *et al.* found that the highly separated surface Pd sites by dilution of Ag or Au can lead to high selectivity in C_2H_2 hydrogenation.[34] Likewise, research work in nanoalloy construction,[35,36] atomic site regulation,[37,38] and ultrasmall nanoparticles[39] also reveals the importance of modifying the size of the metal's active site ensembles in hydrogenation reactions.

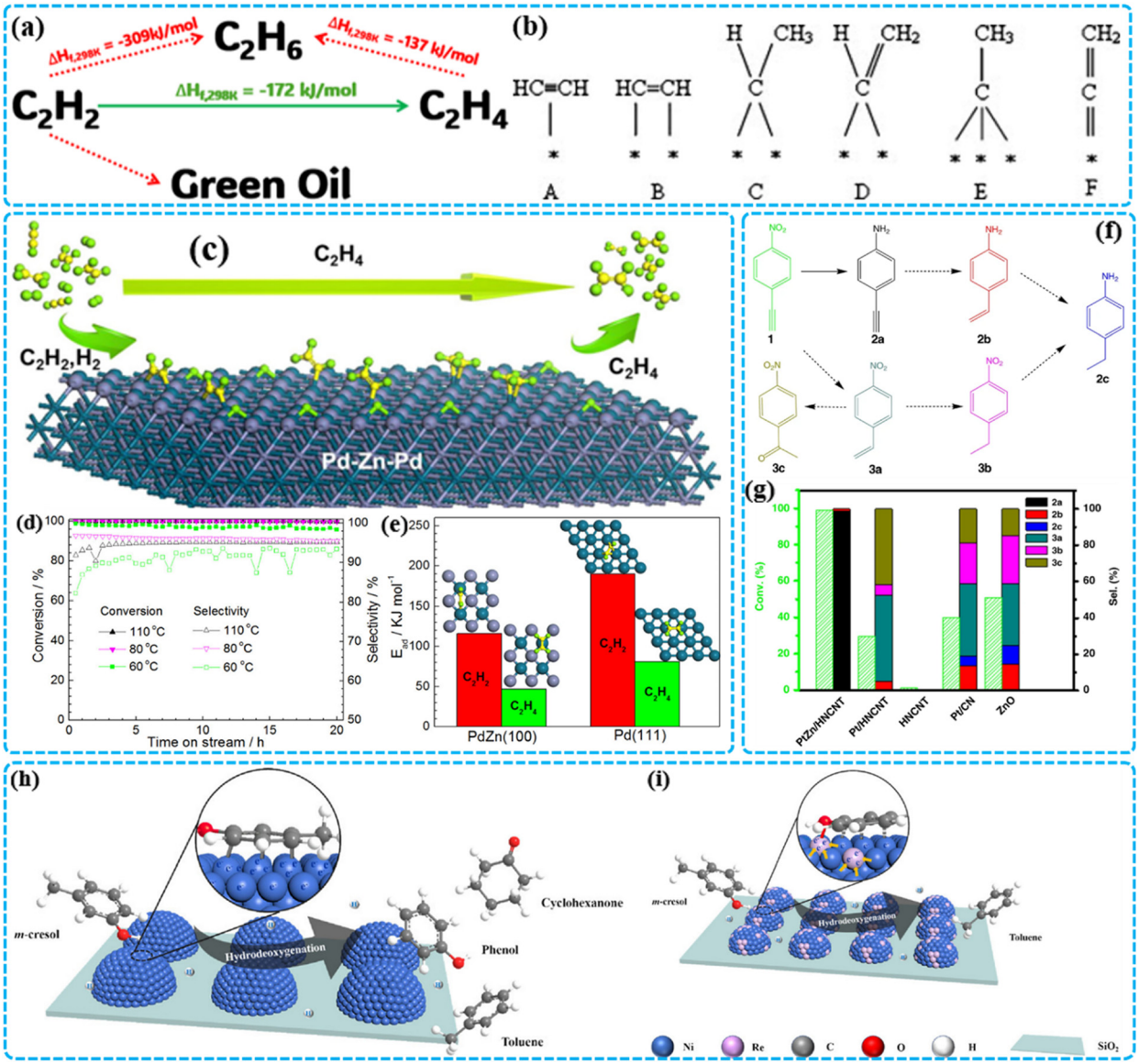

Fig. 2 (a) Schematic of reactions in C_2H_2 hydrogenation; (b) possible adsorption mode of C_2H_2 on active metal sites. A: π-complex; B: di-σ-adsorbed; C: ethylidene; D: vinyl; E: ethylidyne; F: vinylidene; (c) schematic of the PdZn intermetallic nanostructure for selective hydrogenation of C_2H_2; (d) conversion and selectivity with time for selective hydrogenation of C_2H_2 over PdZn; (e) DFT modeling of acetylene and ethylene adsorption on PdZn(100) or Pd(111) surfaces; (f) schematic of reaction pathways in 4-nitrophenylacetylene; (g) conversion and selectivity for selective hydrogenation of 4-nitrophenylacetylene over different Pt-based catalysts; (h and i) the proposed reaction mechanism for *m*-cresol hydrodeoxygenation over Ni/SiO_2 and NiRe/SiO_2 catalysts [panels (a and b) have been reproduced with permission from ref. 33, Copyright 2007, Elsevier. Panels (c–e) have been reproduced with permission from ref. 27, Copyright 2016, American Chemical Society. Panels (f and g) have been reproduced with permission from ref. 41, Copyright 2019, Springer Nature. Panel (h and i) have been reproduced with permission from ref. 31, Copyright 2020, Wiley-VCH].

Geometric effects have also been shown to alter the reaction pathway by optimizing the recognition ability of specific functional groups during hydrogenation reactions.[5] Li *et al.* claimed that the larger Ni ensembles favor the cleavage of C–C bonds in biomass hydrogenolysis, while the smaller Ni ensembles favor the cleavage of C–O bonds.[31] Wang *et al.* also concluded that it is a reasonable strategy to modify the adsorption mode of specific functional groups by changing metallic ensemble size in the selective hydrogenation of cinnamaldehyde.[40] Specifically, in the case of coexisting C=O and C=C groups, it is difficult to control the targeted adsorption between C=O and metal active sites, as the hydrogenation of C=C in cinnamaldehyde is more thermodynamically favorable.[40] To improve C=O adsorption while inhibiting C=C adsorption, Wang *et al.* proposed the introduction of oxyphilic adsorption sites to favor the vertical adsorption mode (C=O) over the parallel adsorption mode (C=C). Fig. 2(f and g) represents research on selective hydrogenation of 4-nitrophenylacetylene, proposing

isolating contiguous Pt atoms and forming Pt–Zn intermetallic nanoparticles to enhance Pt selectivity towards 4-aminophenylacetylene.[41] In contrast to other monometallic catalysts, the Pt–Zn intermetallic surface obtained nearly 100% conversion and selectivity. DFT calculations reveal that the presence of Zn promotes the adsorption of nitro groups and changes the hydrogenation energy barriers from 239 kJ mol^{-1} for the alkynyl group and 117 kJ mol^{-1} for the nitro group in Pt catalysts to 201 kJ mol^{-1} and 114 kJ mol^{-1}, respectively, in PtZn catalysts. Thus, the selective hydrogenation process can be stopped upon the formation of product **2a** (Fig. 2(f)) instead of further over-hydrogenation.[41]

It is worth noting that geometric effects are usually accompanied by electronic effects, working together to improve the catalyst performance.[36,42–45] Fig. 2(h and i) presents the different behaviors between Ni ensembles and NiRe ensembles on *m*-cresol hydrodeoxygenation (HDO).[31] It is obvious that the introduced Re atoms not only act as a separate active site on Ni ensembles, but they also show preferential adsorption with hydroxyl groups rather than the electron-rich benzene ring because of its nature as an electron-rich metal center. However, although the secondary metal always causes a tunable coordination environment on catalyst surfaces, there are some cases in which electronic effects don't play a major role in the performance of the catalyst.[34,35,46]

2.2 Electronic effects

Electronic effects, or ligand effects, are known as modifications to the electronic structure of the active metal species that influence the binding energies of adsorbed species,[31,47,48] which corresponds to improvements in catalytic performance. Compared with the simple geometric factors, the electronic structure of the active metal sites is generally considered to have a bigger impact on catalytic performance.[5,49] For supported bimetallic catalysts, a reasonable explanation for the electronic effects can be attributed to the d-band center theory.[5,50,51] It is generally believed that the combination of two metals with different electronegativity will induce charge transfer from the species with lower electronegativity to the species with higher electronegativity, reducing the d-band center of the former because of its lower electron density.[52–55] Hence, the electronic interaction between active sites and reactants is also reduced, resulting in a decrease in the adsorption energy of the reactants on the surface of the catalyst. Generally, it is beneficial to increase the desorption rate of reactants, intermediates, or products, particularly for some selective hydrogenation reactions. Yao *et al.* reported a Pt–Ni core–shell bimetallic catalyst with a strong Pt(5d)–Ni(3d) coupling effect, resulting in enhanced catalytic stability over the monometallic Pt catalyst.[56] The electron transfer from Ni to Pt by electronic effects affects the catalyst's ability for H_2 activation, as well as enhances the catalytic stability of nitrobenzene hydrogenation and promotes selectivity to *p*-aminophenol as desired products. Li *et al.* reported a $CuNi/ZrO_2$ bimetallic catalyst with 100% conversion of C_2H_2 and 93% selectivity to C_2H_4. The electron transfer from Cu to Ni makes the catalyst superior to most advanced non-noble metal catalysts reported in the literature.[36] Reddy *et al.* also reported a Cu–Ni bimetallic catalyst with a regulated Cu/Ni ratio for the CO_2 hydrogenation reaction.[13] Generally, Ni-based catalysts demonstrate considerable conversion of CO_2 under mild conditions, but are more selective towards CH_4 than CO due to excessive hydrogenation.[57] The optimum Cu–Ni composition shows higher selectivity than the mono Ni catalyst because the introduced Cu can modify the electronic structure of the nickel surface and act as the active site to enhance CO desorption.

Another valuable discussion related to electronic effects is that it can affect the noncovalent electronic interaction between reactants (or reactive intermediates) and metal active sites.[5,58–62] As discussed in the above section, the introduced secondary metal can tune the adsorption orientation of *m*-cresol by altering the electron density. Xu *et al.* reported an electronic regulating effect of a potassium (K) promoter from a reactant activation perspective on CuFe-based catalysts for producing higher alcohols (HAs) from direct CO_2 hydrogenation.[63] The introduced K can not only balance the two modes of CO dissociated activation for providing adequate intermediate species that take part in the coupling reaction, but also selectively inhibits the competitive reaction that is not conducive to the formation of HAs in the coupling reaction. Moreover, for the selective hydrogenation of *p*-chloronitrobenzene (*p*-CNB) to *p*-chloroaniline (*p*-CAN), Xiao *et al.*[64] developed a series of bimetallic catalysts PtM/Al_2O_3 (M = Co, Cu, Ni, Fe, Zn, Ga, and Sn). Among them, $PtCo/Al_2O_3$ and $PtCu/Al_2O_3$ were chosen as the most representative samples as Co has the strongest electronic interaction with Pt that can donate electrons to Pt, while Cu is the only metal that can attract electrons from Pt (Fig. 3(a)). Fig. 3(e and f) reveals that two opposed electronic effects are reflected in completely different behaviors of electronic interaction between reaction intermediates and active sites. These opposing electronic effects are responsible for the high conversion, low *p*-CAN selectivity of $PtCo/Al_2O_3$ and the low conversion, high *p*-CAN selectivity of $PtCu/Al_2O_3$. The electronic effects among Pt, Co, and Cu were also investigated in a trimetallic catalyst, aiming to benefit from the combination of the Pt–Ni and Pt–Cu electronic effects. As shown in Fig. 3(b–d), as the Co/Pt molar ratios increase, the electron transfer from Co to Pt and Cu occurs, optimizing the electronic interactions between the three metals and the functional groups of the reactive intermediate (Fig. 3(g)). It is worth noting that electronic effects of supported active sites can also act as indirect electronic modulations that happen between loaded metals and supports, especially for reducible metal oxides; these modulations are termed

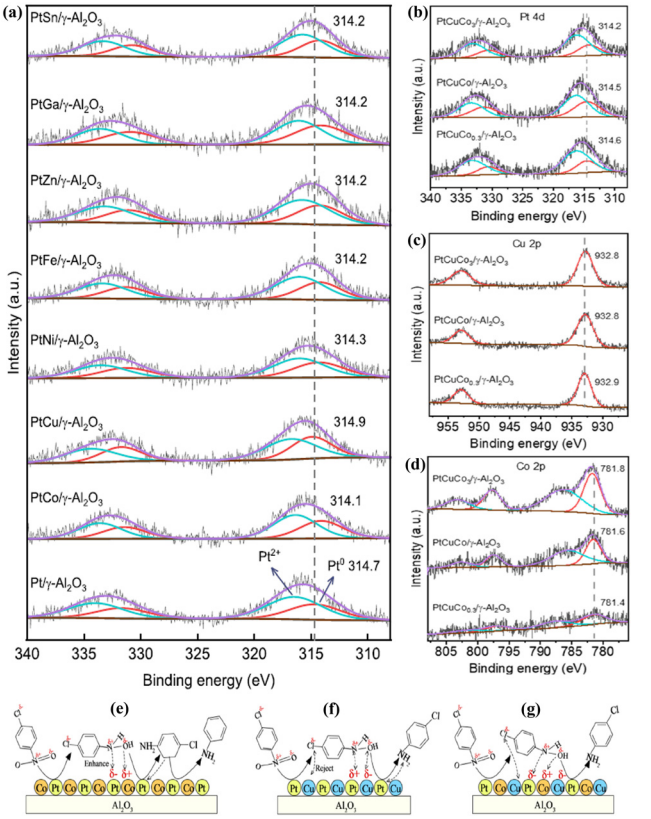

Fig. 3 (a) Pt 4d XPS spectra for PtM/γ-Al_2O_3 catalysts; XPS spectra of (b) Pt 4d, (c) Cu 2p, and (d) Co 2p for PtCuCo$_x$/γ-Al_2O_3 catalysts; proposed mechanism for the selective hydrogenation of *p*-CNB on (e) PtCo/γ-Al_2O_3, (f) PtCu/γ-Al_2O_3, and (g) PtCuCo$_x$/γ-Al_2O_3 catalysts [panels (a–g) have been reproduced with permission from ref. 64, Copyright 2023, Elsevier].

"electronic metal–support interaction" (EMSI). A detailed discussion of this part will be given in section 3.3.

2.3 Bifunctional effects

Bifunctional effects refer to the definition that each active component in bimetallic catalysts shows a distinct function of the corresponding monometallic catalyst simultaneously in catalytic reactions.[18,30] These effects manifest as each metal activating different parts of an adsorbate or, in the case of bimolecular reactions, activating different adsorbates. For example, Han *et al.* explored the catalytic HDO of lignin-derived phenolic compounds over supported Ni–Fe nanoparticles on mesoporous carbon spheres.[65] As shown in Fig. 4(a), the HDO reaction occurs in two sequential steps: the hydrogenation of phenol to cyclohexanol and the following hydrogenolysis of cyclohexanol to cyclohexane.[65] In the Ni–Fe alloy system, in addition to the enhanced adsorption of the intermediate product cyclohexanol by the alloy sites, Fe-related sites are responsible for the adsorption of hydroxyl species, while Ni sites activate H_2. Han *et al.* reported coexisting Co atom sites and Co nanoparticle systems for the HDO and following hydrogenation of aromatic ketones for the production of high-energy-density ring hydrocarbons.[66] Despite being a monometallic catalyst, bifunctionality still occurs due to the presence of distinct single-atom Co sites alongside the Co nanoparticles. Specifically, Co atoms acted as Lewis acid sites to disturb the electron density for activating the C=O/C–OH bonds and aromatic ring, while Co nanoparticles are for H_2 activation (Fig. 4(b)).[66] The research from Fu *et al.* reveals that interfacial bifunctional effects exist in the Cu modified Fe_yMgO_x layered double hydroxide catalysts for the selective hydrogenation of C_2H_2.[67] The bifunctional effects are reflected in the activation of C_2H_2 and H_2 that occurred on interfacial Cu sites; meanwhile, the transferred adsorption of formed C–C intermediates on Cu–Fe interfacial sites can make the desorption of formed C_2H_4 easily occur.

It is worth noting that the synergetic effect has also been proved to be a significant effect for bimetallic catalytic reactions. However, it is easily confused with bifunctional effects in some cases. Synergistic effects specifically improve catalytic performance through interactions between the two kinds of active metals, rather than from each metal contributing to separate reaction steps.[68–70] For example, as shown in Fig. 4(c–f), Gao *et al.* synthesized Pd–Cu nanocubes with a Cu core and intermetallic PdCu atomic layered shell.[71] According to the XANES spectra shown in Fig. 4(g), the electron transfer shows that the adsorption edge of the Pd K-edge of PdCu shifts to a lower energy than Pd foil, which means that the electronic states of surface metals are modulated from the synergistic effect between Pd and Cu. The formation free energies of different reactive intermediates over metallic surfaces are also given to show the moderate energy position of the PdCu atomic layer, resulting in a promising catalytic performance for C_2H_2 hydrogenation. In summary, the stable PdCu intermetallic atomic shell not only achieves the isolation of single Pd atoms to optimize the adsorption mode and anti-segregation ability of Pd as an active center for C_2H_2, but also contributes to enhanced catalytic performance through electron transfer between Pd and Cu.

In this section, through the introduction of effects related to bimetallic catalysts, we can conclude that modifying the adsorption/desorption mode and activation process of specific reactants or intermediates is the key to achieving high-performance in catalytic hydrogenation reactions. All properties above depend on constructing dispersion, ensemble states, and specific interactions between active sites on the bimetallic surface. Aiming for this, in section 3, we will thoroughly discuss the representative research work of the past decade, focusing on three main aspects: the control of nanoparticle size, bimetallic catalysts on the atomic scale, and the interaction between bimetallic active sites and supports. It will not only provide relevant synthesis methods of applied catalysts on hydrogenation but, more importantly, it will also conclude with innovative ideas for designing new bimetallic catalysts.

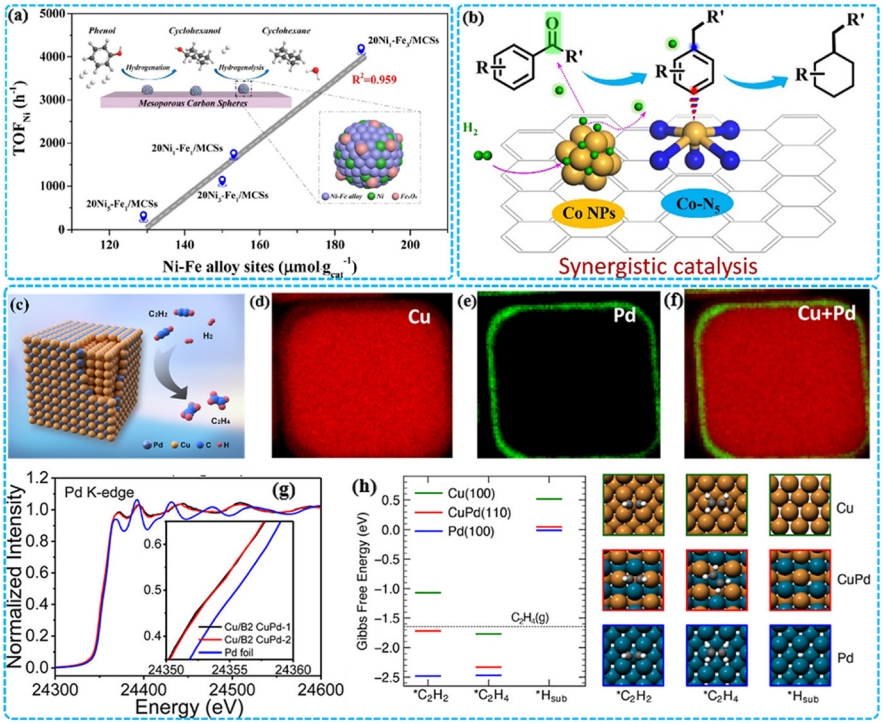

Fig. 4 (a) Schematic for the structure of Ni–Fe alloy sites and stepped hydrogenolysis process of lignin-derived phenolic compounds, with a zoomed view of Ni–Fe alloy, Ni, Fe_3O_4 particles; (b) schematic for the structure of Co atomic sites & nanoparticles and subsequent ring hydrogenation process of aromatic ketones; (c) structure of the Cu–Pd core–shell with an atomic intermetallic layer surface. STEM-EDX elemental mapping of (d) Cu nanocube, (e) Pd atomic layer and (f) PdCu nanocube; (g) Pd K-edge XANES spectra of PdCu nanocubes and Pd foil, with a zoomed view of the Pd K-edge near 24355 eV; (h) standard free formation energies and adsorption modes @298.15 K for $*C_2H_2$, $*C_2H_4$, and $*H_{sub}$ on Cu(100), CuPd(110), and Pd(100) surfaces [panel (a) has been reproduced with permission from ref. 65, Copyright 2019, Elsevier. Panel (b) has been reproduced with permission from ref. 66, Copyright 2023, American Chemical Society. Panels (c–h) have been reproduced with permission from ref. 71, Copyright 2023, American Chemical Society].

3. Synthetic strategies

3.1 Size control

As discussed above, the geometric effect in bimetallic catalysts largely depends on the size of the active metal particles, as it is the key in modifying adsorption and desorption modes of reactants and intermediates during the reaction. In addition to this, the size of the nanoparticles also affects the distribution and utilization efficiency of the active sites.[95–97] Geometrically, metal atoms at the edges and corners are classified as low-coordination sites (LCSs), while metal atoms in terraces and bulk are classified as high-coordination sites (HCSs).[5,96] It is widely accepted that LCSs tend to be more reactive than HCSs due to their unsaturated coordination environment.[98] In addition, the size effects are also reflected in the electronic structure of the catalyst. Unlike the continuous valence band of bulk metals, the band structure of active metal sites becomes discrete energy states when the particle size reduces to the nanoscale, acting similarly to semiconductors.[96,99] It has been proved to interfere with the orbital hybridization and electron transfer between the catalyst and the reactants, resulting in a significant impact on the catalytic performances.[5,96] Therefore, reducing the size of nanoparticles is a promising approach that attracts extensive attention. Table 1 lists representative research work that focuses on controlling the size of bimetallic nanoparticles for hydrogenation reactions through various synthesis strategies, such as impregnation, chemical reduction, deposition–precipitation, strong electrostatic adsorption, *etc.* In this section, based on the two-component nature of bimetallic catalysts, the above methods will be introduced as one-step deposition and two-step deposition.

3.1.1 One-step deposition. Fig. 5 provides a summary of the features of four major strategies of one-step deposition methods, which are chemical reduction deposition, incipient wetness impregnation, deposition precipitation, and strong electrostatic adsorption. In general, the basic idea is to anchor free metal ions on the surface of the support with different methods or processes followed by appropriate post-treatment to finally obtain highly dispersed metal active sites.

Chemical reduction deposition. Chemical reduction is one of the conventional strategies for directly depositing nanoparticles onto supports through a liquid-phase reaction.[100] In this procedure, reduction of a metal precursor occurs close to the surface of the support using a specific reducing agent[95] such as $NaBH_4$, N_2H_4, citric acid, oxalic acid, methanol, or ethylene glycol, *etc.* As shown in Fig. 6(a), Bharath *et al.* successfully synthesized Ru–Pd nanoparticles

Table 1 List of representative work with the synthetic method, particle size, and applications

Catalyst	Method	Particle size (nm)	Hydrogenation reaction	Ref.
$RuFe/Al_2O_3$	IWI/solvothermal reduction	2.3	Lignin-derived phenols to alkyl cyclohexanols	72
PdCu/C	Colloidal synthesis/IWI	7.4	Butadiene to butene	73
$PdCu/Al_2O_3$	IWCI	3.3–18.6	Butadiene to butene	74
$NiRu/Al_2O_3$	LDH precursor	3–9	PyGasMF hydrogenation	75
$CuRe/TiO_2$	IWCI	0.69	Levulinic acid to γ-valerolactone	76
$RuCo/CoO_x$	Solvothermal	2.5	Hydrogenolysis of 5-hydroxymethylfurfural	77
NiCu/C	Solvothermal reduction	17.3	2-Acetylfuran to 2-ethylfuran	78
$NiCo/SiO_2$	MOFs precursors	0.6	Furfuryl alcohol to tetrahydrofurfuryl alcohol	79
AuCu/ZnO	MOFs precursors	18.2	CO_2 to methanol	80
$PtCu/Al_2O_3$	Solvothermal reduction/galvanic displacement	5.2	Furfural to furfuryl alcohol	81
$Pt_3Co/Co(OH)_2$	Solvothermal reduction	4	α,β-Unsaturated aldehydes to α,β-unsaturated alcohols	82
CuPd/HAP	Co-impregnation	3.7	Succinic acid to 1,4-butanediol	83
$FeNi/SiO_2$	Deposition–precipitation with urea (DPU)	5	Furfural to furfuryl alcohol	84
$NiCo/MO_x$	IWI	10	Fischer–Tropsch process	85
RuPd/BN	Chemical reduction/microwave synthesis	2	Furfural to furfuryl alcohol	86
$NiAu/Al_2O_3$	Chemical reduction/galvanic displacement	8	1-Octyne to 1-octene	87
$ReCo/TiO_2$	IWI	1.24	Levulinic acid to γ-valerolactone	88
PdPb/N-doped C	Co-impregnation	1.3	Phenylacetylene to styrene	89
PdAu/N-doped C	Chemical reduction	3.4	Nitrophenol hydrogenation	90
$NiRu/SiO_2$	Strong electrostatic adsorption	0.92	Biphenyl to cyclohexylbenzene	91
$NiFe/TiO_2$	Deposition–precipitation with urea (DPU)	6.32	1,3-Butadiene to butenes	92
$CuRe/Al_2O_3$	IWI	3.7	Furfural to 2-methylfuran	93
IrRe/C	Strong electrostatic adsorption	1.5	Succinic acid to tetrahydrofuran	94

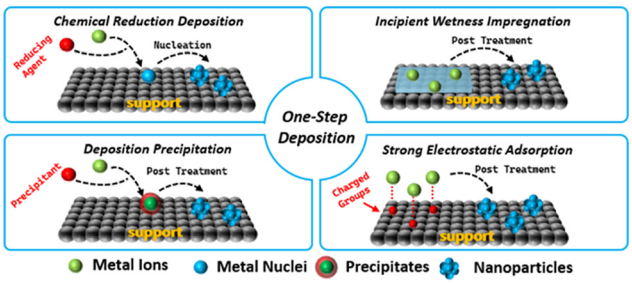

Fig. 5 Schematic representing major synthesis strategies of one-step deposition.

on hexagonal boron nitride nanocomposites using $NaBH_4$ as a reducing agent, and the obtained alloyed nanoparticles are highly dispersed with particle sizes at or below 2 nm.[86] Wang *et al.* reported highly dispersed NiCo nanoparticles supported on MOF/SiO_2 with particle sizes less than 1 nm using $NaBH_4$.[79] Han *et al.* introduced L-ascorbic acid as a reducing agent to deposit Pd–Au bimetallic nanoparticles on nitrogen-doped carbon black through a co-reduction process.[90] With a high metal loading, the average particle size reaches 3.4 nm with a narrow size distribution.

Some chemical reduction procedures driven by a solvent thermal method generally use reductive solvents for reducing metal precursors. For example, ethylene glycol is a conventional solvent as it can be dehydrated into reductive acetaldehyde to reduce adsorbed metal ions. This technique has been reported for the synthesis of dispersed RuFe bimetallic catalysts for the selective hydrodeoxygenation of lignin-derived phenols to cyclohexanol.[72] Fig. 6(b) shows the HAADF-TEM image of the synthesized Pt_3Co alloy on $Co(OH)_2$ nanosheets by the one-pot method.[82] A co-reduction procedure driven by methanol as a reductive solvent obtained uniform Pt_3Co nanoparticles with particle diameters less than 4 nm; the synthesized catalyst shows promising catalytic performance for the selective hydrogenation of cinnamaldehyde to cinnamyl alcohol (Fig. 6(c)). It is worth noting that the type of reducing agent has been found to greatly affect the formed particles.[95] The research work from

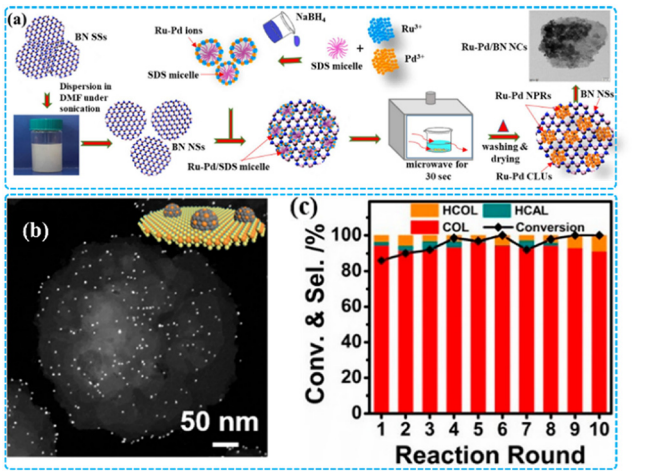

Fig. 6 (a) Schematic illustration of the formation mechanism of the RuPd cluster on boron nitride nanocomposites; (b) HAADF-TEM images and the inserted scheme of synthesized Pt_3Co@$Co(OH)_2$; (c) the stability test of Pt_3Co@$Co(OH)_2$ for hydrogenation of cinnamaldehyde [panel (a) has been reproduced with permission from ref. 86, Copyright 2021, Elsevier. Panels (b and c) have been reproduced with permission from ref. 82, Copyright 2019, American Chemical Society].

Agnihotri *et al.* reveals the effect of reducing agents on the different stages of Ag particle formation from Ag^{+}.[101] At the initial reduction stage, $NaBH_4$ induces the instant nucleation of Ag^0 and trisodium citrate primarily passivates the nanoparticles from agglomeration. In the following stage, trisodium citrate mediated reduction plays a main role in the growth of Ag^0.

Surfactants also contribute to size control during the chemical reduction procedure. In Fig. 6(a), the spherical-like sodium dodecyl sulfate (SDS) micelles serve as a soft template to lead to the formation of spherical Ru–Pd clusters on boron nitride nanocomposites.[86] Taylor *et al.* synthesized ultra-dilute PtCu alloys using ethylene glycol as a reducing solvent and polyvinylpyrrolidone (PVP) as a surfactant. Bruno *et al.* reported the synergetic influence driven by the co-existence of borane *tert*-butylamine (BTB), oleyl amine (OLAM), and oleic acid (OLAC) on the formation of reduced Ni nanoparticles with a narrow size distribution (4.7 ± 0.4 nm), which can be applied to the monometallic precursor for preparing bimetallic catalysts *via* sequential deposition.[87]

Incipient wetness impregnation. For the preparation of supported metal catalysts, the impregnation method is the most commonly used synthesis strategy.[95] It can be classified into wet impregnation and dry impregnation based on the volume of precursor solution that is used during synthesis. For wet impregnation, the amount of precursor solution used is in excess of the pore volume of the support.[95] However, wet impregnation is limited by its ability to achieve precise metal loadings. In comparison, for dry impregnation (DI), also known as incipient wetness impregnation (IWI), the volume of precursor solution is limited to the pore volume of the support.[95,102] The simplicity of dry impregnation and the

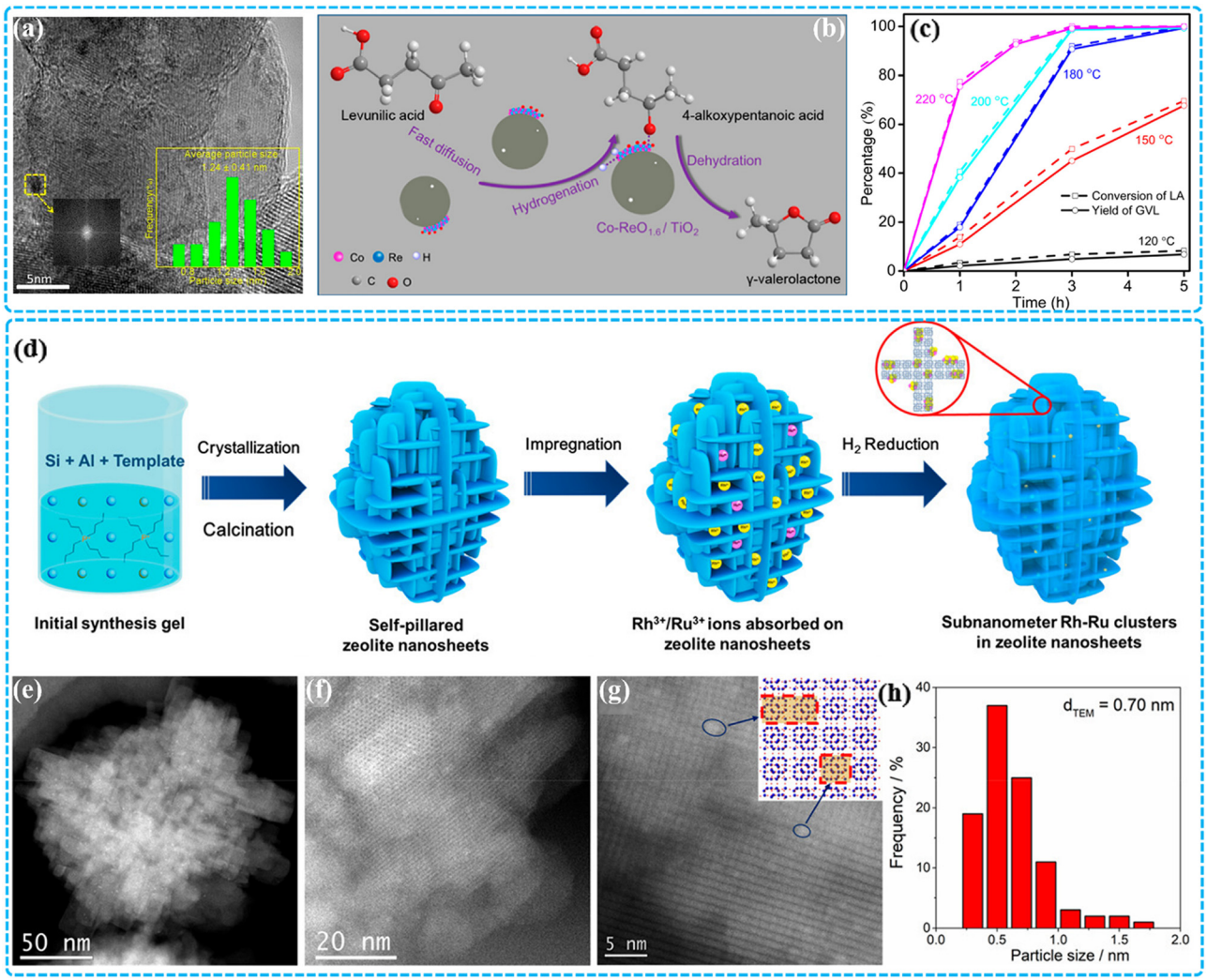

Fig. 7 (a) HRTEM images and size distribution of the 1 wt% $Co_{0.5}Re_{0.5}/TiO_2$ catalyst; (b) schematic of hydrodeoxygenation of levulinic acid over the 1 wt% $Co_{0.5}Re_{0.5}/TiO_2$ catalyst; (c) time courses for hydrodeoxygenation of levulinic acid to γ-valerolactone over the 1 wt% $Co_{0.5}Re_{0.5}/TiO_2$ catalyst; (d) schematic representation of the synthetic procedure of sub-nanometer RhRu clusters in self-pillared MFI nanosheets; (e–g) STEM images and (h) particle size distribution of the prepared $Rh_{0.8}Ru_{0.2}$/MFI sample [panels (a–c) have been reproduced with permission from ref. 88, Copyright 2021, American Chemical Society. Panels (d–h) have been reproduced with permission from ref. 111, Copyright 2021, American Chemical Society].

ability for scale-up made it the most cost-effective approach for synthesizing supported metal catalysts, in both an industrial and academic environment, as very high throughput can be achieved.[102,103] Generally, catalysts prepared through IWI contain large and uneven particles with low dispersion, as well as a weak interaction between the active component and support.[91,95] An acceptable reason is that during the drying process, the active components adsorbed in the pores of the support are redispersed and migrate to the surface of the support due to capillary action, thereby affecting the size of the metal particles on the support.[104,105] Efforts have been made to minimize the size of loaded active particles through optimizing synthesis conditions and modifying support surfaces.[102,106,107]

A common strategy to control the particle size is to reduce the weight loading of active metal.[88,108] Wei *et al.* reported the low loading of $CoRe/TiO_2$ for hydrodeoxygenation of levulinic to γ-valerolactone with 0.5 wt% of Co and 0.5 wt% of Re.[88] As shown in Fig. 7(a), the average particle size is around 1.24 nm with a narrow distribution. The fine size of alloyed nanoparticles allows more active sites to be exposed to the substrate and leads to greater catalytic efficiency. Simultaneously, the synergetic effect between Co and ReO_x accelerates the spillover of H dissociation and mass diffusion of reactants (Fig. 7(b)). As a result, $Co_{0.5}Re_{0.5}/TiO_2$ achieved >99% yield of γ-valerolactone at 220 °C for 3 h (Fig. 7(c)).

Another strategy to control particle size is by extending the aging time.[72] In Liu's work, with conventional IWI methods, Cu–Re bimetallic particles with diameters less than 1 nm are successfully loaded on the TiO_2 substrate *via* an extended aging time, which is up to 24 h.[76] It has been reported that the choice of drying procedure for impregnated samples also affects the dispersion of active metallic particles. For instance, compared with conventional drying in an oven, freeze drying can maintain the spatial distribution of the active components on the support because the solution evaporates below the freezing point under low pressure, and no liquid phase flow occurs.[109] Cao *et al.* found that for Pd–Cu alloyed catalysts prepared by sequential IWI, drying under vacuum can avoid the segregation during the reduction process, which allows the active metal to be distributed more evenly throughout the alloy.[106]

It has been reported that using additives during IWI can help form well-dispersed particles because of the coordination effect between additives and special metallic cations. Triethanolamine has been found as an additive reported to coordinate Cu^{2+} in the precursor solution and improve the dispersion of Cu.[16] In Quindimil's work, glycerol was introduced to assist in the IWI method. Compared with conventional impregnation, the addition of glycerol leads to an enclosing effect with Ru^{3+}, which reduces the Ru particle size from 11.2 nm to 5.8 nm.[110] However, for Ni monometallic particles, glycerol has the opposite effect on particle size control. Nevertheless, Ni–Ru bimetallic particles prepared by the glycerol-assisted IWI method show a notable increase in performance over monometallic catalysts for CO_2 methanation, with the methane yield rising from 20% to 40% at 300 °C.

In other cases, other well-designed supports like LDH precursors, MOFs, and zeolites have also been reported to show a positive effect on particle size control.[54,111,112] As shown in Fig. 7(d), Wang *et al.* successfully constructed self-pillared MFI zeolite nanosheets with a high surface area and abundant Si–OH groups, which makes them an ideal support to immobilize ultrasmall Rh–Ru bimetallic nanoclusters *via* the simple IWI method.[111] Fig. 7(e–g) shows the STEM images for the synthesized sample, it can be seen that the ultrasmall nanoparticles are anchored into the MFI zeolite's structure, and the average particle size is 0.7 nm (Fig. 7(h)). The Rh–Ru alloy with a specific molar ratio of Rh : Ru = 0.8 : 0.2 shows a superior H_2 generation rate (1006 mol_{H_2} mol_{metal}^{-1} min^{-1}) from ammonia borane hydrolysis and promising catalytic activities on cascade hydrogenation of nitroarenes.

Deposition precipitation. Deposition–precipitation is a method that converts soluble metal salt precursors into non-soluble precipitates with the addition of appropriate precipitant and immobilizes them onto the support.[95] Post-treatments are generally required to obtain activated supported catalysts after the precipitation process.[113] The key to catalyst preparation through this method is to selectively deposit nanoparticles on the support instead of forming in solution.[95,114] In the deposition–precipitation process, metal salt precursors in solution preferentially deposit on the surface of the support, which acts as a nucleation site for metal ions, resulting in a lower solubility limit at the support surface compared to the bulk solution.[95,114] To prevent localized precipitation, the added precipitant must form uniformly distributed OH^- species in the solution.[114,115] Sodium hydroxide,[116,117] ammonium,[118,119] and urea[84,120] are commonly used as precipitants. Among these, the deposition precipitation with urea (DPU) method has become the most widespread strategy in recent years due to its ability to achieve almost total metal precipitation even at high metal weight loadings and yields tight nanoparticle distributions.[114,115,121] The effectiveness of urea lies in its ability to hydrolyze at temperatures above 50 °C, producing evenly distributed OH^- species throughout the solution, minimizing localized gradients in pH, thereby reducing the possibility of precipitation in the bulk solution.[114,122]

DPU is a common approach in the synthesis of supported catalysts, although specific experimental conditions vary between research groups. Generally, the procedure of DPU can be operated through the following steps:[115] firstly, the suspension with support material should be heated to a temperature where urea is stable. Then, the metal salt precursor and urea are added to the suspension for precipitation. The mixture usually needs to be aged under continuous stirring in order to obtain a uniform deposition of deposited nanoparticles, and the aging time can vary from several hours to one day.[123–125] Finally, the obtained solids need to be washed and activated at a temperature under a

reductive gas flow. In this method, the synthesized nanoparticles have particle sizes between 2 and 10 nm. Wang *et al.* prepared a Ni–Fe/TiO_2 catalyst for selective hydrogenation of 1,3-butadiene by the CO-DPU method.[92] With increases in the Ni : Fe ratio, the size of uniformly distributed particles increases from 3.92 nm (mono-Ni) to 6.32 nm (Ni : Fe = 1 : 0.33). Simultaneously, the alloying tendency of nanoparticles gradually increases as the Fe content increases, resulting in greater catalytic performance. For a 200 h stability test, the reported catalyst maintains a high butadiene conversion of over 99% and the selectivity to butene is higher than 95%, greatly outperforming the commercial Pd/Al_2O_3 catalyst under the same reaction conditions. Shi *et al.* investigated the synthesis parameters of Fe–Ni/SiO_2 for the hydrogenation of furfural.[84] Firstly, Ni(II) and Fe(II) sulfate salts are used as precursors instead of nitrate salts to eliminate the oxidizing species. After 22 h of the DPU process, the deposited solids were activated under H_2 through multi-step reduction: (1) reduction of Fe^{3+} to Fe^{2+} around 275 °C, (2) reduction of Ni^{2+} to Ni above 350 °C and (3) the deep reduction of Fe^{2+} to Fe between 500–700 °C, which induced the diffusion of Fe atoms into the Fe–Ni alloy. The optimized procedure resulted in homogeneous alloyed Fe–Ni nanoparticles with an average size of 5.4 nm. Zanella *et al.* deposited Au–Ni bimetallic nanoparticles on TiO_2 with CO-DPU and obtained particles with particle sizes less than 3 nm.[124] The adjustment of the atomic ratio of Au : Ni finally reached the optimal value of 1 : 0.08, which shows the best compromise between conversion and selectivity for the selective hydrogenation of 1,3-butadiene. The average size of Au–Ni nanoparticles was determined to be 2.2 nm. The results also revealed the universality of DPU for co-depositing bimetallic particles with size control, even for poorly miscible metals such as Au and Ni. Zanella's group also studied the possibility of synthesizing Au–Ru bimetallic particles through the DPU method.[120] Interestingly, Janus-type nanoparticles prepared by sequential deposition (first Au then Ru) show completely different segregation behaviors at reduction temperatures of 300 and 500 °C, which cause a significant impact on their catalytic activity. In their recent research, DPU was applied to deposit Au–Cu bimetallic particles with an average particle size of 3.3 nm on TiO_2.[123] It was found that segregation during the activation process may cause CuO_x to partially migrate to the surface of bimetallic nanoparticles. Simultaneously, the strong interaction between Au and CuO_x can anchor Au on the TiO_2 surface, thereby reducing the restructuring and aggregation of Au during the catalytic process and significantly increasing the stability of the catalyst.

In addition, DPU can be combined with the strategy of *in situ* growth method to create bimetallic particles that can be directly reduced from precursors with a well-fabricated structure. Yang's group reported the fabrication of Al_2O_3-supported Ni–Ru bimetallic catalysts by reducing precursors of $Ni^{2+}Ru^{3+}Al^{3+}$ that contained layered double hydroxides (NiRuAl-LDHs) in flowing H_2.[75] It was found that the existence of Ru^{3+} in the LDH layer can promote the reduction of Ni^{2+} by H_2 spillover and significantly decrease the size of Ni particles, as well as the formed Ni–Ru alloy particles. Liu *et al.* developed an alumina microsphere (AMS) supported Ni–Cu nanoparticles with a hierarchical flower-like structure for catalytic transfer hydrogenation of ethyl to γ-valerolactone.[126] As shown in Fig. 8(a), the alumina microsphere was used as a support, and DPU was introduced to trigger an *in situ* growth of NiCuAl-LDH precursors on the surface of the alumina microsphere. After the calcination/reduction step, Ni–Cu nanoparticles can be formed on a layered alumina sheet with an average particle size of 8.56 nm.

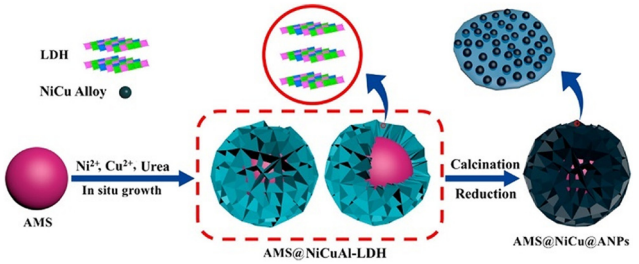

Fig. 8 Synthetic procedure for AMS@NiCu@ANPs through transformation of the AMS@NiCuAl-LDH precursor [panel has been reproduced with permission from ref. 126, Copyright 2019, American Chemical Society].

Strong electrostatic adsorption. Strong electrostatic adsorption (SEA) is the method of modifying the interaction between the support and precursor of the metal complex by controlling the pH value during the impregnation process.[95,114] As reported, the nature of interaction between the metal complex and oxide support is based on a coulombic force, which can be changed with charge variation.[127,128] A critical concept in SEA is the point of zero charge (PZC); the PZC is the point at which the surface of the support is neutrally charged. For a support surface distributed with hydroxyl groups (OH^-), anionic metal complexes (*e.g.*, $PtCl_4^{2-}$ (ref. 129), $IrCl_6^{2-}$ (ref. 94), $AuCl_4^-$ (ref. 130), *etc.*) can adsorb to the surface through strong electrostatic interactions when the surface is protonated by lowering the pH of the solution below the PZC.[95] Conversely, strong electrostatic interactions can be established between cationic metal complexes (*e.g.* $Ru(NH_3)_6^{2+}$,[91] $Pd(NH_3)_4^{2+}$,[129] *etc.*) by deprotonating the surface by raising the pH of the solution above the PZC. According to the measuring method descripted, PZC can be determined by the DI method, and the pH of the paste formed by the solution and support can be buffered to be near the PZC of the support, as the number of hydroxyl groups on the support surface is orders of magnitude higher than the H^+ or OH^- in the solution.[131] Once the PZC is determined, the second step is to perform an uptake survey to determine the maximum adsorption of the metal complex at a certain pH value.[95] A typical volcano curve shown in Fig. 9(a) displays the trends in metal precursor

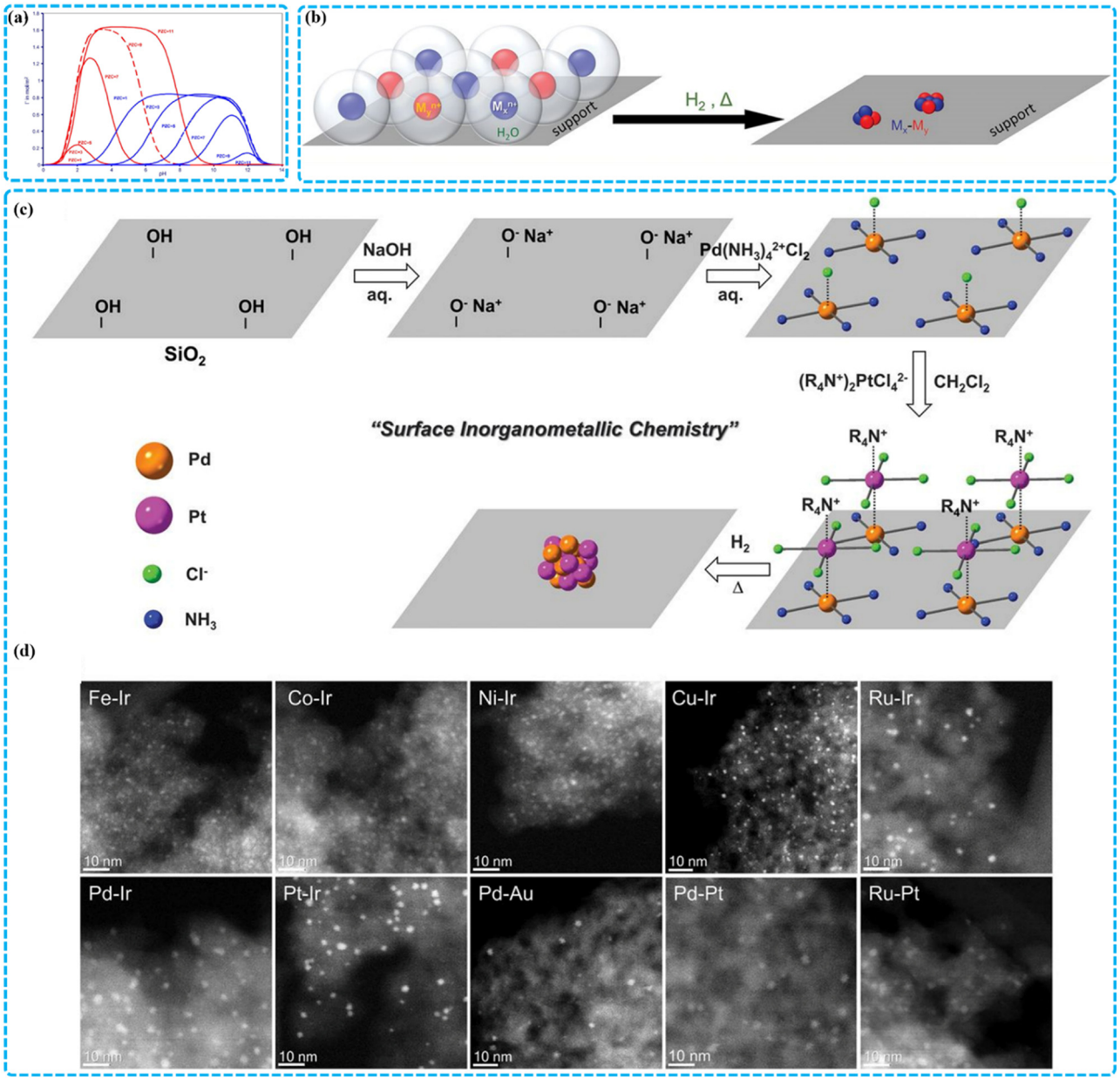

Fig. 9 (a) Simulation of $[PtCl_6]^{2-}$ or $[(NH_3)_4Pt]^{2+}$ *versus* pH for various PZC materials; (b) monolayer mixture of metal precursors electrostatically adsorbed and clusters of alloyed nanoparticles formed after H_2 reduction; (c) schematic of the process for the synthesis of sequential-SEA method; (d) HAADF-STEM images of 10 types of supported bimetallic NPs synthesized by sequential-SEA [panel (a) has been reproduced with permission from ref. 137, Copyright 2011, Elsevier. Panel (b) has been reproduced with permission from ref. 17, Copyright 2017, American Association for the Advancement of Science. Panels (c and d) have been reproduced with permission from ref. 130, Copyright 2018, American Association for the Advancement of Science].

uptake with the variation in the pH value of the solution. It is worth noting that the SEA is usually performed with limited support in excess liquid to minimize the pH shift caused by the buffer effect. Surface loading (SLs, $m^2\ L^{-1}$) is the value that is set to represent the ratio of liquid to support, which means the area of support surface per volume of precursor solution. In the case of the SEA process, the requirement for a high liquid/support ratio means SLs should be kept within the range of 500 to 2000 $m^2\ L^{-1}$.[95] Then, the catalyst sample after impregnation will be treated through calcination or reduction to remove the ligands from the metal complex, resulting in a catalyst with highly dispersed active particles.[114,132]

SEA is a flexible and universal approach as it can be adapted to a variety of combinations of support and metal species.[129,130,133] Regalbuto *et al.* originally proved the possibility of a rational synthesis approach for alloyed bimetallic nanoparticles based on the co-SEA method.[17] In this work, common silica (PZC = 3.6) was used as a support to adsorb a variety of noble and base metal ammine

precursor pairs (Pt, Pd, Cu, Ni, and Co). Fig. 9(b) represents an electrostatically adsorbed layer of a mixture of hydrated metal precursors, followed by a reduction step in H_2 to remove the metal ligands and reduce the metals to a zero-valent state. The obtained bimetallic nanoparticles of ten permutations of noble and base metals have average sizes ranging from 0.9 to 1.4 nm and show good interactions between metals. This generalizable approach can be extended to other supports like alumina, titania, and carbon as long as the metal precursors are available to be used with the specific support that has a corresponding PZC value. Generally, for supports with a high PZC, anionic chloride complexes can be applied as precursors. Keels *et al.* successfully synthesized an Ir–Re/C bimetallic structure by co-SEA, which is an effective catalyst for aqueous-phase hydrogenation of succinic acid.[94] $IrCl_6^{2-}$ and ReO_4^- were chosen as the metal complex precursors according to the PZC of activated carbon (PZC = 7). The surface loading was set as 1000 m^2 L^{-1}, and both precursors were impregnated simultaneously according to the uptake survey. It was found that the bimetallic structure consists of highly dispersed Ir particles with diameters of around 1.5 nm, partially covered by Re due to their close contact. Recently, Yang *et al.* reported the selective hydrogenation catalytic behavior of Ni–Ru/SiO_2 prepared by co-SEA.[91] The average diameter of Ni–Ru/SiO_2-SEA particles was 0.92 nm, which is 2.6 times smaller than that of the sample obtained by the traditional IWI method. It has been proved that the existence of Ru enhances the hydrogen spillover effect, and the enforced interaction between the Ni–Ru alloy and SiO_2 leads to the transfer of electrons from the metallic Ni to SiO_2 surface. The synergistic effects lead to the formation of electron-deficient $Ni^{\delta+}$ species, promoting the selective hydrogenation of biphenyl to cyclohexylbenzene.

For bimetallic catalysts, the two metal active components can not only be loaded through co-SEA but also by sequential-SEA. Ding *et al.* reported a representative work of sequential-SEA for various metal combinations.[130] As shown in Fig. 9(c), the support was dispersed in solution, and the pH was adjusted to negatively charge the surface. Then, the first cationic metal complex was introduced into the system in a normal SEA process, followed by washing and drying. The secondary metal anion complex was then added into the solution, which can precisely pair with the first metal complex through electrostatic interactions. After a reduction in H_2 flow, well-defined bimetallic nanoparticles are successfully deposited on the support. By introducing oppositely charged complex precursors, the issue of competitive adsorption in the general co-SEA process can be avoided. Fig. 9(d) proved that this general approach can be applied to a large variety of bimetallic combinations, and the diameter of these bimetallic particles ranges from 1 to 3 nm with narrow size distributions (±25%). Also, as the first-step synthesis, SEA built highly dispersed particles of the first metal as metal seeds, which are anchored on the surface of the support. In subsequent steps, the immobilized particles facilitate the targeted deposition of the secondary metal into the coordination environment of itself by selective reduction, galvanic deposition (GD), or electroless deposition (ED), aiming to obtain a highly dispersed bimetallic structure. Chen *et al.* reported a method for loading Pd on a reducible ZnO support by SEA and loaded Pd induced ZnO to be selectively reduced to Pd–Zn intermetallic compounds (IMC) in H_2 atmosphere.[39] The size of the uniformly distributed Pd–Zn IMC is around 7 nm. Although it is greater than the size of particles synthesized by the general SEA, the reported particles tend to reduce the aggregation caused by the Ostwald ripening effect during the reduction step. The authors claimed that a uniform distribution of Pd and Zn existed in the lattice of Pd–Zn, indicating that an IMC was obtained rather than an alloy. Riyapan *et al.* reported the bimetallic structure of Ag–Pd/TiO_2 prepared by SEA of Pd on TiO_2 followed by the ED method of depositing Ag on Pd.[134] Due to the SEA methodology, the formed Pd particle size is around 2 nm with uniform distribution. Controllable monolayer coverage of Ag through the ED method can effectively dilute the exposed surface of Pd sites and result in a tunable adsorption behavior of acetylene.

To emphasize, the premise of highly dispersed metal nanoparticles obtained by SEA is the monolayer adsorption of metallic precursors, which are in direct contact with the support surface through electrostatic forces.[113] The adsorbed precursors not only include metal ligands but also hydration sheaths that occupy the space around the ligands, which limits the metal loading of the catalysts prepared through this method by taking up space on the surface.[17,131,135] However, the hydration sheaths can be removed in the subsequent pretreatment step, creating more available space on the support surface. Hence, catalysts with higher metal loadings can be obtained through multiple performing cycles of SEA.[136]

3.1.2 Two-step deposition

Galvanic displacement. Galvanic displacement (GD) is a redox reaction with an electron transfer process in which the primary metal, immobilized on the surface of a support, acts as a reducing agent and a sacrificial template to drive the *in situ* deposition of secondary metal onto the surface of the primary metal.[18,138] As shown in Fig. 10(a), the primary metal atoms are oxidized and subsequently replaced by secondary metal atoms, which are reduced from the aqueous solution. Equations described in Fig. 10(a) point out that the GD process must be driven by the thermodynamic favorability of the paired reactions, as predicted through the standard reduction potentials.[138,139] For example, Zhang *et al.* have proved the possibility of replacing Ag atoms from supported Ag nanoparticles by Pd^{2+} ($Pd^{2+} + 2e^- = Pd^0$, $E^\circ = 0.915$ V; $Ag^+ + e^- = Ag^0$, $E^\circ = 0.799$ V), however, the opposite displacement reaction can't occur.[34] Generally, the GD method can be used to replace a base metal with a more reducible noble metal, acting as the second step for preparing a bimetallic system if a highly dispersed primary metal has already been obtained. Since the redox reaction is only driven by the difference in reduction potential, without any extra reducing agent,

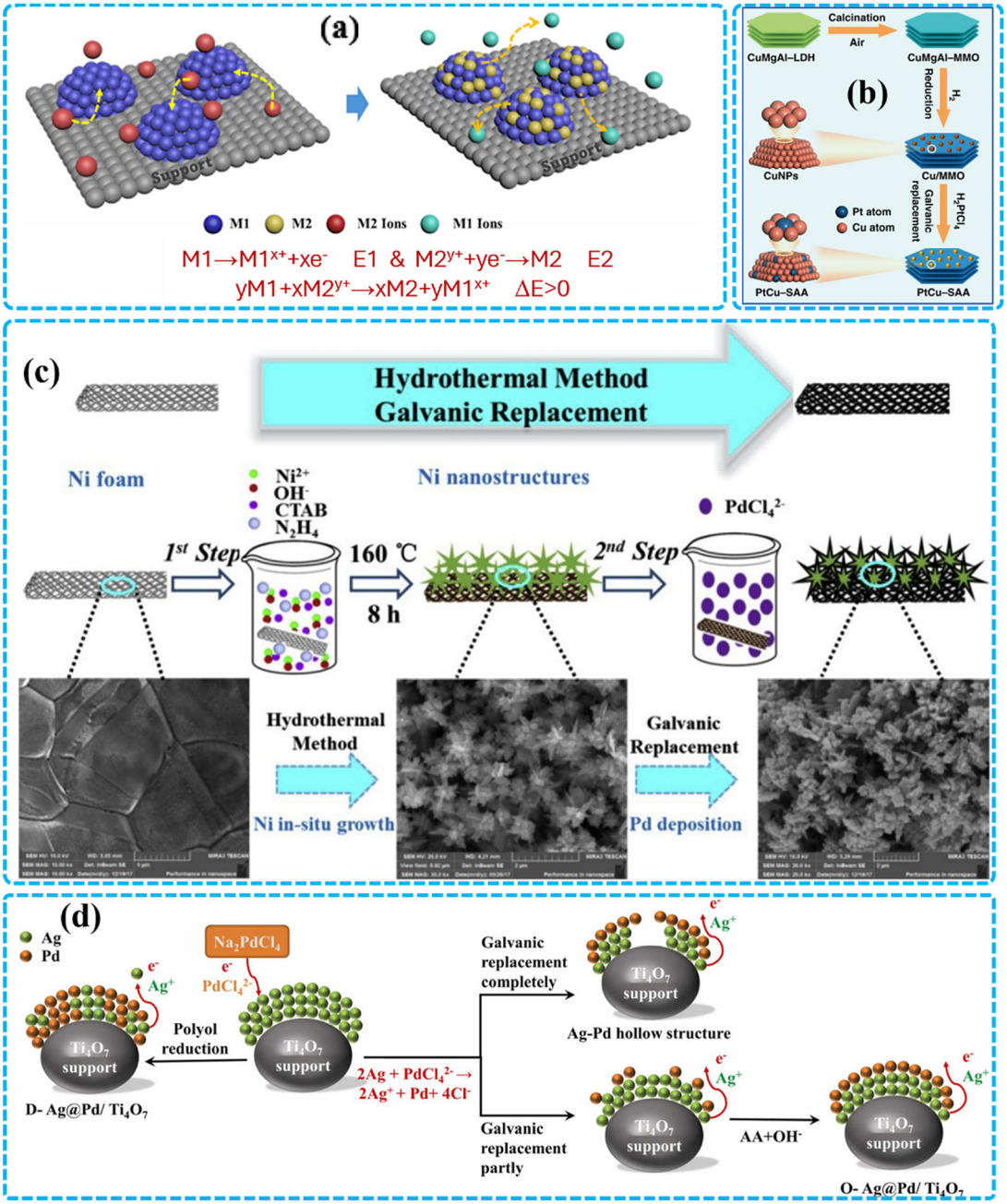

Fig. 10 (a) Galvanic displacement method for supported-metallic catalyst synthesis; (b) a schematic illustration for preparation of PdCu–SAA-LDH; (c) the synthesis process of the hierarchical PdNi–Ni foam catalyst; (d) a comparison of the synthesis process of the PdAg–Ti_4O_7 catalyst [panel (b) has been reproduced with permission from ref. 142, Copyright 2019, Springer Nature. Panel (c) has been reproduced with permission from ref. 144, Copyright 2019, Elsevier. Panel (d) has been reproduced with permission from ref. 148, Copyright 2022, Elsevier].

contamination and byproducts can be avoided in the final product.

Zhou *et al.* reported a rational synthesis strategy for a series of bimetallic catalysts RuM/TiO_2 (M = Fe, Co, Ni, and Cu) that can be used in the selective hydrogenation of benzene. In this strategy, the primary base metals are supported by TiO_2 by wet impregnation–chemical reduction and sacrificed as templates to anchor Ru atoms atop themselves by GD. Then, an innovative acid treatment method was used to further alter the content of the template. It has been proven that Ru can donate electrons to base metals during the hydrogenation reaction, and the degree to which Ru becomes electron-deficient corresponds positively to the cyclohexene selectivity, which reaches a maximum at 85%.[140] Peng *et al.* synthesized single atoms of Pt embedded into Ni crystals that were supported on active carbon. Ni crystals with an average diameter of 4.4 nm were prepared in advance, followed by GD that occurred in a hexane medium using a $Pt(acac)_2$ precursor. It was found that the formed Pt single atoms were highly isolated on Ni crystal surfaces,

leading to an optimized adsorption configuration for 3-nitrostyrene that was favorable for the activation of nitro groups, resulting in high selectivity for 3-vinylaniline.[141] GD can also be applied to the synthesis of single-atom alloy catalysts. Zhang *et al.* reported a Pt–Cu/LDH single-atom catalyst with single Pt atoms dispersed on Cu nanoclusters.[142] As shown in Fig. 10(b), Cu-LDH was initially formed based on a structural transformation from CuMgAl-LDH hydrotalcite precursors under a H_2 reduction atmosphere; once formed, a controllable GD process was used to load single Pt atoms onto the surface of Cu. Compared with the corresponding monometallic catalysts (Pd/LDH and Cu/LDH), a dramatic increase in the turnover frequency to 2.6×10^3 mol mol^{-1} h^{-1} was observed for the hydrogenolysis reaction of glycerol to 1,2-propanediol. The increased performance resulted from the interfacial synergistic effect between Pt single atoms and Cu, which can decrease the activation energy during the hydrogenolysis reaction. This preparation route has also been extended to other metal alloy systems. Recently, Xu *et al.* proposed a Pd-based single-atom alloy catalyst, Pd–Cu/LDH based on the same routine as discussed above. The single atom-cluster structure not only shows a high selectivity for acetylene hydrogenation but also plays a role in tuning the thermal effect during the catalysis reaction. It was found that the heat generation rate over Pd was dramatically decreased due to its ultra-small size. Simultaneously, Cu nanoclusters that host Pd atoms can provide a micro-environment with attractive lattice heat capacities and phonon scattering rates, which can rapidly transfer the heat generated on Pd sites by the reaction to the surroundings.[143] In addition, GD can be applied to the bimetallic catalyst system with a metallic support. Chen *et al.* reported a hierarchical Pd–Ni bimetallic alloy with a snow-like nanostructure supported on Ni foam for nitrobenzene hydrogenation.[144] As shown in Fig. 10(c), the snow-like Ni was initially synthesized on Ni foam through a hydrothermal method, followed by the GD method to deposit a hierarchical Pd shell over it. During the hydrothermal process, cetyltrimethylammonium bromide (CTAB) is an indispensable structure-directing agent for the formation of the snow-like Ni nanostructure, and the specific aging temperature is key for obtaining a high specific surface area product. Then, benefiting from the increased BET area, the Pd loaded through the GD method can be formed with good dispersion and strong interaction with Ni. The unique structure of the Pd–Ni bimetallic system ensured a large extent of active site exposure, which resulted in better performance for the hydrogenation of nitrobenzene. Fu *et al.* proposed the 2D Pd rafts confined in (111) exposed Cu nanosheets for the selective hydrogenation of acetylene.[145] In their work, Cu(111) acts both as the support and as the primary metal for loading Pd by the GD method. The isolated Pd–Cu coordination environment balances the advantages of Pd for reducing the energy barrier of semi-hydrogenation and Cu(111) for weakening the adsorption of ethylene, which results in high conversion and selectivity for the hydrogenation of acetylene.

Furthermore, as an atom-to-atom reaction, the rate of the GD process can be controlled by tuning the reaction parameters for possibly pursuing secondary metal distribution and controllable nucleation.[18,146] Zhang *et al.* showed that the uptake of Pd^{2+} in the GD bath is highly related to the different loading of $Pd(NO_3)_2$.[147] Specifically, all Pd^{2+} can be exchanged into Pd at lower Pd^{2+} levels, however, only 50% of the Pd^{2+} was exchanged when the Pd concentration reached 48 μmoles per $g_{catalyst}$. It was also found that the actual amount of Pd displacement was much greater than the theoretical limit for the GD process, which suggested that the large difference in the surface free energies of Pd and Ag leads to the diffusion of Pd into the bulk of Ag particles with Ag transferring to the exposed surface to provide fresh Ag atoms for further galvanic displacement. Zhang *et al.* reported a route for synthesizing $PdAg/Ti_4O_7$ covered by a continuous ordered Pd shell over the surface of Ag nanoclusters.[148] Briefly, Ag was first reduced onto the Ti_4O_7 support surface by 1,2-propanediol as the primary metal, and followed by an initial GD process with a small amount of $PdCl_4^{2-}$ to form Pd "seeds" rather than carrying out a complete displacement. Then, in the presence of ascorbic acid (AA), more $PdCl_4^{2-}$ was reduced to Pd around the initial Pd seeds, forming an ordered Pd shell. As shown in Fig. 10(c), unlike the complete GD process, the sequential GD process can create the ordered deposition with a minimal loss of primary metal to avoid the inevitable leaching of the primary metal and uncontrollable deposition and segregation resulting from the chemical reduction method. Most importantly, it has been proven that the morphology and thickness of the Pd shell over the Ag surface can be modified by simply changing the amount of $PdCl_4^{2-}$ precursor used, which gives potential for this technique to be applied to the synthesis of other bimetallic systems.

Electroless deposition. Electroless deposition (ED) is the controllable deposition process that can deposit secondary metal (M2) precursors on the primary metal (M1) sites that are already loaded onto a support.[18,102] As its name suggests, the ED process occurs without an external current, but is driven by a reducing agent (RA) that is activated by M1 sites. Hence, the application of ED aims to form a bimetallic surface by selectively depositing M2 on the metallic surface without forming isolated M2 crystallites on the catalyst support. Fig. 11(a) shows a general ED process starting with the mixture of RA, ions of M2, and supported M1. Firstly, RA is activated by M1 sites, and an *in situ* reduction deposition between M2 ions and the activated RA will occur to allow M2 deposition on the M1 surface, which is a catalytic process. Furthermore, nucleated M2 can also activate RA and allow M2 precursors to deposit on itself automatically and finally cause the formation of the M2 cluster combined with M1, which is an autocatalytic process. As seen from the illustrated mechanism, it can be concluded that the ideal

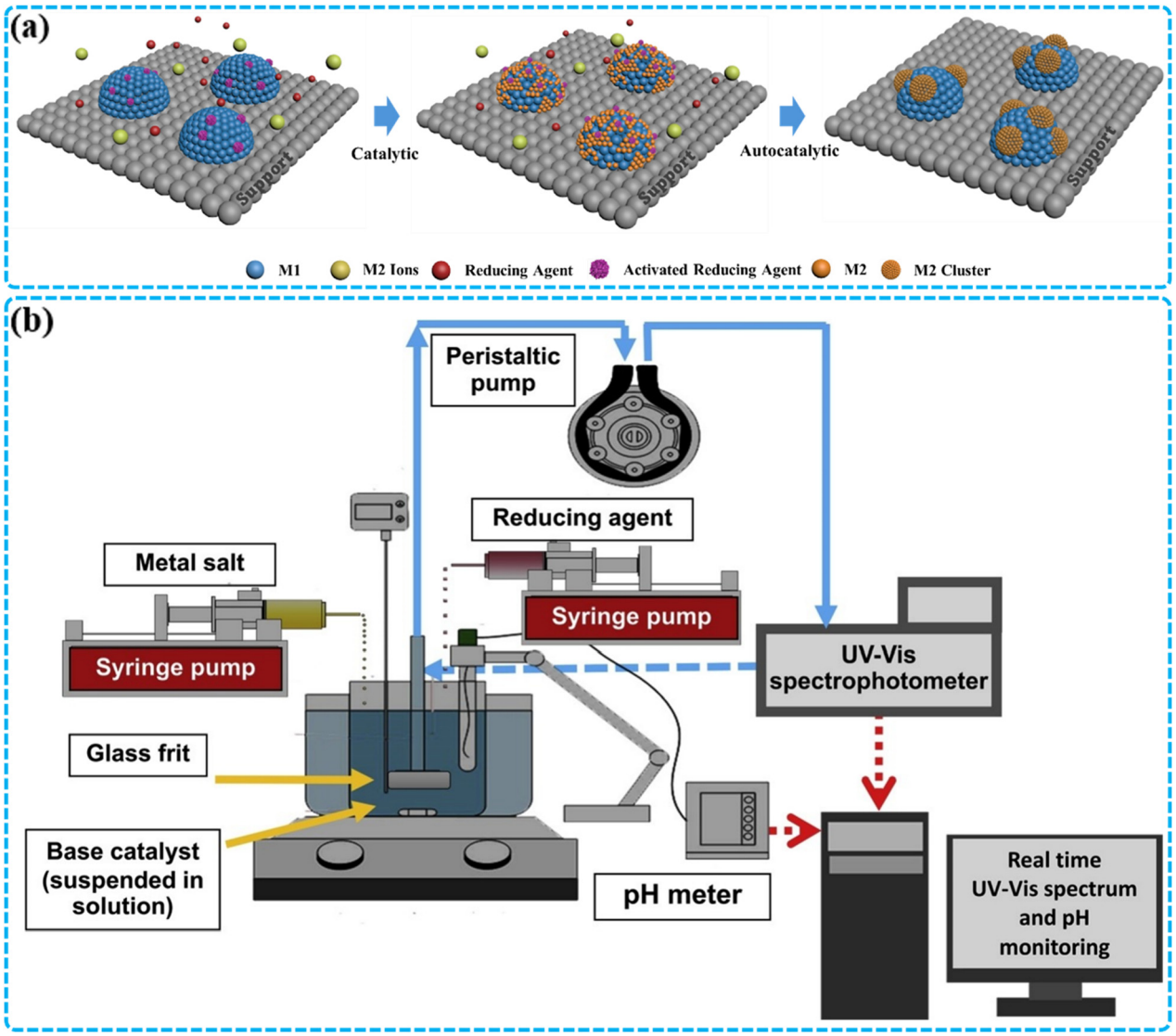

Fig. 11 (a) Electroless deposition method for supported-bimetallic catalyst synthesis with the catalytic process and autocatalytic process; (b) schematic illustration of the continuous ED procedure [panel (b) has been reproduced with permission from ref. 153, Copyright 2019, Elsevier].

bimetallic catalyst created by ED would be getting a partial monolayer or a few monolayers of M2 to combine with M1 selectively and precisely, instead of forming continuous films of M2.[18] To avoid indiscriminate deposition, the reducible M2 precursors must display the same charge as the surface charge of the support, otherwise, the co-existing opposite charges will lead to an undesirable SEA process, which forms a monometallic surface rather than a bimetallic surface. However, it is possible to minimize the SEA process by introducing additional soluble salts that can shield the surface charge of the support. Schaal *et al.* proved that the excess addition of Na^+ during the ED process can virtually suppress the SEA effect occurring between Ag^+ and Pt/SiO_2.[149] The added Na^+ can positively charge the SiO_2 surface preferentially and stabilize the ED bath system by shielding Ag^+ from the SiO_2 surface.

The goal of ED also requires avoiding the unnecessary nucleation of the second metal in the ED bath liquid. On the one hand, although there is no metal loss during the filtration and collection, independently nucleated M2 cannot interact with the primary metal and fails to show effects that can only be provided by the bimetallic system. On the other hand, once nucleation of M2 occurs in the bath liquid, competitive autocatalytic deposition inevitably reduces the loading of M2 on the primary metal. In this case, to obtain optimized bimetallic surfaces, the key is to stabilize the ED bath system by limiting the nucleation rate of the secondary metal. One general way for stabilizing the system is to use specific ligands as stabilizers that can combine with M2 ions and lower the consumption rate of M2 since the formation constant (K_f) for some metal complexes is sufficiently large enough to resist the quick reduction of the M2 precursor, such as $[Ag(CN)_2]^-$, $[Co(NH_3)_6]^{3+}$, $[Fe(EDTA)]^-$, $[Cu(CN)_4]^{2-}$, *etc.*

For reference, detailed research given by Djokić lists common complex agents that can be used for different metal salts in electroless deposition.[150]

It has been proven that the instability period in the ED bath usually exists at the beginning of the deposition because the RA and the reducible metal precursor are both simultaneously at their highest concentrations, which manifests as a rapid decrease in the concentration of reducible M2 ions within a short period of time after the start of ED.[151,152] As shown in Fig. 11(b), Tate *et al.* developed a method in which the RA and reducible M2 precursors are added separately to the ED bath using syringes with a controlled pumping rate, denoted as the continuous ED procedure, successfully matching the rate of ED reagent addition with that of its consumption.[153] Besides, because of the nature of the redox reactions occurring between the reducible M2 ions and the RA, a stable ED bath system must include considerations for the redox potential factor, which is highly related to the selection of a suitable RA and the pH of the ED bath. Generally, the choice of RA always depends on the bimetallic surface combination and sequence of depositions, since different reducing agents show significant preferences for different metals, even though they all have sufficient standard oxidation potentials to reduce these metals. Detailed research of Ohno[154] indicates the different abilities of RAs ($H_2PO_2^-$, HCHO, BH_4^-, N_2H_4, *etc.*) to combine with group VII and group IB metals. In the case of the ED process, the dominant catalytic process that allows M2 to preferentially deposit on M1 will occur once the applied RA shows a more negative redox potential with M1. For example, for the Cu–Pd bimetallic system, HCHO can be applied as the RA for depositing Pd on Cu, however, BH_4^- is a more suitable RA for the reverse example of depositing Cu onto Pd. In the case of the pH value, based on avoiding precipitation and keeping to the correct side of the support's PZC, the pH value should be monitored (Fig. 11(b)) and kept stable during the whole ED process since the standard oxidation potential of the RA varies a lot when pH fluctuates,[155] which causes changes in the rate of deposition.[18,153]

In addition to controlling the properties of the reactants in the ED procedure, changes in external reaction conditions can also be applied to affect the deposition rate. For example, by maintaining relatively mild agitation, the limited rate of external mass transfer can effectively reduce the rate of the ED procedure, especially when the rate of diffusion is lower than the rate of deposition. By contrast, according to the Arrhenius equation, limiting the deposition rate by appropriately lowering the temperature is a more effective approach because temperature acts on the reaction rate constant exponentially. Research has shown that a suitable temperature for the ED bath is a vital parameter for balancing the stability of the ED system and the deposition rate.[153,156]

It is worth noting that smaller particle sizes do not always correlate with improved catalytic performance for various hydrogenation reactions.[157–159] Rupprechter *et al.* demonstrated that the size distribution of Pd nanoparticles affects the selectivity of isomerization and hydrogenation of 1-butene.[157] For Pd/Al_2O_3, larger Pd nanoparticles dominated by the (111) facet favored hydrogenation reactions, while smaller Pd nanoparticles were more selective on the isomerization of 1-butene. A recent study by de Jongh *et al.* showed that Cu nanoparticles in the range of 7–10 nm show better performance than 2 nm particles for the selective hydrogenation of 1,3-butadiene.[160] In short, larger Cu particles were ascribed to a higher fraction of kinks and step sites, essential to activate hydrogen, as well as a stronger preferential adsorption of diene. In the case of bimetallic catalysts, García *et al.* demonstrated that for CO_2 hydrogenation, 10 nm CoFe alloy particles are the most selective samples for the formation of C_2–C_4 hydrocarbons, while smaller particles promote the formation of CO, and larger particles increase the selectivity to CH_4.[161] Also, compared to large particles, studies have proved that smaller nanoparticles are easier to sinter, aggregate, or get active sites covered by by-products during the reaction.[162] Therefore, reasonable regulation of particle size is necessary and should be severely considered based on the incorporation of the second metallic component, appropriate synthesis strategy, and specific reaction conditions.

3.2 Single atom catalysts

Since the first report of single atom catalysts (SACs) from Zhang *et al.* in 2011,[185] SACs have attracted much attention from researchers over the past decade because of their promising potential for applications in energy conversion, which originates from their adjustable structure and maximum atomic utilization of catalytic metals.[186,187] Based

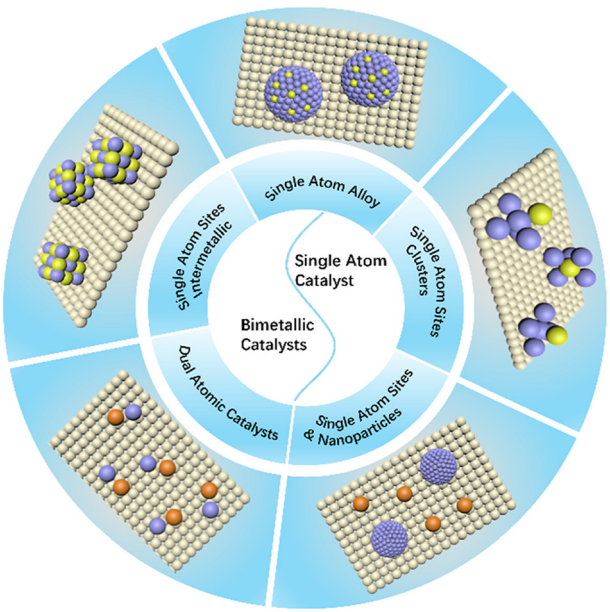

Fig. 12 The types of atomically dispersed bimetallic catalysts.

Table 2 List of representative work with bimetallic single atom catalysts, synthetic method, category, and applications

Catalysts	Bimetallic sites	Synthesis strategy	Loading	Application	Ref.
$PdCu/SiO_2$	SAAs	Incipient wetness co-impregnation	Pd : Cu = 0.006 : 1	C_2H_2 hydrogenation	35
$PdAu/SiO_2$	SAAs	Sequential reduction	Pd : Au = 0.004 : 2	Hydrogenation of 1-hexyne	163
FeK/Co–NC	SAAs	Ultrasonic-assisted melt infiltration method & incipient wetness impregnation	Fe : Co = 80 : 20	CO_2 hydrogenation	164
NiGa/MgAl-LDH	SAIMs	Co-precipitation	Ni : Ga = 1 : 1	C_2H_2 hydrogenation	165
RuCo/N-doped carbon	SAAs	Co-precipitation & pyrolysis	Ru : Co = 0.016 : 1	Levulinic acid hydrogenation	166
PdCu/ND	DACs	Sequential precipitation	Pd : Cu = 1 : 1	C_2H_2 hydrogenation	37
$PdIn/MgAlO_4$	SAIMs	Hydrothermal	Pd : In = 1 : 1	C_2H_2 hydrogenation	167
$IrMo/TiO_2$	DACs	Wet impregnation & pyrolysis	Ir : Mo = 1 : 1	Hydrogenation of 4-nitrostyrene	168
$PdFe/Fe_2O_3$	DACs	Wet impregnation & photochemically synthesis	—	C_2H_2 hydrogenation	169
RuNi/LDHs	SAAs	*In situ* growth method & galvanic displacement	Ru = 0.4 wt%	Hydrogenation of nitroarenes	170
$PtCu/Al_2O_3$	SAAs	Galvanic displacement	Pt : Cu < 1 : 100	Hydrogenation of 1,3-butadiene	171
Pd–Mn/NC	DACs	Co-precipitation with hydrothermal & pyrolysis	Pd : Mn = 1 : 2	Phenylacetylene semi-hydrogenation	172
$Pd–Ru/Zr(HPO_4)_2$	DACs	Cross-linkage of ionic inorganic oligomers assistance	Pd : Ru = 5 : 95	Phenylacetylene semi-hydrogenation	173
Pd–Ru/ZIF-8	DACs	Co-precipitation	Pd : Ru = 7 : 3	Phenylacetylene semi-hydrogenation	174
$Pt–Pt/C_3N_4$	DACs	*In situ* precipitation	—	Hydrogenation of nitrobenzene	175
$AgPd/SiO_2$	SAAs	Incipient wetness co-impregnation	Pd : Ag = 1 : 100	C_2H_2 hydrogenation	176
PdAu/C	SAAs	Incipient wetness impregnation	Pd : Au = 5 : 95	CO_2 hydrogenation	177
PtZn/HNCNT	SAIMs	Incipient wetness impregnation & *in situ* reduction	—	4-Nitrophenylacetylene hydrogenation	41
CoRu/N-doped carbon	SACCs	Wet impregnation & vacuum freeze dried	Ru : Co = 1 : 5	NH_3 synthesis	178
$Pt/NiCo(OH)_2$	SACCs	Co-precipitation & galvanic displacement	—	Hydrogenation of nitroaromatics	179
$NiRu/CeO_2$	SAC-NPs	Sequential precipitation	Ru : Ni = 1 : 5	CO_2 Methanation	180
$NiPd/Al_2O_3$	SAC-NP	Wet co-impregnation	Ni : Pd = 1 : 1	Semi-hydrogenation of phenylacetylene	181
$Ru_1–Ru$ NP/CMF	SAC-NPs	Incipient wetness impregnation	—	Hydrogenation of levulinic acid	182
$Ir_1–Ir$ NP/CMK	SAC-NPs	Two step wet impregnation	—	Hydrogenation of quinoline	183
$Pd_1–Pd$ NP/TiO_2	SAC-NPs	Spray pyrolysis	—	Selective hydrogenation of ketone/aldehydes	184

on the advantage of SACs, the introduction of bimetallic systems at the atomic level shows extra synergistic effects between two active components, offering more possibilities in structural regulation and practical usage, including in the hydrogenation reactions discussed in this review.[187,188] Fig. 12 gives the five main structure modes of bimetallic SACs, which are single atom alloys (SAAs),[189] single atom sites-clusters (SACCs),[187,190] single atom sites & nanoparticles (SAC–NPs),[186] dual atom catalysts (DACs),[191] and single atom site-intermetallics (SAIMs).[165,192] Based on the concluded research shown in Table 2, in this section, a detailed review will be given for the five structures of bimetallic SACs mentioned above to develop a better understanding of the synthesis strategies and regulation methods of these materials.

3.2.1 Single atom alloys (SAAs). According to the definition given by Sykes *et al.* in 2020, single atom alloys (SAAs) were described as a bimetallic single-site heterogeneous catalyst in which small amounts of one metal are atomically dispersed on the surface of a different metal.[189] A typical SAA structure contains a more catalytically active metal that is alloyed onto the surface of a more inert and catalytically selective host metal. Generally, to ensure the formation of isolated individual atoms in alloys, small or even trace amounts of active metal species are used in the synthetic process of SAA construction.[163,193,194] To achieve this, efforts have been made to develop simple and effective methods for SAA synthesis since this is a prerequisite for developing cost-effective catalysts.

As we discussed in section 3.1.1, incipient wetness co-impregnation is a simple, one-pot method for catalyst preparation, which has also been widely used for SAA synthesis. Chai *et al.* used $AgNO_3$ and $Pd(NO_3)_2$ as metal precursors and co-impregnated them onto a pretreated Al_2O_3 support to obtain atomically dispersed Pd alloyed with Ag particles loaded on Al_2O_3.[193] As shown in Fig. 13(a), KOH was initially introduced to modify the surface of α-Al_2O_3 to allow better adsorption of metal cations using electrostatic effects. Then a trace amount of Pd precursor was mixed with an Ag precursor and added to the α-Al_2O_3 support, followed by a

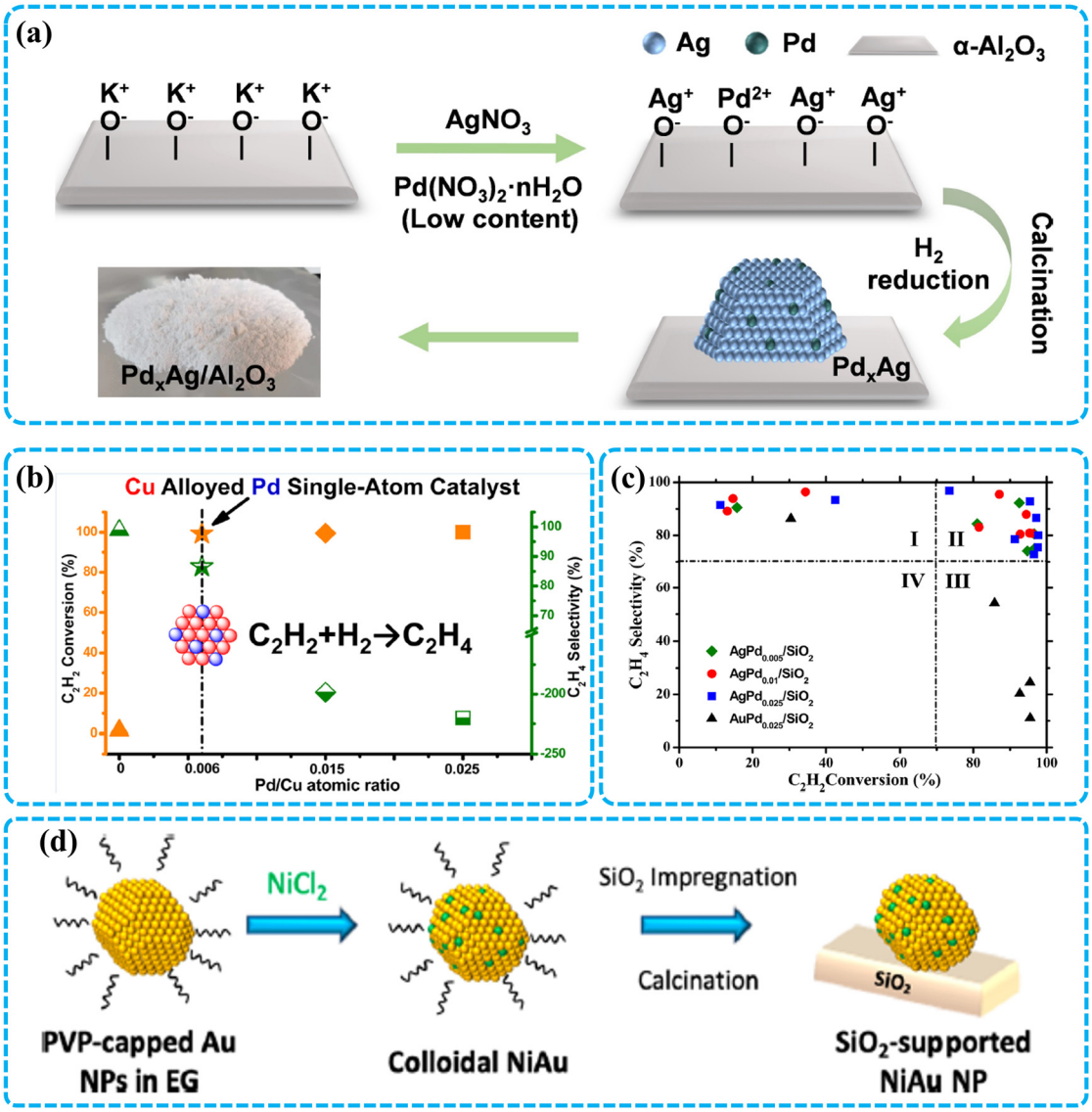

Fig. 13 (a) Schematic illustration of the synthesis process of the Pd_xAg/Al_2O_3 catalyst; (b) catalytic performance distribution of the alloyed Pd supported catalyst with different Pd/Cu atomic ratios obtained by the incipient wetness co-impregnation method; (c) catalytic performance distribution of the Ag alloyed Pd supported catalyst with different Pd/Ag atomic ratios obtained by the incipient wetness co-impregnation method; (d) schematic illustration of the sequential reduction method for the synthesis of SAAs [panel (a) has been reproduced with permission from ref. 193, Copyright 2023, European Chemical Societies Publishing. Panel (b) has been reproduced with permission from ref. 35, Copyright 2017, American Chemical Society. Panel (c) has been reproduced with permission from ref. 176, Copyright 2015, American Chemical Society. Panel (d) has been reproduced with permission from ref. 189, Copyright 2020, American Chemical Society].

post-thermal treatment for getting the dilute Pd/Ag alloy which had an atomic ratio of Pd : Ag of 0.04 : 1. Due to the highly active Pd species and its atomic level dispersion, the reported catalysts showed over 90% of yield in a 100 h catalyst test in the selective hydrogenation of acetylene. Fig. 13(b) and (c) show the catalytic performance distribution of the selective hydrogenation of acetylene over Pd–Cu/SiO_2 and Pd–Ag/SiO_2 SAAs prepared by the incipient wetness co-impregnation method. The best balance of conversion and selectivity was achieved when 0.6% Pd species were diluted in hosted Cu metal and 1% Pd for Ag, respectively. The above results provide evidence for the possibility of synthesizing SAAs through a simple strategy, and the high atomic utilization with such small metal loadings. Besides, as a multi-step preparation strategy for SAAs, sequential reduction can precisely control the composition and structure of catalysts.[187] In short, sequential reduction requires the seed preparation of the first metal, while the secondary metal is added into the seed to form SAAs with controlled loadings. As shown in Fig. 13(d), Au nanoparticles were first prepared by reducing an Au precursor, then $NiCl_2$ was added into the dispersed PVP–Au NPs as a secondary metal precursor and reduced in ethylene glycol.[189] Finally, the unsupported NiAu SAAs were loaded onto the substrate by a simple

impregnation method. Compared to the method where the metal precursor is randomly reduced on the substrate, this method has the advantage of having controllable alloy formation due to the prior preparation of SAAs before loading the active species onto the support. Furthermore, galvanic displacement (GD) can also be used for the preparation of SAAs due to its advantageous *in situ* deposition, and no external current is required, which is suitable for depositing secondary active metal onto the anchored host metal. As shown in Fig. 10(b), Pt–Cu SAAs were synthesized by the GD method using Cu particles that were reduced *in situ* from CuMgAl-LDHs.[142] Liu *et al.* reported a Ru–Ni SAA in which Ru single atoms are anchored onto Ni NPs in a NiAl-LDH system through the GD method.[170] The Ru weight loading was precisely controlled (<0.4 wt% to Ni) to ensure that Ru exists on the Ni surface as single atoms rather than as clusters. The prepared RuNi SAAs exhibited improved activity and high selectivity towards the selective hydrogenation of 4-nitrostyrene to 4-aminostyrene due to the Ni-coordinated single atom Ru sites.

In addition to the above synthetic methods, other novel strategies were also investigated for high-performance SAAs. Zhong *et al.* reported a Pd–Ni SAA supported on SiO_2 prepared by the atomic layer deposition (ALD) method, aiming to overcome the difficulty that Pd active sites cannot be exposed on the catalytic surface through conventional impregnation methods, to further improve the atomic utilization of SAAs.[195] Fig. 14(a) gives a comparison of synthesized Pd–Ni/SiO_2 SAAs by wet co-impregnation and ALD, respectively. It can be seen that uniform Pd sites can be dispersed on the outermost surface of supported Ni NPs in the ALD route instead of being distributed in a random, aggregated form on the Ni NPs or the surface of the support. Besides, Shao *et al.* reported a Ru–Co SAA catalyst with precisely modulated electron-rich Ru atoms confined to the Co lattice, prepared by pyrolysis of Ru-containing ZIF-67, which was obtained through a one-step polymerization synthesis (Fig. 14(b)).[166] The structured ZIF-67 precursor can confine Ru and Co, preventing aggregation during the pyrolysis process to obtain a Ru–Co/N-doped carbon catalyst with dispersed single atoms of Ru. Meanwhile, as shown in Fig. 14(c), highly coordinated Ru sites in the Co lattice resulted in a precisely regulated electronic structure on the atomic scale, which means the electronic effect between the two metals promotes the shift of electrons from Co to Ru sites, greatly improving the catalytic activity of hydrogenation from levulinic acid to γ-valerolactone.

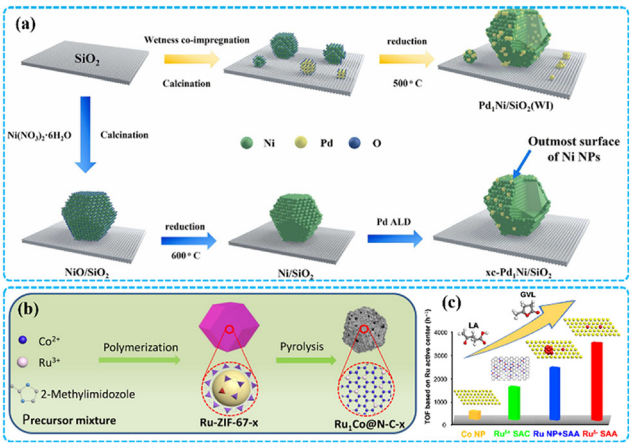

Fig. 14 (a) Schematic illustration of synthesis of Pd_1Ni/SiO_2 by wetness co-impregnation and atomic layer deposition; (b) schematic illustration of the synthesis process of RuCo SAAs on N-doped carbon by pyrolysis of Ru-containing ZIF-67; (c) turnover frequency comparison over Ru-based single atom catalysts on hydrogenation of levulinic acid [panel (a) has been reproduced with permission from ref. 195, Copyright 2023, Elsevier. Panels (b and c) have been reproduced with permission from ref. 166, Copyright 2021, American Chemical Society].

3.2.2 Single atom sites – cluster (SACCs). As a metal particle on the sub-nanometer scale, clusters are generally defined as a collection of several to dozens of metal atoms with a diameter of around 1 nm.[186] Clusters have received great attention due to their diverse coordination structures, which cause different catalytic behaviors than metal NPs and SACs. For example,[196] for gold clusters (Au_n, n is the number of metal atoms in the cluster) with fewer than 8 Au atoms, Au_n clusters have a planar structure consisting of several localized Au atoms with unsaturated coordination environments, which mainly contributes to their frontier orbitals. However, when $n \geq 8$, the geometric structure of Au_n will change in three dimensions, increasing the coordination number of the surface atoms, leading to contributions to the frontier orbitals from the atoms inside the particles. On the other hand, it has been shown that when the atomicity of metal particles is gradually reduced from NPs to sub-nanometer clusters, the electronic structure changes from continuous metal energy levels to split molecular orbitals.[186,197] Thus, one can reasonably expect that coupling

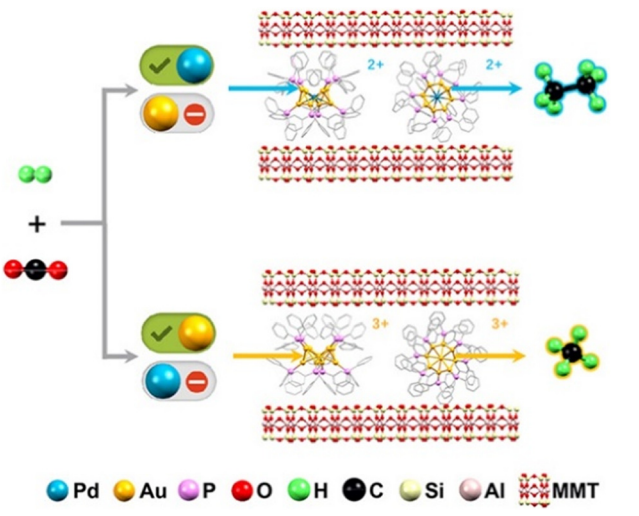

Fig. 15 Different catalytic behavior between Au_8Pd_1 and Au_9 clusters over CO_2 hydrogenation [panel has been reproduced with permission from ref. 198, Copyright 2021, Chinese Chemical Society Publishing].

nanoclusters with single atom sites as multi-active sites can directly simplify the catalytic process for complex reactions.

Cai *et al.* successfully synthesized a heterogeneous catalyst containing Au_9 and Au_8Pd_1 clusters intercalated into montmorillonite for CO_2 hydrogenation.[198] Experimentally, pre-prepared $[Au_9(PPh_3)_8]^{3+}$ and $[Au_8Pd_1(PPh_3)_8]^{2+}$ complexes were confined into the layered montmorillonite structure through a simple wet mixing process. As shown in Fig. 15, the central Au atom of the Au_9 cluster was substituted by one Pd atom that forms Au_8Pd_1 SACCs, giving the ability to control the reaction pathway of CO_2 hydrogenation to produce C_2H_6 rather than CH_4. It has been proven that the substitution of a Pd atom for the central gold atom can reduce the migration and rearrangement of Au during the catalytic process, thereby significantly reducing the tendency of structural variation caused by changes in the coordination number of surface Au sites during the catalytic reaction. This work shows the possibility that the transformed products of CO_2 can be readily changed by altering the composition of cluster catalysts. Zhang *et al.* used vacuum-freeze-drying and high-temperature pyrolysis methods for preparing Co–Ru/N-doped carbon (N-C) with atomic cobalt anchored on sub-nanometer Ru clusters, which can be applied in the process to synthesize ammonia.[178] Precursors of Ru and Co were mixed in DMF solvent before being added into the N-C suspension through wet-impregnation, and this was then followed by a pyrolysis process to remove the organic solvent. According to the report, the spatial effect generated by the single atom & cluster structure induces strong interelectronic interactions between Co and Ru, which can cause the high-surface-unoccupied Co 3d charge and obvious upshifting of the Ru d-band center simultaneously. Furthermore, Zhu *et al.* found that the ensemble of Pt single atoms and clusters can be deposited on bimetallic hydroxide ($(Ni,Co)(OH)_2$) with a one-step GD process.[179]

3.2.3 Single atom sites – intermetallic (SAIMs). Unlike the random distribution of dopant metals in SAAs, single atom sites – intermetallic (SAIMs) always exist as a well-defined atomic structure due to their fixed ratio, regular arrangement, and homogeneous distribution of the two

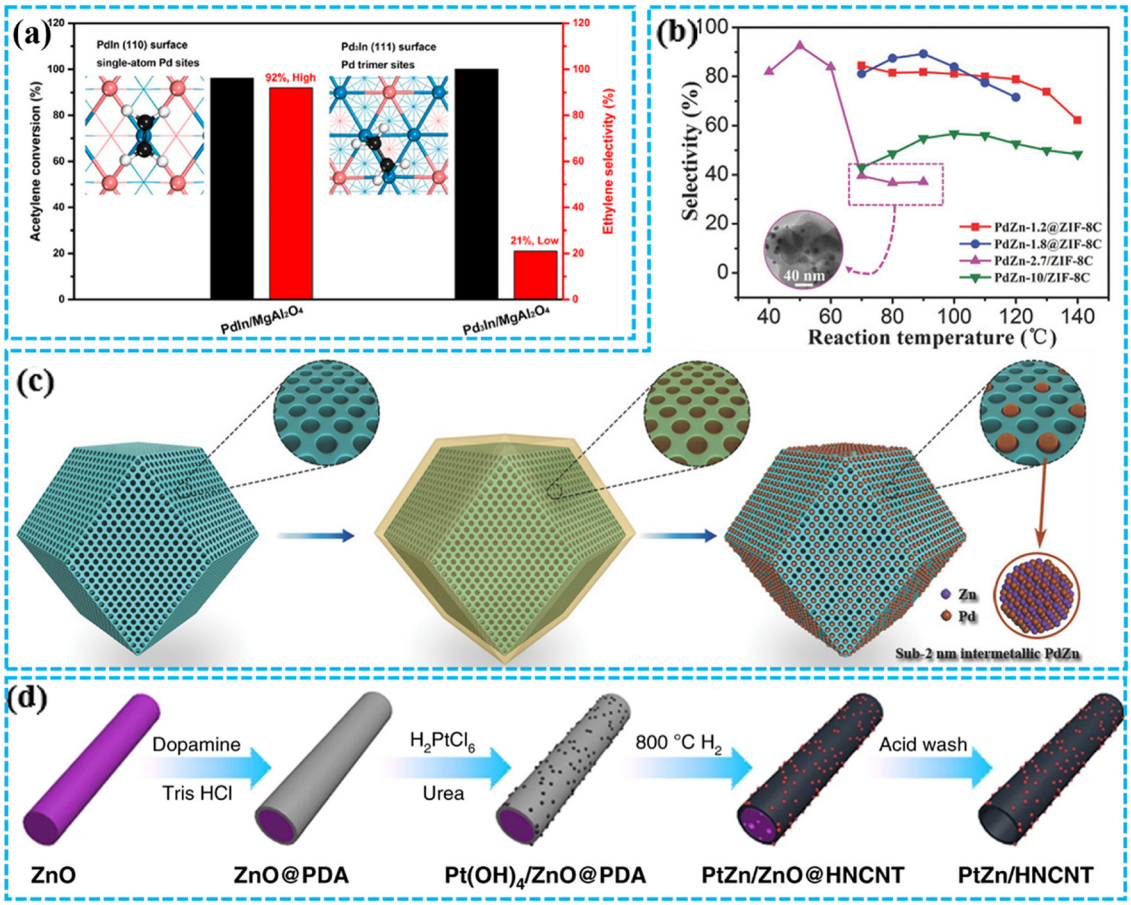

Fig. 16 (a) Atomic configuration and catalytic performance differences of intermetallic PdIn (110) and Pd_3In (111); (b) schematic synthesis process of PdZn-sub-2@ZIF-8 with a MOF-confined co-reduction strategy; (c) catalytic stability test over PdZn-1.2@ZIF-8 as a function of time at 115 °C for C_2H_2 selective hydrogenation to C_2H_4; (d) schematic synthetic process of atomic regulated PtZn intermetallic nanoparticles supported on hollow nitrogen-doped carbon nanotubes (PtZn/HNCNT) [panel (a) has been reproduced with permission from ref. 167, Copyright 2017, American Chemical Society. Panels (b and c) have been reproduced with permission from ref. 192, Copyright 2018, Wiley-VCH. Panel (d) has been reproduced with permission from ref. 41, Copyright 2019, Springer Nature].

metal elements.[186] Since the concentration of dopant atoms in SAIMs is much greater than in SAAs, researchers prefer to classify SAIMs as nanocatalysts instead of single-atom catalysts.[189,199] However, in this review, a brief introduction of SAIMs will be given due to their properties of regulating the doped metal elements with atomic scale dispersion, even though the overall intermetallic active sites are typically supported nanoparticles. As shown in Fig. 16(a), Li and colleagues compared the catalytic performance of the supported PdIn (110) surface with single-atom Pd site exposure and the Pd_3In surface with Pd trimer site exposure for the semi-hydrogenation of alkynes.[167] The isolated Pd atoms of the PdIn (110) surface displayed a much higher selectivity to C_2H_4 than Pd_3In, in accordance with the atomic separation of their Pd sites, which was consistent with the classic adsorption model of acetylene hydrogenation. The study also proved that the constructed intermetallic structure between Pd and In can effectively confine the single Pd sites and endow the catalysts with long-term stability. For the same hydrogenation process, Li *et al.* also reported ultrasmall MOF-confined atomically ordered intermetallic PdZn nanoparticles by impregnating the Pd precursor into the well-defined porous structure of ZIF-8, which was followed by a co-reduction process.[192] As shown in Fig. 16(b), the uniform pores of ZIF-8 acted as cages to effectively restrict the aggregation of intermetallic particles during preparation, resulting in excellent size uniformity and thermal stability of the sub-2 nm PdZn nanoparticles. Besides, due to the confinement effect of the pore-structured ZIF-8, the size of the intermetallic Pd–Zn nanoparticles can be controlled by increasing or decreasing the amount of Pd precursor. Fig. 16(c) shows that PdZn-sub-2@ZIF-8C remains stable during a 12 h test at a relatively high temperature for the C_2H_2 semi-hydrogenation reaction. Besides, *in situ* reduction can also be used to support Pd–Zn intermetallic nanoparticles on hollow nitrogen-doped carbon nanotubes (HNCNT).[41] As presented in Fig. 16(d), ZnO nanotubes were synthesized as initial templates for the growth of the PDA support. Then, $Pt(OH)_4$ was deposited onto the outer surface of PDA through the DPU route, which was then followed by a reduction step that allowed the inner ZnO to migrate to the outer surface and combine with Pd. Finally, the ZnO template was sacrificed by acid wash. In PdZn/HNCNT, the original contiguous Pd atoms were isolated with the Zn atoms doping the lattice. As we discussed in section 2.1, the catalytic performance of the selective hydrogenation of 4-nitrophenylacetylene was greatly improved because of the geometric effect caused by PdZn intermetallic structure.

3.2.4 Diatomic sites. In recent years, diatomic catalysts have started to show greater research value and broader development potential than monoatomic catalysts due to their unique synergistic effects and electronic modulation capabilities.[191,200] Generally, according to the interacting structure of dual metal sites, diatomic sites can be classified into dual-single-atom catalysts (DSACs) and dual-atom catalysts (DACs).[187,200] For DSACs, two types of metal atoms are unconnected and distributed randomly on the support surface, while DACs contain active sites with two adjacent atoms of differing species that interact as dual-atomic pairs through direct bonding (M1–M2) or with heteroatom bridging (M1–N–M2).[201]

Li *et al.* developed mesoporous silica stabilized Pd–Ru/ZIF-8 DSACs with isolated Pd and Ru single atomic sites for phenylacetylene semi-hydrogenation.[174] In a two-step synthesis process, Pd–Ru/ZIF-8 was initially prepared by cation substitution during the synthesis of ZIF-8, where partial Zn atoms originally used as metal nodes were replaced with single Pd and Ru atoms. Then, a thin layer of ordered mesoporous silica was introduced on the surface of Pd–Ru/ZIF-8 through the precipitation method under mild conditions. The Pd–Ru DSAC shows 98% conversion of phenylacetylene, 96% selectivity to styrene and a turnover frequency of up to 25× that of its monoatomic Pd counterpart (Pd/ZIF-8). The superior performance was attributed to the synergistic effect of anchored dual-single-atom sites as metal nodes in the ZIF-8 structure, where Pd can coordinate with the benzene ring to activate phenylacetylene and Ru can activate hydrogen for the reaction with C≡C. Furthermore, the coverage of highly ordered mesoporous silica can improve the stability of Pd–Ru/ZIF-8 without blocking the active sites, which allows the catalyst to maintain performances in five test cycles. For the same hydrogenation reaction, Sun *et al.* proposed an innovative idea for a Pd–Ru DSAC system with highly dilute Pd and Ru atomic sites, which are dispersed in an amorphous zirconium hydrogen phosphate matrix by cross-linking ionic inorganic oligomers (Zr^{4+}, Pd^{2+}, Ru^{2+}, and PO_4^{3-}).[173] The synthesis approach has the potential for scale-up and universality to other DSAC systems due to its rapid and mild aging process for the mixed metal precursors and freeze-drying of the final products. Furthermore, Fu *et al.* successfully synthesized DSAC Ir_1Mo_1/TiO_2 based on the redistribution behavior of bimetallic carbonyl clusters of $Ir_2Mo_2(CO)_{10}(\eta^5\text{-}C_5H_5)_2$ on reducible support surfaces after the loss of the protective ligands during pyrolysis under an Ar atmosphere.[168] For hydrogenation of 4-nitrostyrene to 4-vinylaniline, a clear synergistic cooperation effect has been shown by experimental and computational results in which Ir_1 sites contribute to the activation of H_2 molecules while Mo_1 sites are responsible for the adsorption of 4-nitrostyrene, resulting in a great increase in performance with the prepared Ir_1Mo_1/TiO_2 in comparison to the corresponding SACs: Ir_1/TiO_2 and Mo_1/TiO_2.

For DACs, superior catalytic performances rely more heavily on the rationally tailored coordination environment formed between the first and second metals. Fig. 17(a) shows the outstanding catalytic yield of low-temperature C_2H_2 semi-hydrogenation over DACs with a bonded Pd_1–Cu_1 atomic pair anchoring on nanodiamond graphene (ND@G) fabricated by Huang and their colleagues.[37] In a sequential precipitation process, atomic Cu sites are precipitated and deposited onto the prepared ND@G through long-time stirring, then a highly

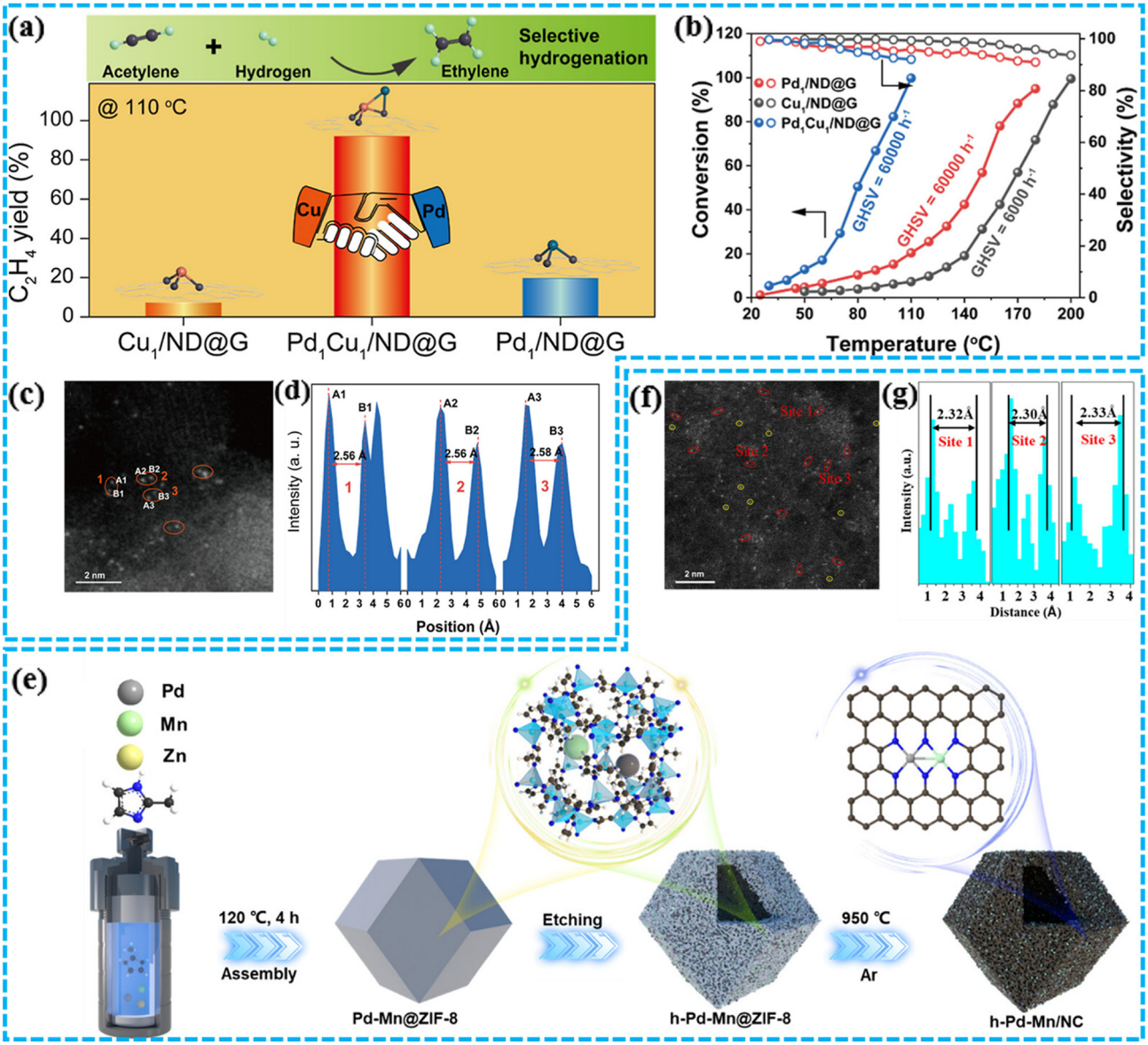

Fig. 17 (a) Yield comparison between Pd_1Cu_1, Cu_1 and Pd_1 supported on nanodiamond graphene (ND@G); (b) HAADF-STEM images of Pd_1Cu_1/ND@G (orange ovals: Pd–Cu atomic pairs; white circles: single-atom Cu or Pd atoms); (c) intensity profile of ovals 1, 2, and 3 in the HAADF-STEM image; (d) C_2H_2 conversion rate and C_2H_4 selectivity as a function of temperature over Pd_1Cu_1/ND@G, Cu_1/ND@G and Pd_1/ND@G; (e) schematic illustration of the synthesis process of h-Pd–Mn/NC; (f) HAADF-STEM image of h-Pd–Mn/NC (red circles: Pd–Mn atom pairs); (g) intensity profile of sites 1, 2, and 3 in the HAADF–STEM image [panels (a–d) have been reproduced with permission from ref. 37, Copyright 2022, American Chemical Society. Panels (e–g) have been reproduced with permission from ref. 172, Copyright 2024, American Chemical Society].

diluted Pd precursor (1.6 ppm) was added into Cu_1/ND@G to fabricate the Pd_1–Cu_1/ND@G sample. Fig. 17(b and c) demonstrates the existence of well-defined Pd_1–Cu_1 pairs with a constant bond length of ~2.6 Å. Compared to Pd_1/ND@G and Cu_1/ND@G, the prepared DAC sample displays a much greater catalytic performance, particularly with its ability to engage in the hydrogenation process at low temperatures, as shown in Fig. 17(d). The enhanced activity was attributed to the altered reaction path and reduced reaction barrier of hydrogenation, which was caused by the bonded atom pairs that promote the adsorption of C_2H_2, facilitate H_2 adsorption and dissociation, and convert the competitive adsorption of reactant species to non-competitive adsorption. In a single step, Gao *et al.* applied the photoinduced deposition method to anchor single Pd atoms on the surface of α-Fe_2O_3 (012) to form Pd–Fe diatomic pairs with the capability of breaking the trade-off between catalytic activity and selectivity for low-temperature semi-hydrogenation of alkynes.[169] The strong electronic coupling between Pd–Fe pairs leads to d-electron domination near the Fermi level and results in an enhanced ability to adsorb and disassociate H_2, while Pd atomic sites enable the preferential desorption of C_2H_4 as the final product. DACs with metal atom pair structures can also exist in a homonuclear form.

Studies have shown that homonuclear DACs can also meet the catalytic activity requirements of a bimetallic system. For example, Li's research group reported a heterogeneous catalyst with dual-atom Pt pairs (Pt_2) depositing on mesoporous graphitic carbon nitride (mpg-C_3N_4), which shows excellent catalytic performance for the selective hydrogenation of nitrobenzene to aniline.[175] Like the bimetallic metal pairs discussed above, Pt_2 active sites also show superior ability to disassociate H_2, which results in a higher conversion when compared to a single atom of Pt or Pt nanoparticles. Chu *et al.* utilized electrostatic adsorption between $PdCl_4^{2-}$ and amine-modified surfaces of SiC to prepare monodisperse Pd diatomic pairs (Pd_2) for hydrogenation of carbon–halogen bonds.[202] The prepared sample showed both high conversion and selectivity for the cleavage of the carbon–halogen bond because of the synergistic interaction of neighboring Pd sites, which can lower the activation energy for hydrogenation and promote the desorption of products. Except for dual-atomic pairs through direct bonding (metal–metal), DACs also include the heteroatom coordination connected by bridging atoms. Fig. 17(e) shows the synthesis process of DACs containing dual-atomic Pd–Mn pairs dispersed on nitrogen carbon (Pd–Mn/NC) proposed by Li's group.[172] Briefly, Pd–Mn/ZIF was initially prepared through a hydrothermal route followed by an etching step with tannic acid to obtain the hollow mesoporous structure. Then, the final Pd–Mn/NC sample was obtained through pyrolysis of the sample from the previous step at high temperature in an Ar atmosphere. The existence of Pd–Mn atomic pairs was proved, and the distance between atoms was measured as 0.23 nm (Fig. 17(f and g)). It is clear that Pd and Mn were anchored to the framework as metal nodes connected through a N atom (Pd–N–Mn). The strong electronic structure of the Pd–Mn coupling originates from facilitated electron transfer from the Mn site with weak electronegativity to the adjacent Pd site, which enhances the d-electron advantage near the Fermi level, not only promoting the adsorption of H_2, but also improving the adsorption of large molecular reactants on Pd single atom sites in the hydrogenation process, such as phenylacetylene.

3.2.5 Single atom sites with nanoparticles (SAC–NPs). For the improvement of SACs, there is a strategy of introducing independent metallic nanoparticles to the support as synergistic active sites in conjunction with the single atom sites to facilitate the reaction process.[187] However, it is a challenge to establish heterogeneous deposition of two kinds of active sites, one on the atomic scale and the other on the nanoscale, simultaneously because of the existing competition during the synthesis.[187,203] Song *et al.* reported a SAC–NP structure with single atom Ni-modified Pd/Al_2O_3

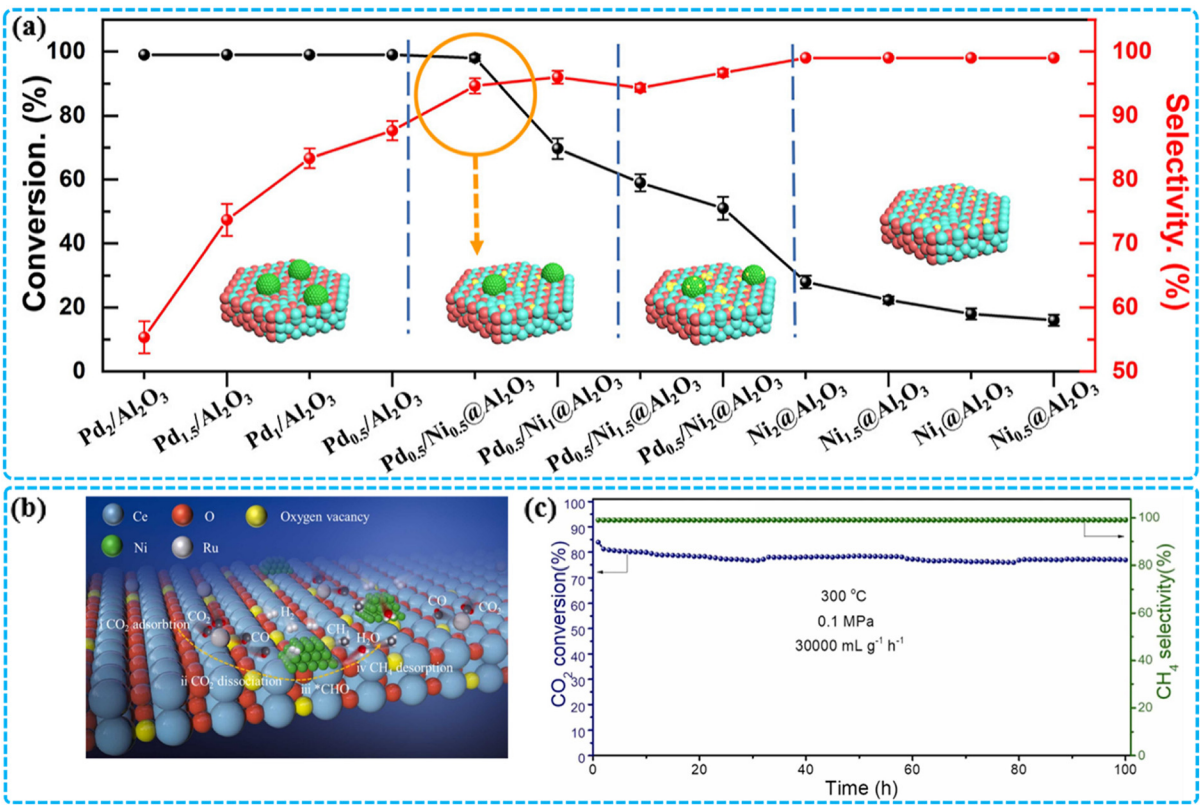

Fig. 18 (a) Comparison of conversion and selectivity of $PdNi/Al_2O_3$ catalysts with different metal loadings; (b) the proposed synergistic mechanism of the Ru_1Ni_{NP}/CeO_2 catalyst for boosting CO_2 methanation; (c) lifetime test of catalytic performances over Ru_1Ni_{NP}/CeO_2 at 300 °C [panel (a) has been reproduced with permission from ref. 181, Copyright 2022, American Chemical Society. Panels (b and c) have been reproduced with permission from ref. 180, Copyright 2023, Elsevier].

nanoparticles for the semi-hydrogenation of phenylacetylene at mild temperatures.[181] The Ni-modified Pd/Al_2O_3 nanoparticles with different metal loading ratios of Pd : Ni were synthesized *via* wet-impregnation and contained single atoms of lattice-embedded Ni alongside Pd nanoparticles on the support surface. Fig. 18(a) shows the comparison of catalytic performances of Pd_xNi_y/Al_2O_3 SAC–NPs under mild conditions (298 K, 0.1 MPa), and it is clear that the $Pd_{0.5}$-$Ni_{0.5}/Al_2O_3$ sample has a favourable trade-off between conversion and selectivity, achieving 98% and 94% of each, respectively. The anchored Ni atoms allow the support to receive the shifted electrons from the Pd sites and thus make it easier for the Pd particles to adsorb the electron-rich phenylacetylene. For the CO_2 hydrogenation process, CeO_2 was proven as an unreactive support and with a very limited promotion effect.[204,205] However, according to the utilized abundant oxygen vacancies and high affinity of surface lattice oxygen atoms on the CeO_2 surface,[206] Zhang *et al.* successfully synthesized CeO_2 nanorods with co-deposition of Ru atoms and Ni nanoparticles with simple wet impregnation for boosting CO_2 methanation.[180] As shown in Fig. 18(b), the dual-active-site system works synergistically with high sensitivity of atomic Ru_1 for converting CO_2 to CO and highly efficient Ni particles for the CO methanation step. In a 100 h test, the prepared Ru_1Ni/CeO_2 displayed a stable catalytic performance with over 80% conversion and 99% selectivity (Fig. 18(c)). Furthermore, similar to DACs with deposition of dual active components on a single support surface, there is also research on SAC–NPs for synthesizing monometallic active species with the coexistence of atomic sites and nanoparticles.[182–184] In Cárcamo's work, multi-cycle synthesis of wet impregnation was utilized for preparing Pd_x(SACs&NP) on carbon nanotubes with carbon defects caused by nitric acid pretreatment, where x refers to the ratio of Pd atomic sites and Pd nanoparticles.[203] The precisely controlled x depended on the number of deposition cycles, namely the trend of transformation from single atomic Pd to assembled Pd particles. Shen *et al.* synthesized a mesoporous carbon CMK-3 supported Ir_{1+NP} SAC–NPs catalyst by a simple adsorption and subsequent calcination method.[183] The synergistic effect between Ir_1 and Ir_{NP} was attributed to the adsorption and activation of quinoline (reactant) by Ir_1 and the boosted H_2 dissociation by Ir_{NP}, which offered the catalyst a much-improved TOF of 7800 h^{-1} over that of the Ir_1/CMK or Ir_{NP}/CMK counterpart samples.

3.3 Metal–support interaction effect (MSI)

As we discussed in the above sections, the modulation of supports for optimizing heterogeneous catalysts is one of the efficient tools that are able to enhance catalytic performances.[86,111,192] In recent years, the investigation of metal–support interactions (MSI) has received much attention based on diverse catalysts and modification strategies.[207] The main consideration is to immobilize metal active sites on the support to control their spatial distribution and enhance the stability of the catalyst. The interfacial interaction between the metal and support has been

Table 3 List of representative work of building bi(multi)metallic catalysts with different metal–support interactions, synthesis, and applications

Support effect	Catalysts	Method	Hydrogenation reaction	Ref.
SMSI	NiBa/anatase TiO_2	Sequential impregnation method & H_2 reduction@673 K 1 h	Guaiacol hydrodeoxygenation	211
	$PdTi/SiO_2$	Sequential incipient wetness impregnation	Propylene hydrogenation	212
	$NiFeO/CeO_2$	Deposition precipitation method	CO_2 hydrogenation	213
	$PtPdCu/Al_2O_3$	One-pot colloidal method & ligand exchange & low-temperature annealing	Hydrogenation of nitrobenzene	214
	$RuMo/MoO_3$	Co-impregnation method & calcination@773 K & 4 h	CO_2 hydrogenation	215
EMSI	$NiRu/SiO_2$	Strong electrostatic adsorption	Biphenyl selective hydrogenation	91
	$IrTi/TiO_2$	Colloid-deposition method & reduction@773 K	Hydrogenation of acetophenone	216
	Ni_3Fe/rutileTiO_2	Hydrothermal method & calcination and reduction@773 K	Hydrogenation of fatty acids	217
	$CuZn/ZnO/SiO_2$	Single solid precursor-derived 3D nanowire networks of CuZn-silicate	CO_2 hydrogenation	218
	$PdCu/TiO_2$ P25	Co-impregnation method	CO_2 hydrogenation	219
	$PtSn/MoO_x$	Impregnation method	Hydrogenation of functionalized nitroarenes	220
	Ir/Mo–KIT6	One-pot hydrothermal method & incipient wetness impregnation	Hydrogenation of amides	221
	PtPd/C	Deposition–precipitation method & reduce in H_2@573K 5 h	Transfer hydrogenation of glycerol	222
Structured supports	PdCo/mesoporous SiO_2	One-pot ligand-protected synthesis strategy	CO_2 hydrogenation to formates	223
	PdAu/raspberry colloid templated SiO_2	Raspberry colloid-templating strategy	Hydrogenation of 1-hexyne	224
	$AuPd/UiO\text{-}66\text{-}NH_{2\text{–}2}$	Ligand-protected synthesis	CO_2 hydrogenation	225
	PdMn/silicalite-1 zeolites	Ligand-protected synthesis	CO_2 hydrogenation	226
	CuCo/carbon	One-step solvothermal synthesis of MOF & pyrolysis	Furfural hydrogenation	227

recognized as a key factor in the resulting performance of metal active sites.[208,209] The concepts of strong metal–support interactions (SMSI) and electronic metal–support interactions (EMSI) have been extensively studied.[210] The representative work related to the modification with SMSI and EMSI on bimetallic hydrogenation catalysts is listed in Table 3 with their respective synthesis methods and reaction systems. In addition, structured supports that have geometric or spatially constraining effects on bimetallic active sites will also be explained in detail in this section to comprehensively illustrate the regulatory effect of the support.

3.3.1 Strong metal–support interaction (SMSI). The concept of SMSI originated from the observation that the H_2 and CO chemisorption abilities of Pt-group metals were reduced by interactions with TiO_2 after a high-temperature reduction step due to the supported metals being encapsulated by a reducible oxide overlayer.[228] Meanwhile, this encapsulation phenomenon causes an immobilization effect on the surface active sites, which results in enhancing the stability of supported catalysts by preventing sintering during reaction, though part of the catalytic activity will be sacrificed due to the blocking of the active sites in some cases.[210] Fig. 19(a) shows the supported Co–Ni bimetallic alloy catalysts prepared through the incipient wetness co-impregnation method, followed by calcination under N_2 to partially reduce the support, where TiO_2 was reduced to a TiO_x layer and Nb_2O_5 forms NbO_x.[85] SMSI between encapsulated Co–Ni particles and TiO_x or NbO_x greatly enhanced the catalytic stability over a sample of CoNi supported on nonreducible α-Al_2O_3 during a 100 h stability test for Fischer–Tropsch synthesis as a result of preventing particle growth. In addition, a recent study shown in Fig. 19(b) provided a method to avoid the sintering of Ru nanoparticles by fabricating a composite support for creating enhanced SMSI.[229] In short, the robust Ru-based catalyst benefits from the dual-component support, which simultaneously avoids the migration and sintering of active sites during Fischer–Tropsch synthesis, where the hydrophobic carbon layer contributes to hindering Ostwald ripening, while TiO_2 avoids particle migration and coalescence through the SMSI generated between Ru and itself.

To establish SMSI, most research is based on the strategy of inducing *in situ* secondary growth of reducible supports around active sites through pyrolysis or high-temperature reduction.[215,230–232] Generally, the partially reduced external layer of the support binds with the active sites in the form of an overlayer or dopant. Typically, in the study shown in Fig. 19(c), SMSI was induced *via* the conditions of the CO_2 hydrogenation process, which transformed the catalyst $H_{0.34}MoO_3$-supported Ru nanoparticles into Ru/MoO_2 covered by a reduced MoO_{3-x} layer.[215] The structure of encapsulation overlayers not only enhanced the long-term stability of the catalyst but also switched the reaction pathway from methanation to RWGS. More importantly, the MoO_{3-x} layer could be removed with oxidation treatment,

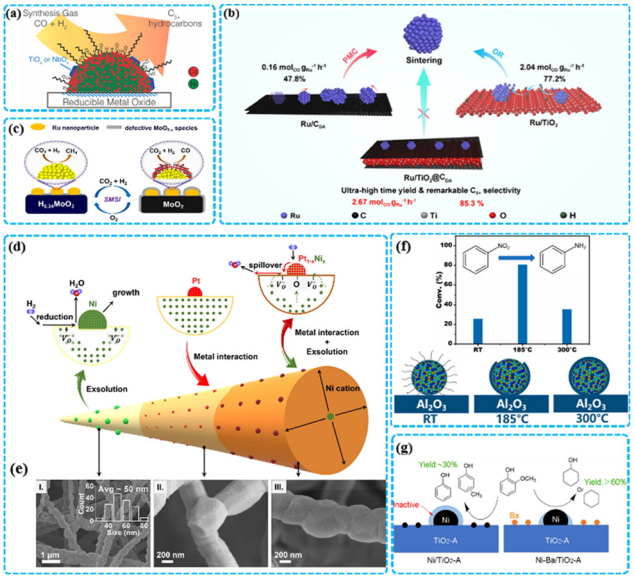

Fig. 19 Schematic illustration of (a) CoNi bimetallic sites loaded on reducible oxide supports with SMSI; (b) hydrophobic carbon-encapsulated TiO_2-supported Ru catalyst in Fischer–Tropsch synthesis; (c) SMSI of Ru nanoparticles encapsulated by the partially reduced MoO_{3-x} overlayer in the CO_2 hydrogenation process; (d) catalyst fabrication processes with *in situ* Ni decoration under Pt nanoparticles on perovskite $La_{0.52}Ca_{0.28}Ni_{0.06}Ti_{0.94}O_3$ nanofibres; (e) SEM micrograph of corresponding catalysts with $La_{0.52}Ca_{0.28}Ni_{0.06}Ti_{0.94}O_3$ nanofibres; (f) comparison of catalytic performance between $PtPdCu/Al_2O_3$ catalysts with controlled SMSI through different thermal treatments; (g) the influence of introduced Ba sites on the Ni/TiO_2-A catalyst through controlled SMSI and hydrodeoxygenation pathways [panel (a) has been reproduced with permission from ref. 85, Copyright 2020, American Chemical Society. Panel (b) has been reproduced with permission from ref. 229, Copyright 2024, American Chemical Society. Panel (c) has been reproduced with permission from ref. 215, Copyright 2022, American Chemical Society. Panels (d and e) have been reproduced with permission from ref. 230, Copyright 2022, Springer Nature. Panel (f) has been reproduced with permission from ref. 214, Copyright 2021, American Chemical Society. Panel (g) has been reproduced with permission from ref. 211, Copyright 2024, American Chemical Society].

offering catalyst reusability. Another strategy is to alloy the metal sites *in situ* with a reduction process to stabilize the active sites and enhance the catalytic performance.[230,231] Xu *et al.* presented an *in situ* approach to disperse Ni-decorated Pt nanoparticles on perovskite $La_{0.52}Ca_{0.28}Ni_{0.06}Ti_{0.94}O_3$ nanofibers (Fig. 19(d)).[230] In a typical fabrication process, Ni particles with diameters of ~50 nm were exsolved onto the surface of the nanofibrous through reduction, then the Pt precursor was added and fixed after the calcination step. The prepared sample was subsequently reduced at high temperature to trigger the formation of Pd–Ni bimetallic alloy nanoparticles. As shown in Fig. 19(e), the combination process of Ni and Pt species induced the nanoparticles to yield smaller sizes.

It is worth noting that a large part of the research on SMSI involving bimetallic systems is now applied to various catalytic oxidation processes instead of

hydrogenation.[210,230,233,234] One reasonable explanation is that the reducible support may be further promoted to cover the metal sites during the hydrogenation process, thus affecting the catalytic performance.[211] On the other hand, during the reduction process, the interaction between bimetallic sites and the reducible support may cause migration or segregation of active species in the bimetallic system.[232,235,236] In some cases, this phenomenon may promote catalytic performance, but it also complicates the characterization of the prepared sample and the explanation of the improved activities. However, limited research shows that it would be valuable to further investigate hydrogenation catalysis over bi(multi)metallic systems with SMSI.[211,214,231] Lu *et al.* innovatively regulated the covering behavior of Al_2O_3 to the supported trimetallic Pt–Pd–Cu nanoparticles under different low-temperature annealing conditions.[214] A stable Pt–Pd–Cu nanoparticle suspension was first obtained by a two-step synthesis, including a colloidal method step and a ligand exchange step. The nanoparticles were then deposited onto Al_2O_3 and annealed under different conditions, followed by reduction under H_2 to obtain the prepared sample. With the premise of removing ligand impurities on the catalyst, annealing at an appropriate temperature provides controllable SMSI without preventing changes in the size and morphology of active components. As shown in Fig. 19(f), during the annealing step, Al_2O_3 underwent a secondary growth that induced SMSI between Al_2O_3 and Pt–Pd–Cu nanoparticles, which offered a balance between partial coverage and optimal catalytic activity for hydrogenation under annealing conditions with 185 °C. Furthermore, Fang *et al.* recently reported the suppressing effect of alkaline earth metal elements as modifiers on SMSI around Ni nanoparticles in a supported bimetallic system.[211] As shown in Fig. 19(g), with the presence of Ba ions, the cross-migration phenomenon caused by the SMSI effect between Ni and anatase TiO_2 (TiO_2-A) was effectively suppressed, which tuned the reduced TiO_2 overlayer from full coverage to partial coverage. In addition, Ba modified the surface acidity of anatase TiO_2, thereby doubling the yield of cyclohexane/cyclohexanol by promoting the selectivity in the guaiacol hydrodeoxygenation reaction.

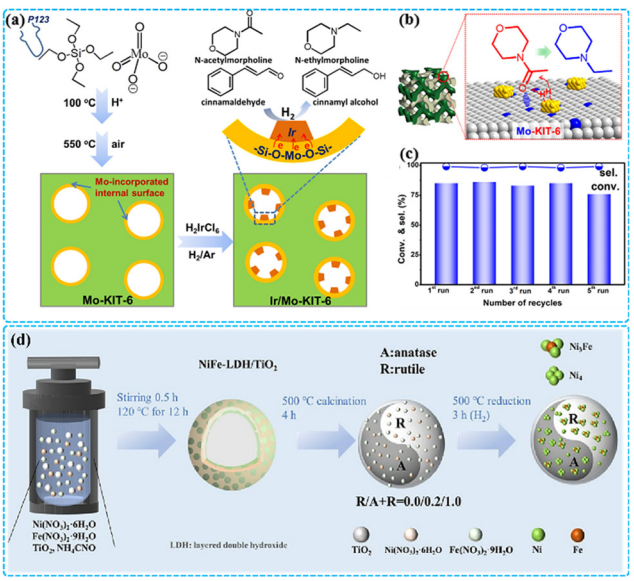

Fig. 20 (a) Schematic illustration for fabricating Ir/Mo–KIT-6 with EMSI to boost catalytic hydrogenation; (b) proposed mechanism of *N*-acetylmorpholine hydrogenation on Ir/Mo–KIT-6; (c) stability test of Ir/Mo–KIT-6 for five successive runs; (d) schematic diagram of the synthesis process over Ni_3Fe/TiO_2 (anatase and rutile) catalysts [panels (a–c) have been reproduced with permission from ref. 221, Copyright 2018, American Chemical Society. Panel (d) has been reproduced with permission from ref. 217, Copyright 2023, Elsevier].

3.3.2 Electronic metal–support interaction (EMSI). Considering the complex electron transfer behavior in the general hydrogenation process, it is worth discussing the electronic metal–support interaction (EMSI) as it emphasizes the chemical bonding and associated charge transfer at the interface between the loaded metallic sites and support, which can change the electronic properties of the active sites for a tunable catalysis performance.[210] The occurrence of charge transfer behavior depends on the difference in Fermi levels between the metal sites and support, thus, the direction of charge transfer can be either from the metal sites to the support or in the opposite direction.[91,221] Simultaneously, for the loaded metal sites on the nanoscale or atomic scale, the behavior of the charge transfer is strongly related to the coordination environment of the sites.[210] Chen *et al.* fabricated EMSI by uniformly incorporating molybdenum into mesoporous silica (KIT-6) to achieve strong interaction with loaded Ir sites.[221] As shown in Fig. 20(a), through the co-assembly procedure, Mo was first introduced to activate the interface of KIT-6 followed by loading Ir nanoparticles to form Ir–O–Mo coordination, which can promote the electron transfer from the modified support to Ir sites. The EMSI caused by the Ir–O–Mo configuration not only stabilizes the ultrafine Ir particles but also lets Mo sites and Ir sites work synergistically to promote the catalytic hydrogenation of *N*-acetylmorpholine (Fig. 20(b)). This proposed mechanism was demonstrated by the stability test on conversion and selectivity shown in Fig. 20(c). Also, the size of the metal sites is another important factor to be taken into account regarding constructing EMSI. In Guo's research, the EMSI behavior of CeO_2-supported Ru single atoms, nanoclusters, and nanoparticles was investigated, and the EMSI related to the electronic interaction of charge transfer *via* Ru–O–Ce was found to become more enhanced as the size of Ru decreased from nanoparticles to single atoms.[237]

From the aspect of supports, reducible TiO_2 attracted the most attention in EMSI-related research because of the extensive strategies of modification on surface defects and crystal facets of TiO_2 as a mature semiconductor that offers adjustable energy states for electronic interactions with supported metal sites.[238,239] Furthermore, the crystal phase of TiO_2 was also reported to influence the formation of EMSI. In comparison, with the one-pot hydrothermal and thermal

post-treatment process shown in Fig. 20(d), Ni_3Fe nanoparticles were loaded on rutile and anatase TiO_2, respectively.[217] Benefiting from the existing surface oxygen vacancies (OVs) on rutile TiO_2, the NiFe-LDH precursor prefers to form Ni_3Fe bimetallic sites rather than Ni_4 during thermal treatment, which further promotes the formation of OVs on the TiO_2 surface. Then, in the hydrogenation reaction of fatty acids for obtaining fatty alcohol products, the EMSI formed between Ni_3Fe and OVs endows the catalyst with bifunctional characteristics, where Ni_3Fe promotes H–H bond dissociation while the OV sites are responsible for absorbing the acid molecule and breaking the C=O bond. However, it should be noted that strong EMSI doesn't always play a positive role in specific catalyst systems or hydrogenation reactions, which has been demonstrated by the research that focused on comparing the EMSI-driven catalytic properties with different supports.[240,241] By contrast, although conventional inert supports (*e.g.*, SiO_2 and Al_2O_3) are typically considered to form only weak EMSI with metallic sites,[207,220] they can still achieve outstanding catalytic performance in certain hydrogenation reactions.[218,240] For instance, a recent study by Yang *et al.* demonstrated that sub-nanometer Ni–Ru bimetallic sites, loaded onto SiO_2 *via* the SEA method, exhibited high conversion in the selective hydrogenation of biphenyl to cyclohexylbenzene.[91] This performance was attributed to the charge transfer from metallic Ni to SiO_2, which rendered the Ni sites electron-deficient, thereby enhancing the adsorption and activation of electron-withdrawing aromatic groups during the reaction.

3.3.3 Structured supports. In the previous chapters, we have discussed various strategies for improving the dispersion of nanoparticles and immobilization of metallic active sites in bimetallic-support systems such as diluted-alloy, SEA, single/diatomic catalysts, metal–support interaction, *etc.* Most of the strategies are commonly based on the idea of loading active species onto the support surface by impregnation, deposition, or immobilization procedures. While convenient, supports used in those methods do not play well in affording the ability to control collective ensembles like nanoparticle properties, such as proximity, placement, and compartmentalization.[242] To overcome this, the fabrication of structured support is considered an effective way. For example, Li *et al.* succeeded in compartmentalizing Pt single-atom sites by confining them to highly structured CeO_2 nanoglue islands anchored on robust high-surface-area SiO_2.[243] They pointed out that the migration of Pt sites under reaction conditions can only be confined in the range of the CeO_2 islands since the interaction between Pt and CeO_2 is higher than that between Pt and SiO_2, which greatly enhances the catalytic stability of single-atom catalysts in high-temperature reducing atmospheres. This section will briefly introduce the recent research on fabricating structured supports and related bimetallic systems.

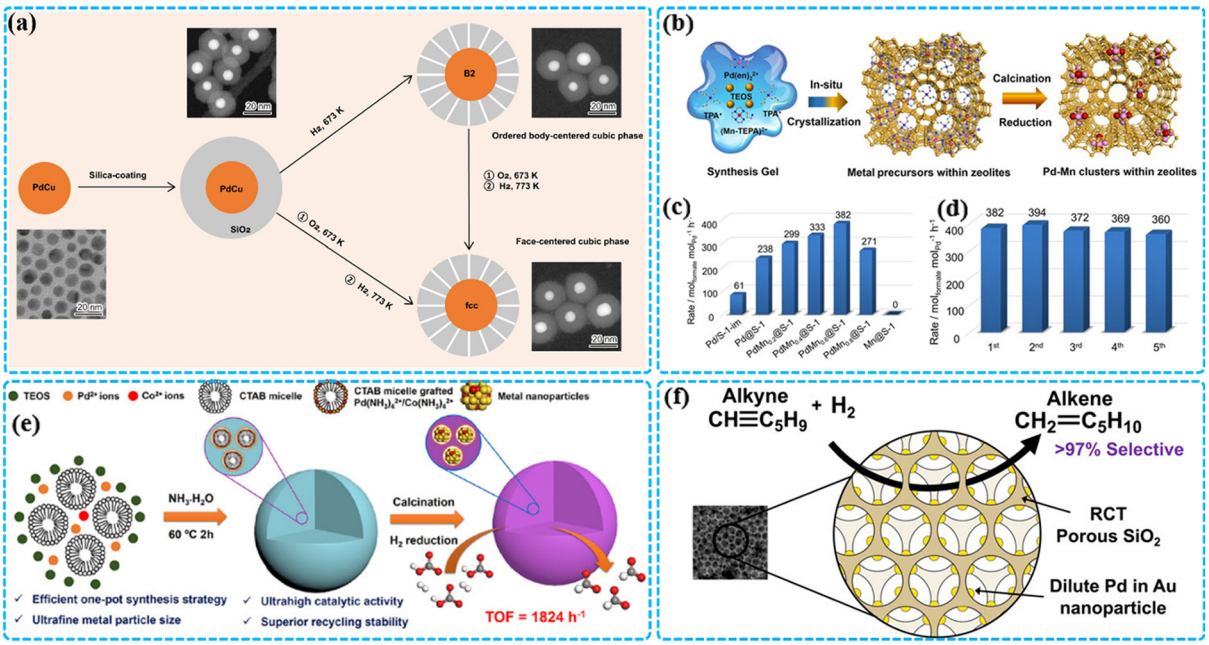

Fig. 21 (a) Tuning the crystal-phase of the PdCu catalysts at the single-nanoparticle scale covered by porous SiO_2; (b) schematic of the synthetic procedure of bimetallic $PdMn_x$@silicalite-1 (S-1) zeolite catalysts; (c) comparison of the formate generation rates from the CO_2 hydrogenation over various catalysts; (d) recycling stability tests of the $PdMn_{0.6}$@S-1 catalyst for CO_2 hydrogenation; (e) schematic illustration of the preparation of Pd_xCo_{1-x}@mesoporous silica nanosphere (MSN) catalysts; (f) schematic illustration of diluted Pd in Au NPs supported on RCT porous SiO_2 [panel (a) has been reproduced with permission from ref. 245, Copyright 2022, Springer Nature. Panels (b–d) have been reproduced with permission from ref. 226, Copyright 2020, WILEY. Panel (e) has been reproduced with permission from ref. 223, Copyright 2019, European Chemical Societies Publishing. Panel (f) has been reproduced with permission from ref. 224, Copyright 2020, American Chemical Society].

For structured supports, the most intuitive role is their ability to spatially separate metal active sites. As discussed in section 3.1.1, the significance of the 3D self-pillared zeolite nanosheet structure lies in its role in forming sub-nanometer Rh–Ru bimetallic particles. In a recent study by Zhang *et al.*, 3D flower-shaped Al_2O_3 was employed as a support for sintering-resistant Pd–Sn bimetallic catalysts.[244] The excellent spatial separation ability not only resulted in smaller supported Pd–Sn particles during the preparation but also significantly enhanced stability in catalytic reactions. Furthermore, as shown in Fig. 21(a), Liu *et al.* used a reverse microemulsion method to coat monodisperse Pd–Cu colloidal particles with a silica shell, which was then converted into permeable porous silica through post-thermal treatment.[245] This reverse-loaded porous silica encapsulation maintained catalytic activity for hydrogenation reactions while spatially confining the metal particles and thus retained its original particle size. More interestingly, the monodisperse silica-covered Pd–Cu particles could undergo a crystal phase transition under specific conditions, which offers new insights into precisely controlling single-nanoparticles and interpreting the atomic configuration of active sites on the particle surface.

Another crucial aspect of structured supports is the construction of supports with highly ordered porous structures or channel-based frameworks, such as porous silica,[223,224] zeolites,[226,246,247] metal–organic frameworks (MOFs) and their derivatives.[225,248] A tunable porous structure not only offers numerous loading and reaction sites due to its high surface area but also significantly influences metal dispersion and compartmentalization, enhances mass transfer efficiency during catalytic reactions, and enables the selective confinement of intermediates. Currently, the primary strategy for synthesizing metal-loaded porous materials is known as the one-pot crystallization process, where metal species are homogeneously dispersed within the precursor of the support, followed by post-thermal treatment to obtain catalysts with nanoparticles encapsulated within the pores.[226,249] To enhance metal dispersion and control particle size, a common approach involves applying specific ligands or surfactants during crystallization, a strategy referred to as the ligand-protected method.[223,250] As shown in Fig. 21(b), Sun *et al.* successfully embedded sub-nanometer Pd–Mn clusters *in situ* in silica-1 zeolites using the ligand-protected method.[226] Fig. 21(c) illustrates the high reaction rate of Pd–Mn bimetallic catalysts for CO_2 hydrogenation to formates under an optimized Pd : Mn ratio. This enhancement is due to the formation of sub-nanometer clusters, facilitated by the ordered microporous framework and the synergistic interaction between Pd and Mn. Additionally, the structured zeolites effectively prevent the aggregation of small clusters containing non-precious metal species, thereby improving the thermal stability of the bimetallic active sites (Fig. 21(d)). Using the same approach, Sun and colleagues synthesized mesoporous silica-encaged ultrafine Pd–CoO bimetallic nanocatalysts.[223] As shown in Fig. 21(e), CTAB micelles served as grafting sites during the crystallization process to control the dispersion of the Pd and Co precursors, yielding ~1.8 nm Pd–CoO nanoparticles after post-thermal treatment. This simple and systematic approach resulted in highly active and durable catalysts for CO_2 hydrogenation to formates. Besides, the colloidal template method is also a strategy to offer greater isolated control over individual components or metal–support assemblies. The colloidal template method can be used to either overgrow a secondary coating around a single colloidal particle or to infiltrate a close-packed arrangement of self-assembled colloidal crystals.[242] After template removal, the former routine tends to generate shell-structured supports, while the latter tends to form highly-ordered porous supports. Among them, the raspberry colloidal templating (RCT) method partially embeds nanoparticles within the macroporous support, ensuring high thermal and mechanical stability while maintaining the accessibility of active sites for reactants. In a typical study shown in Fig. 21(f), ultrafine Pd–Au bimetallic particles were embedded into an RCT macroporous silica support using the above method.[224] The composite colloidal template was first prepared by mixing pre-synthesized bimetallic nanoparticles and thiol-modified polystyrene colloidal microspheres, followed by infiltration with a silica precursor to backfill the interstitial spaces. The RCT silica-encapsulated Pd–Au system was formed by subsequent calcination to remove the template. The highly ordered macroporous structure facilitated the mass transfer of reactants, intermediates, and products, thereby enhancing the sintering-resistance ability of catalysts.

It is worth noting that the metal–support interaction not only depends on the various synthesis strategies but is also affected by the actual reactive environment. In addition to physical parameters such as temperature and pressure, the dynamic changes of metal–support interaction are also affected by the reactive gases or intermediates that are adsorbed on the active sites in a specific reaction.[210] The adsorption behavior can change the surface energy of the metallic sites and tends to affect the contact area of the active sites, then further inducing the dynamic evolution of the metal–support interface.[207] Thanks to the development of *in situ* characterization technology, the dynamic change has been generally proven to exist at the perimeter interface between NPs and certain reducible supports,[251–253] which will provide guidance for the rational design of future supported bimetallic catalysts in the future.

4. Summary and outlook

Hydrogenation reactions, which are central to the production of high-value industrial materials, represent one of the most critical processes in industrial catalysis. Given the stringent requirements for high conversion efficiency, high selectivity, and commercial feasibility, bimetallic catalysts have demonstrated superior application potential compared to traditional monometallic catalysts, owing to their unique

geometric effects, electronic effects, and synergistic effects. To fully exploit these advantages, the selection of an appropriate synthesis strategy to construct bimetallic systems with diverse structures and compositions is crucial. As reviewed, significant progress has been made in this field, but several major challenges remain:

(1) Size control remains a perpetual challenge for supported catalysts. For multiple hydrogenation reactions, smaller active metal sites and higher dispersion typically lead to the promotion of the above effects and improve catalytic efficiency, and the current precise synthesis strategy on a laboratory scale is already well established and proven. However, as we mentioned at the end of section 3.3, nano-scale metal particles tend to sinter, aggregate, or reconstruct under real reaction conditions, followed by deactivation. Thus, for synthesizing well-designed bimetallic catalysts in the future, it is essential to take the reconstruction behaviour of bimetallic particles under actual reaction conditions into account—an aspect that must be evaluated with the aid of the rapid development of *in situ* characterization techniques.

(2) Compared with supported heterogeneous catalysts, SACs exhibit advantages of their maximized atomic utilization and homogeneous active sites with adjustable electronic environments. However, the requirement for precise synthesis conditions significantly limits their scalability, confining most studies to the laboratory without clear potential for large-scale production and commercial applications. For hydrogenation reactions, taking the single-atom alloys as an example, most studies aimed at achieving atomic-level dispersion of active components by sacrificing the loading of active metal species. In some cases, the improved catalytic performance is still limited even when maximized utilization of active components is achieved, which cannot meet practical applications. Therefore, it is an existing challenge to balance the loading of active atoms and their aggregation behaviour to prepare high-loading SACs. In addition, for specific hydrogenation reaction processes, such as multi-step hydrogenation, it has been reported that the catalytic performance of regular SACs is not superior to heterogeneous catalysts due to the aspects of dissociation mode of hydrogen, multi-step activation of reactants, and competitive adsorption of dissociated hydrogen and reactive intermediates. In this case, designing SACs with bifunctional effects should be considered as another valuable choice. Therefore, for the rational design of bimetallic SACs, it is necessary to take the type of hydrogenation reaction and actual reaction conditions into consideration.

(3) For various bimetallic catalysts reported so far, standardization of reaction or evaluation conditions (such as temperature, pressure, flow rate of reactive gases, *etc.*) will be able to provide uniform performance evaluation criteria for designing catalysts more rationally. Taking the selective hydrogenation of acetylene as an example, the reported stream of time for catalyst stability tests varies from tens to hundreds of hours. However, the space velocity of reactants varies greatly across studies, typically from thousands to tens of thousands of h^{-1}. Such discrepancies may cast doubt on the actual stability of the catalysts and hinder meaningful horizontal comparisons among catalysts. From a practical view, it is obviously unrealistic to validate the performance of different catalysts experimentally. With the rapid development of artificial intelligence and advanced algorithms, theoretical predictions based on the vast amount of existing research data can be provided to support the screening of optimal bimetallic combinations for a given hydrogenation reaction.

(4) Although this review primarily focuses on the synthesis strategies of bimetallic catalysts, this does not imply that the study of catalytic mechanisms for specific hydrogenation reactions is unimportant. To date, most research has been dedicated to developing novel catalysts for better catalytic performances, while insufficient attention has been given to the fundamental study of hydrogenation reaction mechanisms. Therefore, guidance for the rational design of catalysts should originate from further exploration of the relationships among activation energy barriers, adsorption/desorption energies, and undesirable side reactions. In this regard, valuable insights and significant support can be offered by advancements in theoretical calculations and *in situ* characterization techniques.

Author contributions

A. Z. reviewed the literature and drafted the manuscript. K. Y. and A. P. contributed to this work by performing formal analysis, editing, and providing suggestions. W. D. contributed by supervision, validation, project administration, and revising (review and editing).

Conflicts of interest

There are no conflicts to declare.

Data availability

As a review manuscript, no new data were created or analyzed in this study. Data sharing does not apply to this article. All data in this manuscript are from cited references, with permission for reproduction from the publisher.

Acknowledgements

The authors would like to thank the Department of Chemical and Biological Engineering, College of Engineering at Villanova University, for financial support.

References

1 G. A. Olah, A. Goeppert and G. K. S. Prakash, *J. Org. Chem.*, 2009, **74**, 487–498.
2 W. Wang, S. Wang, X. Ma and J. Gong, *Chem. Soc. Rev.*, 2011, **40**, 3703–3727.

3 M. Taniewski, *Clean:Soil, Air, Water*, 2008, **36**, 393–398.
4 S. Anand, D. Pinheiro and K. R. Sunaja Devi, *Asian J. Org. Chem.*, 2021, **10**, 3068–3100.
5 S. Mao, Z. Wang, Q. Luo, B. Lu and Y. Wang, *ACS Catal.*, 2022, **13**, 974–1019.
6 P. Munnik, P. E. de Jongh and K. P. de Jong, *Chem. Rev.*, 2015, **115**, 6687–6718.
7 Y. Chen, M. J. Kuo, R. Lobo and M. Ierapetritou, *Green Chem.*, 2024, **26**, 2903–2911.
8 J. Guo, Y. Lei, H. Liu, Y. Li, D. Li and D. He, *Catal. Sci. Technol.*, 2023, **13**, 4045–4063.
9 J. A. Delgado, O. Benkirane, C. Claver, D. Curulla-Ferre and C. Godard, *Dalton Trans.*, 2017, **46**, 12381–12403.
10 J.-F. Portha, K. Parkhomenko, K. Kobl, A.-C. Roger, S. Arab, J.-M. Commenge and L. Falk, *Ind. Eng. Chem. Res.*, 2017, **56**, 13133–13145.
11 L. Samiee and E. GhasemiKafrudi, *React. Kinet., Mech. Catal.*, 2021, **133**, 801–823.
12 W. Zhang, J. Sun, H. Wang and X. Cui, *Chem. – Asian J.*, 2024, **19**, e202300971.
13 K. P. Reddy, D. Kim, S. Hong, K. J. Kim, R. Ryoo and J. Y. Park, *ACS Appl. Mater. Interfaces*, 2023, **15**, 9373–9381.
14 M. Mikkelsen, M. Jørgensen and F. C. Krebs, *Energy Environ. Sci.*, 2010, **3**, 43–81.
15 S. Kattel, P. Liu and J. G. Chen, *J. Am. Chem. Soc.*, 2017, **139**, 9739–9754.
16 D. Gómez, C. Candia, R. Jiménez and A. Karelovic, *J. Catal.*, 2022, **406**, 96–106.
17 A. Wong, Q. Liu, S. Griffin, A. Nicholls and J. R. Regalbuto, *Science*, 2017, **358**, 1427–1430.
18 W. Diao, J. M. M. Tengco, A. M. Gaffney, J. R. Regalbuto and J. R. Monnier, in *Catalysis*, ed. J. Spivey, Y.-F. Han and D. Shekhawat, The Royal Society of Chemistry, 2020, vol. 32.
19 F. Xue, Q. Li, M. Lv, Y. Song, T. Yang, X. Wang, T. Li, Y. Ren, K. Ohara, Y. He, D. Li, Q. Li, X. Chen, K. Lin and X. Xing, *J. Am. Chem. Soc.*, 2023, **145**, 26728–26735.
20 Z. Luo, G. Zhao, H. Pan and W. Sun, *Adv. Energy Mater.*, 2022, **12**, 2201395.
21 A. K. Singh and Q. Xu, *ChemCatChem*, 2013, **5**, 652–676.
22 J. Fan, H. Du, Y. Zhao, Q. Wang, Y. Liu, D. Li and J. Feng, *ACS Catal.*, 2020, **10**, 13560–13583.
23 X. Liu, D. Wang and Y. Li, *Nano Today*, 2012, **7**, 448–466.
24 B. Lim, M. Jiang, P. H. C. Camargo, E. C. Cho, J. Tao, X. Lu, Y. Zhu and Y. Xia, *Science*, 2009, **324**, 1302–1305.
25 W. U. Khan, L. Baharudin, J. Choi and A. C. K. Yip, *ChemCatChem*, 2020, **13**, 111–120.
26 L. Liu and A. Corma, *Chem. Rev.*, 2023, **123**, 4855–4933.
27 H. Zhou, X. Yang, L. Li, X. Liu, Y. Huang, X. Pan, A. Wang, J. Li and T. Zhang, *ACS Catal.*, 2016, **6**, 1054–1061.
28 T. D. Shittu and O. B. Ayodele, *Front. Chem. Sci. Eng.*, 2022, **16**, 1031–1059.
29 A. M. Robinson, J. E. Hensley and J. W. Medlin, *ACS Catal.*, 2016, **6**, 5026–5043.
30 S. Ashraf, Y. Liu, H. Wei, R. Shen, H. Zhang, X. Wu, S. Mehdi, T. Liu and B. Li, *Small*, 2023, **19**, e2303031.
31 T. Li, N. Ji, Z. Jia, X. Diao, Z. Wang, Q. Liu, C. Song and X. Lu, *ChemCatChem*, 2020, **12**, 5288–5302.
32 B. Yang, R. Burch, C. Hardacre, P. Hu and P. Hughes, *J. Phys. Chem. C*, 2014, **118**, 1560–1567.
33 J. Wood, M. J. Alldrick, J. M. Winterbottom, E. H. Stitt and S. Bailey, *Catal. Today*, 2007, **128**, 52–62.
34 Y. Zhang, W. Diao, C. T. Williams and J. R. Monnier, *Appl. Catal., A*, 2014, **469**, 419–426.
35 G. X. Pei, X. Y. Liu, X. Yang, L. Zhang, A. Wang, L. Li, H. Wang, X. Wang and T. Zhang, *ACS Catal.*, 2017, **7**, 1491–1500.
36 Z. Li, J. Zhang, J. Tian, K. Feng, Z. Jiang and B. Yan, *Chem. Eng. J.*, 2022, **450**, 138244.
37 F. Huang, M. Peng, Y. Chen, X. Cai, X. Qin, N. Wang, D. Xiao, L. Jin, G. Wang, X. D. Wen, H. Liu and D. Ma, *J. Am. Chem. Soc.*, 2022, **144**, 18485–18493.
38 A. Dasgupta, H. He, R. Gong, S. L. Shang, E. K. Zimmerer, R. J. Meyer, Z. K. Liu, M. J. Janik and R. M. Rioux, *Nat. Chem.*, 2022, **14**, 523–529.
39 X. Chen, C. Shi, X. B. Wang, W. Y. Li and C. Liang, *Commun. Chem.*, 2021, **4**, 175.
40 X. Wang, X. Liang, P. Geng and Q. Li, *ACS Catal.*, 2020, **10**, 2395–2412.
41 A. Han, J. Zhang, W. Sun, W. Chen, S. Zhang, Y. Han, Q. Feng, L. Zheng, L. Gu, C. Chen, Q. Peng, D. Wang and Y. Li, *Nat. Commun.*, 2019, **10**, 3787.
42 L. Wang, B. Wang, M. Fan, L. Ling and R. Zhang, *Fuel*, 2022, **321**, 124118.
43 F. Liu, Y. Xia, W. Xu, L. Cao, Q. Guan, Q. Gu, B. Yang and J. Lu, *Angew. Chem., Int. Ed.*, 2021, **60**, 19324–19330.
44 X. Wang, M. Chu, M. Wang, Q. Zhong, J. Chen, Z. Wang, M. Cao, H. Yang, T. Cheng, J. Chen, T. K. Sham and Q. Zhang, *ACS Nano*, 2022, **16**, 16869–16879.
45 D. Kim, J. Resasco, Y. Yu, A. M. Asiri and P. Yang, *Nat. Commun.*, 2014, **5**, 4948.
46 Y. Liu, W. Guo, X. Li, P. Jiang, N. Zhang and M. Liang, *ACS Appl. Nano Mater.*, 2021, **4**, 5292–5300.
47 J. Rodriguez, *Prog. Surf. Sci.*, 2006, **81**, 141–189.
48 C. T. Campbell, *Annu. Rev. Phys. Chem.*, 1990, **41**, 775–837.
49 S. A. Khromova, A. A. Smirnov, O. A. Bulavchenko, A. A. Saraev, V. V. Kaichev, S. I. Reshetnikov and V. A. Yakovlev, *Appl. Catal., A*, 2014, **470**, 261–270.
50 L. T. Roling, L. Li and F. Abild-Pedersen, *J. Phys. Chem. C*, 2017, **121**, 23002–23010.
51 L. T. Roling, T. S. Choksi and F. Abild-Pedersen, *Nanoscale*, 2019, **11**, 4438–4452.
52 F. Yang, D. Liu, H. Wang, X. Liu, J. Han, Q. Ge and X. Zhu, *J. Catal.*, 2017, **349**, 84–97.
53 M. T. Greiner, T. E. Jones, S. Beeg, L. Zwiener, M. Scherzer, F. Girgsdies, S. Piccinin, M. Armbrüster, A. Knop-Gericke and R. Schlögl, *Nat. Chem.*, 2018, **10**, 1008–1015.
54 Y. He, L. Liang, Y. Liu, J. Feng, C. Ma and D. Li, *J. Catal.*, 2014, **309**, 166–173.

55 W. Xue, H. Liu, B. Zhao, L. Ge, S. Yang, M. Qiu, J. Li, W. Han and X. Chen, *Appl. Catal., B*, 2023, **327**, 122453.
56 C. Yao, D. Ma, J. Luo, Y. Chen, M. Tian, H. Xie, C. Lu, F. Feng, X. Xu, Q. Wang, Q. Zhang and X. Li, *Chin. J. Chem. Eng.*, 2023, **63**, 260–267.
57 S. Tada, H. Nagase, N. Fujiwara and R. Kikuchi, *Energy Fuels*, 2021, **35**, 5241–5251.
58 F. Studt, F. Abild-Pedersen, T. Bligaard, R. Z. Sørensen, C. H. Christensen and J. K. Nørskov, *Science*, 2008, **320**, 1320–1322.
59 L. Nie, P. M. de Souza, F. B. Noronha, W. An, T. Sooknoi and D. E. Resasco, *J. Mol. Catal. A: Chem.*, 2014, **388–389**, 47–55.
60 S. K. Singh, *Asian J. Org. Chem.*, 2018, **7**, 1901–1923.
61 Y. Xiao, Q. Meng, X. Pan, C. Zhang, Z. Fu and C. Li, *Green Chem.*, 2020, **22**, 4341–4349.
62 R. Yao, B. Wu, Y. Yu, N. Liu, Q. Niu, C. Li, J. Wei and Q. Ge, *Appl. Catal., B*, 2024, **355**, 124159.
63 D. Xu, M. Ding, X. Hong and G. Liu, *ACS Catal.*, 2020, **10**, 14516–14526.
64 A. Xiao, H. Xu, H. Cui, Z. Cheng and Z. Zhou, *Appl. Catal., A*, 2023, **666**, 119424.
65 Q. Han, M. U. Rehman, J. Wang, A. Rykov, O. Y. Gutiérrez, Y. Zhao, S. Wang, X. Ma and J. A. Lercher, *Appl. Catal., B*, 2019, **253**, 348–358.
66 S. Han, R. Gao, M.-S. Sun, Y. Zhou, W.-T. Chen, X. Liu, J. Qin, D.-J. Tao and Z. Zhang, *J. Phys. Chem. C*, 2023, **127**, 14185–14196.
67 F. Fu, Y. Liu, Y. Li, B. Fu, L. Zheng, J. Feng and D. Li, *ACS Catal.*, 2021, **11**, 11117–11128.
68 J. L. Snider, V. Streibel, M. A. Hubert, T. S. Choksi, E. Valle, D. C. Upham, J. Schumann, M. S. Duyar, A. Gallo, F. Abild-Pedersen and T. F. Jaramillo, *ACS Catal.*, 2019, **9**, 3399–3412.
69 J. Pinto, A. Weilhard, L. T. Norman, R. W. Lodge, D. M. Rogers, A. Gual, I. Cano, A. N. Khlobystov, P. Licence and J. Alves Fernandes, *Catal. Sci. Technol.*, 2023, **13**, 4082–4091.
70 A. Wang, X. Y. Liu, C.-Y. Mou and T. Zhang, *J. Catal.*, 2013, **308**, 258–271.
71 Q. Gao, Z. Yan, W. Zhang, H. S. Pillai, B. Yao, W. Zang, Y. Liu, X. Han, B. Min, H. Zhou, L. Ma, B. Anaclet, S. Zhang, H. Xin, Q. He and H. Zhu, *J. Am. Chem. Soc.*, 2023, **145**, 19961–19968.
72 T. Liu, Z. Tian, W. Zhang, B. Luo, L. Lei, C. Wang, J. Liu, R. Shu and Y. Chen, *Fuel*, 2023, **339**, 126916.
73 O. E. Brandt Corstius, H. L. Nolten, G. F. Tierney, Z. Xu, E. J. Doskocil, J. E. S. van der Hoeven and P. E. de Jongh, *Catal. Today*, 2024, **441**, 114877.
74 Q. Yang, R. Hou and K. Sun, *J. Catal.*, 2019, **374**, 12–23.
75 Z. Yang, J. Han, Q. Fan, H. Jia and F. Zhang, *Appl. Catal., A*, 2018, **568**, 183–190.
76 Y. Liu, K. Liu, M. Zhang, K. Zhang, J. Ma, S. Xiao, Z. Wei and S. Deng, *RSC Adv.*, 2021, **12**, 602–610.
77 Z. Gao, G. Fan, M. Liu, L. Yang and F. Li, *Appl. Catal., B*, 2018, **237**, 649–659.
78 J. D. Lee, C. Wang, T. Jin, R. J. Gorte and C. B. Murray, *Appl. Catal., A*, 2020, **606**, 117808.
79 H. Wang, X. Li, X. Lan and T. Wang, *ACS Catal.*, 2018, **8**, 2121–2128.
80 G. Xie, X. Bai, F. Yu, Q. Yang and Z.-j. Wang, *Catal. Today*, 2024, **434**, 114702.
81 M. J. Taylor, S. K. Beaumont, M. J. Islam, S. Tsatsos, C. A. M. Parlett, M. A. Issacs and G. Kyriakou, *Appl. Catal., B*, 2021, **284**, 119737.
82 H. Wang, S. Bai, Y. Pi, Q. Shao, Y. Tan and X. Huang, *ACS Catal.*, 2018, **9**, 154–159.
83 S. D. Le and S. Nishimura, *ACS Sustainable Chem. Eng.*, 2019, **7**, 18483–18492.
84 D. Shi, Q. Yang, C. Peterson, A.-F. Lamic-Humblot, J.-S. Girardon, A. Griboval-Constant, L. Stievano, M. T. Sougrati, V. Briois, P. A. J. Bagot, R. Wojcieszak, S. Paul and E. Marceau, *Catal. Today*, 2019, **334**, 162–172.
85 C. Hernandez Mejia, J. E. S. van der Hoeven, P. E. de Jongh and K. P. de Jong, *ACS Catal.*, 2020, **10**, 7343–7354.
86 G. Bharath, K. Rambabu, A. Hai, F. Banat, S. Rajendran, D. D. Dionysiou and P. Loke Show, *Fuel*, 2021, **290**, 119826.
87 J. E. Bruno, N. S. Dwarica, T. N. Whittaker, E. R. Hand, C. S. Guzman, A. Dasgupta, Z. Chen, R. M. Rioux and B. D. Chandler, *ACS Catal.*, 2020, **10**, 2565–2580.
88 Z. Wei, Q. Li, Y. Cheng, M. Dong, Z. Zhang, X. Zhu, Y. Liu and Y. Sun, *ACS Sustainable Chem. Eng.*, 2021, **9**, 10882–10891.
89 L. Wang, P. Yin, L.-L. Zhang, S.-C. Shen, S.-L. Xu, P. Chen and H.-W. Liang, *J. Catal.*, 2020, **389**, 297–304.
90 F. Han, J. Xia, X. Zhang and Y. Fu, *RSC Adv.*, 2019, **9**, 17812–17823.
91 J. Yang, Y. Gao, J. Fan, J. Wang, T. Yang, Z. Bing, M. Zhang and Z. Liu, *Appl. Surf. Sci.*, 2024, **660**, 159959.
92 W.-H. Wang, B. Jiang, Z. Wang, Y. Chen, Y. Li, T.-T. Luo, F. Cheng and B.-L. Su, *Mol. Catal.*, 2023, **550**, 113602.
93 K. Zhou, J. Chen, Y. Cheng, Z. Chen, S. Kang, Z. Cai, Y. Xu and J. Wei, *ACS Sustainable Chem. Eng.*, 2020, **8**, 16624–16636.
94 J. M. Keels, X. Chen, S. Karakalos, C. Liang, J. R. Monnier and J. R. Regalbuto, *ACS Catal.*, 2018, **8**, 6486–6494.
95 B. A. T. Mehrabadi, S. Eskandari, U. Khan, R. D. White and J. R. Regalbuto, *Chapter One - A Review of Preparation Methods for Supported Metal Catalysts*, ed. C. Song, Elsevier, Amsterdam, 2017, vol. 61, pp. 1–35.
96 H. Wang and J. Lu, *Chin. J. Chem.*, 2020, **38**, 1422–1444.
97 F. Jiang, J. Cai, B. Liu, Y. Xu and X. Liu, *RSC Adv.*, 2016, **6**, 75541–75551.
98 J. K. Nørskov, T. Bligaard, B. Hvolbæk, F. Abild-Pedersen, I. Chorkendorff and C. H. Christensen, *Chem. Soc. Rev.*, 2008, **37**, 2163–2171.
99 C. N. R. Rao, G. U. Kulkarni, P. J. Thomas and P. P. Edwards, *Chem. – Eur. J.*, 2002, **8**, 28–35.
100 Y. Sunagawa, K. Yamamoto, H. Takahashi and A. Muramatsu, *Catal. Today*, 2008, **132**, 81–87.
101 S. Agnihotri, S. Mukherji and S. Mukherji, *RSC Adv.*, 2014, **4**, 3974–3983.
102 X. Cao, B. W. Jang, J. Hu, L. Wang and S. Zhang, *Molecules*, 2023, **28**, 2572.

103 B. A. Yusuf, W. Yaseen, J. Xie, A. A. Babangida, A. I. Muhammad, M. Xie and Y. Xu, *Nano Energy*, 2022, **104**, 107959.
104 Q. Qin and D. Ramkrishna, *Ind. Eng. Chem. Res.*, 2005, **44**, 6466–6476.
105 J. R. Regalbuto, *Catalyst Preparation: Science and Engineering*, Taylor & Francis Group, 2006.
106 X. Cao, T. Lyu, W. Xie, A. Mirjalili, A. Bradicich, R. Huitema, B. W. L. Jang, J. K. Keum, K. More, C. Liu and X. Yan, *Front. Chem. Sci. Eng.*, 2019, **14**, 522–533.
107 A. K. Sharma, P. Mehara and P. Das, *ACS Catal.*, 2022, **12**, 6672–6701.
108 D. V. Yurpalova, T. N. Afonasenko, I. P. Prosvirin, A. V. Bukhtiyarov, M. A. Panafidin, Z. S. Vinokurov, M. V. Trenikhin, E. Y. Gerasimov, T. I. Gulyaeva, L. M. Kovtunova and D. A. Shlyapin, *Catalysts*, 2023, **13**, 739.
109 T. Vergunst, F. Kapteijn and J. A. Moulijn, *Appl. Catal., A*, 2001, **213**, 179–187.
110 A. Quindimil, M. C. Bacariza, J. A. González-Marcos, C. Henriques and J. R. González-Velasco, *Appl. Catal., B*, 2021, **296**, 120322.
111 N. Wang, Q. Sun, T. Zhang, A. Mayoral, L. Li, X. Zhou, J. Xu, P. Zhang and J. Yu, *J. Am. Chem. Soc.*, 2021, **143**, 6905–6914.
112 X. Gu, Z. H. Lu, H. L. Jiang, T. Akita and Q. Xu, *J. Am. Chem. Soc.*, 2011, **133**, 11822–11825.
113 Y. Ren, Y. Yang and M. Wei, *ACS Catal.*, 2023, **13**, 8902–8924.
114 C. J. Zhong and J. R. Regalbuto, in *Comprehensive Inorganic Chemistry II*, 2013, pp. 75–102, DOI: **10.1016/b978-0-08-097774-4.00711-7**.
115 A. Chrouda, S. Mahmoud Ali Ahmed and M. Babiker Elamin, *ChemBioEng Rev.*, 2022, **9**, 248–264.
116 D. L. Nguyen, S. Umbarkar, M. K. Dongare, C. Lancelot, J. S. Girardon, C. Dujardin and P. Granger, *Catal. Commun.*, 2012, **26**, 225–230.
117 R. Zanella, C. Louis, S. Giorgio and R. Touroude, *J. Catal.*, 2004, **223**, 328–339.
118 S. Zhao, H. Yue, Y. Zhao, B. Wang, Y. Geng, J. Lv, S. Wang, J. Gong and X. Ma, *J. Catal.*, 2013, **297**, 142–150.
119 Y. Zhao, S. Li, Y. Wang, B. Shan, J. Zhang, S. Wang and X. Ma, *Chem. Eng. J.*, 2017, **313**, 759–768.
120 L. A. Calzada, C. Louis, C. Wan Han, V. Ortalan and R. Zanella, *Appl. Catal., B*, 2020, **264**, 118503.
121 R. Zanella, S. Giorgio, C. R. Henry and C. Louis, *J. Phys. Chem. B*, 2002, **106**, 7634–7642.
122 L. A. M. Hermans and J. W. Geus, in *Studies in Surface Science and Catalysis*, ed. B. Delmon, P. Grange, P. Jacobs and G. Poncelet, Elsevier, 1979, vol. 3, pp. 113–130.
123 D. G. Araiza, C. A. Celaya, D. A. Solís-Casados, J. Muñiz and R. Zanella, *Chem. Eng. J.*, 2024, **494**, 152921.
124 A. Aguilar-Tapia, L. Delannoy, C. Louis, C. W. Han, V. Ortalan and R. Zanella, *J. Catal.*, 2016, **344**, 515–523.
125 Z. Wang, G. Wang, C. Louis and L. Delannoy, *Res. Chem. Intermed.*, 2021, **47**, 91–116.
126 M. Liu, S. Li, G. Fan, L. Yang and F. Li, *Ind. Eng. Chem. Res.*, 2019, **58**, 10317–10327.
127 M. S. Heise and J. A. Schwarz, *J. Colloid Interface Sci.*, 1986, **113**, 55–61.
128 W. A. Spieker and J. R. Regalbuto, *Chem. Eng. Sci.*, 2001, **56**, 3491–3504.
129 H.-R. Cho and J. R. Regalbuto, *Catal. Today*, 2015, **246**, 143–153.
130 K. Ding, D. A. Cullen, L. Zhang, Z. Cao, A. D. Roy, I. N. Ivanov and D. Cao, *Science*, 2018, **362**, 560–564.
131 J. M. Macasero Tengco, *Doctoral dissertation*, University of South Carolina, 2016.
132 J. Yang, Y. Fan, Z.-L. Li, Z. Peng, J.-H. Yang, B. Liu and Z. Liu, *Mol. Catal.*, 2020, **492**, 110992.
133 X. Niu, J. Sun, W. Zhao, X. Yang, X. Zhang and Q. Wang, *Fuel Process. Technol.*, 2023, **241**, 107622.
134 S. Riyapan, Y. Zhang, A. Wongkaew, B. Pongthawornsakun, J. R. Monnier and J. Panpranot, *Catal. Sci. Technol.*, 2016, **6**, 5608–5617.
135 C. Park, P. A. Fenter, N. C. Sturchio and J. R. Regalbuto, *Phys. Rev. Lett.*, 2005, **94**, 076104.
136 N. Job, S. Lambert, M. Chatenet, C. J. Gommes, F. Maillard, S. Berthon-Fabry, J. R. Regalbuto and J.-P. Pirard, *Catal. Today*, 2010, **150**, 119–127.
137 X. Hao, S. Barnes and J. R. Regalbuto, *J. Catal.*, 2011, **279**, 48–65.
138 Y. Hong, S. Venkateshalu, S. Jeong, G. M. Tomboc, J. Jo, J. Park and K. Lee, *Bull. Korean Chem. Soc.*, 2022, **44**, 4–22.
139 T. Zhang, A. G. Walsh, J. Yu and P. Zhang, *Chem. Soc. Rev.*, 2021, **50**, 569–588.
140 G. Zhou, Y. Dong and D. He, *Appl. Surf. Sci.*, 2018, **456**, 1004–1013.
141 Y. Peng, Z. Geng, S. Zhao, L. Wang, H. Li, X. Wang, X. Zheng, J. Zhu, Z. Li, R. Si and J. Zeng, *Nano Lett.*, 2018, **18**, 3785–3791.
142 X. Zhang, G. Cui, H. Feng, L. Chen, H. Wang, B. Wang, X. Zhang, L. Zheng, S. Hong and M. Wei, *Nat. Commun.*, 2019, **10**, 5812.
143 X. Xu, Q. Wang, L. Xie, Y. Liu, D. Li, J. Feng and X. Duan, *AIChE J.*, 2023, **69**, e17935.
144 G. Chen, X. Zhu, R. Chen, Q. Liao, D. Ye, B. Zhang, H. Feng, J. Liu, M. Liu and K. Wang, *Appl. Catal., A*, 2019, **575**, 238–245.
145 X. Fu, J. Liu, S. Kanchanakungwankul, X. Hu, Q. Yue, D. G. Truhlar, J. T. Hupp and Y. Kang, *Nano Lett.*, 2021, **21**, 5620–5626.
146 G. Giannakakis, M. Flytzani-Stephanopoulos and E. C. H. Sykes, *Acc. Chem. Res.*, 2019, **52**, 237–247.
147 Y. Zhang, W. Diao, J. R. Monnier and C. T. Williams, *Catal. Sci. Technol.*, 2015, **5**, 4123–4132.
148 L. Zhang, Y. Luo, H. Huang, H. Zhang, Y. Wang and Y. Wang, *J. Alloys Compd.*, 2022, **929**, 167283.
149 M. T. Schaal, A. C. Pickerell, C. T. Williams and J. R. Monnier, *J. Catal.*, 2008, **254**, 131–143.
150 S. S. Djokić, in *Modern Aspects of Electrochemistry*, ed. B. E. Conway and R. E. White, Springer US, Boston, MA, 2002, pp. 51–133, DOI: **10.1007/0-306-47604-5_2**.
151 A. Wongkaew, Y. Zhang, J. M. M. Tengco, D. A. Blom, P. Sivasubramanian, P. T. Fanson, J. R. Regalbuto and J. R. Monnier, *Appl. Catal., B*, 2016, **188**, 367–375.

152 B. Pongthawornsakun, N. Wimonsupakit and J. Panpranot, *J. Chem. Sci.*, 2017, **129**, 1721–1734.
153 G. Tate, A. Kenvin, W. Diao and J. R. Monnier, *Catal. Today*, 2019, **334**, 113–121.
154 I. Ohno, O. Wakabayashi and S. Haruyama, *J. Electrochem. Soc.*, 1985, **132**, 2323.
155 B. D. Barker, *Surf. Technol.*, 1981, **12**, 77–88.
156 M. Parizad, A. P. Wong, A. C. Reber, J. M. M. Tengco, S. G. Karakalos, S. N. Khanna, J. R. Regalbuto and J. R. Monnier, *ACS Catal.*, 2020, **10**, 13352–13363.
157 A. Genest, J. Silvestre-Albero, W. Q. Li, N. Rosch and G. Rupprechter, *Nat. Commun.*, 2021, **12**, 6098.
158 J. Zhu, G. Zhang, W. Li, X. Zhang, F. Ding, C. Song and X. Guo, *ACS Catal.*, 2020, **10**, 7424–7433.
159 C. Wei, H. Ding, Z. Zhang, F. Lin, Y. Xu and W. Pan, *Int. J. Hydrogen Energy*, 2024, **58**, 872–891.
160 G. Totarella, J. W. de Rijk, L. Delannoy and P. E. de Jongh, *ChemCatChem*, 2022, **14**, e202200348.
161 L. Peng, B. Jurca, A. Primo, A. Gordillo, V. I. Parvulescu and H. García, *iScience*, 2022, **25**, 104252.
162 L. Wang, L. Wang, X. Meng and F. S. Xiao, *Adv. Mater.*, 2019, **31**, e1901905.
163 J. Liu, M. B. Uhlman, M. M. Montemore, A. Trimpalis, G. Giannakakis, J. Shan, S. Cao, R. T. Hannagan, E. C. H. Sykes and M. Flytzani-Stephanopoulos, *ACS Catal.*, 2019, **9**, 8757–8765.
164 S.-M. Hwang, S. J. Han, H.-G. Park, H. Lee, K. An, K.-W. Jun and S. K. Kim, *ACS Catal.*, 2021, **11**, 2267–2278.
165 Y. Cao, H. Zhang, S. Ji, Z. Sui, Z. Jiang, D. Wang, F. Zaera, X. Zhou, X. Duan and Y. Li, *Angew. Chem., Int. Ed.*, 2020, **59**, 11647–11652.
166 S. Shao, Y. Yang, K. Sun, S. Yang, A. Li, F. Yang, X. Luo, S. Hao and Y. Ke, *ACS Catal.*, 2021, **11**, 12146–12158.
167 Q. Feng, S. Zhao, Y. Wang, J. Dong, W. Chen, D. He, D. Wang, J. Yang, Y. Zhu, H. Zhu, L. Gu, Z. Li, Y. Liu, R. Yu, J. Li and Y. Li, *J. Am. Chem. Soc.*, 2017, **139**, 7294–7301.
168 J. Fu, J. Dong, R. Si, K. Sun, J. Zhang, M. Li, N. Yu, B. Zhang, M. G. Humphrey, Q. Fu and J. Huang, *ACS Catal.*, 2021, **11**, 1952–1961.
169 R. Gao, J. Xu, J. Wang, J. Lim, C. Peng, L. Pan, X. Zhang, H. Yang and J. J. Zou, *J. Am. Chem. Soc.*, 2022, **144**, 573–581.
170 W. Liu, H. Feng, Y. Yang, Y. Niu, L. Wang, P. Yin, S. Hong, B. Zhang, X. Zhang and M. Wei, *Nat. Commun.*, 2022, **13**, 3188.
171 F. R. Lucci, J. Liu, M. D. Marcinkowski, M. Yang, L. F. Allard, M. Flytzani-Stephanopoulos and E. C. Sykes, *Nat. Commun.*, 2015, **6**, 8550.
172 H. Liu, P. Zhu, D. Yang, C. Zhong, J. Li, X. Liang, L. Wang, H. Yin, D. Wang and Y. Li, *J. Am. Chem. Soc.*, 2024, **146**, 2132–2140.
173 D. Sun, Q. Bi, M. Deng, B. Jia and F. Huang, *Chem. Commun.*, 2021, **57**, 5670–5673.
174 Z. Li, M. Hu, J. Liu, W. Wang, Y. Li, W. Fan, Y. Gong, J. Yao, P. Wang, M. He and Y. Li, *Nano Res.*, 2021, **15**, 1983–1992.
175 S. Tian, B. Wang, W. Gong, Z. He, Q. Xu, W. Chen, Q. Zhang, Y. Zhu, J. Yang, Q. Fu, C. Chen, Y. Bu, L. Gu, X. Sun, H. Zhao, D. Wang and Y. Li, *Nat. Commun.*, 2021, **12**, 3181.
176 G. X. Pei, X. Y. Liu, A. Wang, A. F. Lee, M. A. Isaacs, L. Li, X. Pan, X. Yang, X. Wang, Z. Tai, K. Wilson and T. Zhang, *ACS Catal.*, 2015, **5**, 3717–3725.
177 Y. Wang, L. Cao, N. J. Libretto, X. Li, C. Li, Y. Wan, C. He, J. Lee, J. Gregg, H. Zong, D. Su, J. T. Miller, T. Mueller and C. Wang, *J. Am. Chem. Soc.*, 2019, **141**, 16635–16642.
178 Y. Zhang, J. Li, J. Cai, L. Yang, T. Zhang, J. Lin, X. Wang, C. Chen, L. Zheng, C.-t. Au, B. Yang and L. Jiang, *ACS Catal.*, 2021, **11**, 4430–4440.
179 L. Zhu, Y. Sun, H. Zhu, G. Chai, Z. Yang, C. Shang, H. Ye, B. H. Chen, A. Kroner and Z. Guo, *ACS Catal.*, 2022, **12**, 8104–8115.
180 T. Zhang, P. Zheng, F. Gu, W. Xu, W. Chen, T. Zhu, Y.-F. Han, G. Xu, Z. Zhong and F. Su, *Appl. Catal., B*, 2023, **323**, 122190.
181 X. Song, F. Shao, Z. Zhao, X. Li, Z. Wei and J. Wang, *ACS Catal.*, 2022, **12**, 14846–14855.
182 L. Zhang, G. Meng, W. Zhang, X. Li, Z. Zhang, M. Yang, Y. Wu, D. Wang and Y. Li, *ACS Catal.*, 2023, **13**, 2268–2276.
183 Q. Shen, H. Jin, P. Li, X. Yu, L. Zheng, W. Song and C. Cao, *Nano Res.*, 2022, **15**, 5024–5031.
184 L. Kuai, Z. Chen, S. Liu, E. Kan, N. Yu, Y. Ren, C. Fang, X. Li, Y. Li and B. Geng, *Nat. Commun.*, 2020, **11**, 48.
185 B. Qiao, A. Wang, X. Yang, L. F. Allard, Z. Jiang, Y. Cui, J. Liu, J. Li and T. Zhang, *Nat. Chem.*, 2011, **3**, 634–641.
186 L. Liu and A. Corma, *Chem. Rev.*, 2018, **118**, 4981–5079.
187 F. Yang and W. Xu, *J. Mater. Chem. A*, 2022, **10**, 5673–5698.
188 W. Gao, S. Liu, G. Sun, C. Zhang and Y. Pan, *Small*, 2023, **19**, e2300956.
189 R. T. Hannagan, G. Giannakakis, M. Flytzani-Stephanopoulos and E. C. H. Sykes, *Chem. Rev.*, 2020, **120**, 12044–12088.
190 X. Cai, G. Li, W. Hu and Y. Zhu, *ACS Catal.*, 2022, **12**, 10638–10653.
191 Y. Li, J. Wei, N. Cui, J. Li, M. Xu, G. Pan, Z. Jiang, X. Cui, X. Niu and J. Li, *Adv. Funct. Mater.*, 2023, **33**, 2300639.
192 M. Hu, S. Zhao, S. Liu, C. Chen, W. Chen, W. Zhu, C. Liang, W. C. Cheong, Y. Wang, Y. Yu, Q. Peng, K. Zhou, J. Li and Y. Li, *Adv. Mater.*, 2018, e1801878, DOI: **10.1002/adma.201801878**.
193 S. Chai, D. Gao, J. Xia, Y. Yang and X. Wang, *ChemCatChem*, 2023, **15**, e202300217.
194 M. J. Islam, M. Granollers Mesa, A. Osatiashtiani, J. C. Manayil, M. A. Isaacs, M. J. Taylor, S. Tsatsos and G. Kyriakou, *Appl. Catal., B*, 2021, **299**, 120652.
195 M. Zhong, J. Zhao, Y. Fang, D. Wu, L. Zhang, C. Du, S. Liu, S. Yang, S. Wan, Y. Jiang, J. Huang and H. Xiong, *Appl. Catal., A*, 2023, **662**, 119288.
196 M. Boronat, A. Leyva-Pérez and A. Corma, *Acc. Chem. Res.*, 2014, **47**, 834–844.
197 D. Buceta, Y. Piñeiro, C. Vázquez-Vázquez, J. Rivas and M. A. López-Quintela, *Catalysts*, 2014, **4**, 356–374.
198 X. Cai, X. Sui, J. Y. Xu, A. C. Tang, X. Liu, M. Y. Chen and Y. Zhu, *CCS Chem.*, 2021, **3**, 408–420.

199 R. Zhang, M. Peng, L. Ling and B. Wang, *Chem. Eng. Sci.*, 2019, **199**, 64–78.
200 H. Liu, H. Rong and J. Zhang, *ChemSusChem*, 2022, **15**, e202200498.
201 X. Yang, L. Xu and Y. Li, *Coord. Chem. Rev.*, 2024, **516**, 214651.
202 C. Chu, D. Huang, S. Gupta, S. Weon, J. Niu, E. Stavitski, C. Muhich and J. H. Kim, *Nat. Commun.*, 2021, **12**, 5179.
203 C. Rivera-Cárcamo, I. C. Gerber, I. del Rosal, B. Guicheret, R. Castro Contreras, L. Vanoye, A. Favre-Réguillon, B. F. Machado, J. Audevard, C. de Bellefon, R. Philippe and P. Serp, *Catal. Sci. Technol.*, 2021, **11**, 984–999.
204 C. Y. Regalado Vera, N. Manavi, Z. Zhou, L.-C. Wang, W. Diao, S. Karakalos, B. Liu, K. J. Stowers, M. Zhou, H. Luo and D. Ding, *Chem. Eng. J.*, 2021, **426**, 131767.
205 M. S. Frei, C. Mondelli, A. Cesarini, F. Krumeich, R. Hauert, J. A. Stewart, D. Curulla Ferré and J. Pérez-Ramírez, *ACS Catal.*, 2019, **10**, 1133–1145.
206 N. Hashimoto, K. Mori, K. Asahara, S. Shibata, H. Jida, Y. Kuwahara and H. Yamashita, *Langmuir*, 2021, **37**, 5376–5384.
207 T. W. van Deelen, C. Hernández Mejía and K. P. de Jong, *Nat. Catal.*, 2019, **2**, 955–970.
208 H. Wang, L. Wang and F.-S. Xiao, *Sci. China:Chem.*, 2022, **65**, 2051–2057.
209 J. Zecevic, G. Vanbutsele, K. P. de Jong and J. A. Martens, *Nature*, 2015, **528**, 245–248.
210 Y. Li, Y. Zhang, K. Qian and W. Huang, *ACS Catal.*, 2022, **12**, 1268–1287.
211 Q. Fang, H. Du, X. Zhang, Y. Ding and Z. C. Zhang, *ACS Catal.*, 2024, **14**, 5047–5063.
212 C. J. Breckner, K. Zhu, M. Wang, G. Zhang, C. W. Li and J. T. Miller, *Catal. Sci. Technol.*, 2023, **13**, 157–169.
213 X. Yuan, T. Pu, M. Gu, M. Zhu and J. Xu, *ACS Catal.*, 2021, **11**, 11966–11972.
214 F. Lu, S. Zhou, S. Li, H. Jiang, B. He, J. Qi, Y. Zhang, X. Liu, J. Xu, Y. Li, X. Liu and L. Chen, *J. Phys. Chem. C*, 2021, **125**, 23205–23211.
215 H. Xin, L. Lin, R. Li, D. Li, T. Song, R. Mu, Q. Fu and X. Bao, *J. Am. Chem. Soc.*, 2022, **144**, 4874–4882.
216 X. Bian, D. Zhou, X. Zhang, S. Han, S. Liu, W. Zhao, Y. Li and W. Shen, *Catal. Lett.*, 2024, **154**, 5584–5592.
217 F. Long, S. Wu, Y. Chen, X. Cao, J. Zhao, P. Liu, J. Jiang, X. Zhang and J. Xu, *Chem. Eng. J.*, 2023, **464**, 145987.
218 Y. Shao, M. Kosari, S. Xi and H. C. Zeng, *ACS Catal.*, 2022, **12**, 5750–5765.
219 M.-S. Kim, S.-H. Chung, C.-J. Yoo, M. S. Lee, I.-H. Cho, D.-W. Lee and K.-Y. Lee, *Appl. Catal., B*, 2013, **142–143**, 354–361.
220 Y. Shu, H. C. Chan, L. Xie, Z. Shi, Y. Tang and Q. Gao, *ChemCatChem*, 2017, **9**, 4199–4205.
221 T. Chen, Z. Shi, G. Zhang, H. C. Chan, Y. Shu, Q. Gao and Y. Tang, *ACS Appl. Mater. Interfaces*, 2018, **10**, 42475–42483.
222 D. Zhang, W. Yu, Z. Li, Z. Wang, B. Yin, X. Liu, J. Shen, C. Yang, W. Yan and X. Jin, *Biomass Bioenergy*, 2022, **163**, 105503.
223 Q. Sun, X. Fu, R. Si, C. H. Wang and N. Yan, *ChemCatChem*, 2019, **11**, 5093–5097.
224 M. Luneau, T. Shirman, A. C. Foucher, K. Duanmu, D. M. A. Verbart, P. Sautet, E. A. Stach, J. Aizenberg, R. J. Madix and C. M. Friend, *ACS Catal.*, 2019, **10**, 441–450.
225 X. Zhang, Y. Fan, E. You, Z. Li, Y. Dong, L. Chen, Y. Yang, Z. Xie, Q. Kuang and L. Zheng, *Nano Energy*, 2021, **84**, 105950.
226 Q. Sun, B. W. J. Chen, N. Wang, Q. He, A. Chang, C. M. Yang, H. Asakura, T. Tanaka, M. J. Hulsey, C. H. Wang, J. Yu and N. Yan, *Angew. Chem., Int. Ed.*, 2020, **59**, 20183–20191.
227 K. W. Golub, T. P. Sulmonetti, L. A. Darunte, M. S. Shealy and C. W. Jones, *ACS Appl. Nano Mater.*, 2019, **2**, 6040–6056.
228 S. J. Tauster, S. C. Fung and R. L. Garten, *J. Am. Chem. Soc.*, 1978, **100**, 170–175.
229 Y. Liu, X. Li, Q. Cheng, Y. Tian, Y. Zhang, T. Ding, S. Song, K. Song and X. Li, *ACS Catal.*, 2024, **14**, 10365–10375.
230 M. Xu, Y. Jeon, A. Naden, H. Kim, G. Kerherve, D. J. Payne, Y. G. Shul and J. T. S. Irvine, *Nat. Commun.*, 2024, **15**, 4007.
231 X. Zhang, W. Shi, Y. Li, W. Zhao, S. Han and W. Shen, *ACS Catal.*, 2023, **13**, 4030–4041.
232 A. Beck, X. Huang, L. Artiglia, M. Zabilskiy, X. Wang, P. Rzepka, D. Palagin, M. G. Willinger and J. A. van Bokhoven, *Nat. Commun.*, 2020, **11**, 3220.
233 H. Wang, L. Wang, D. Lin, X. Feng, Y. Niu, B. Zhang and F.-S. Xiao, *Nat. Catal.*, 2021, **4**, 418–424.
234 C.-J. Pan, M.-C. Tsai, W.-N. Su, J. Rick, N. G. Akalework, A. K. Agegnehu, S.-Y. Cheng and B.-J. Hwang, *J. Taiwan Inst. Chem. Eng.*, 2017, **74**, 154–186.
235 S. D. Le and S. Nishimura, *Appl. Catal., B*, 2021, **282**, 119619.
236 R. Gubo, C. M. Yim, M. Allan, C. L. Pang, A. Berko and G. Thornton, *Top. Catal.*, 2018, **61**, 308–317.
237 Y. Guo, S. Mei, K. Yuan, D.-J. Wang, H.-C. Liu, C.-H. Yan and Y.-W. Zhang, *ACS Catal.*, 2018, **8**, 6203–6215.
238 A. M. Silva, M. A. Morales, E. M. Baggio-Saitovitch, E. Jordão and M. A. Fraga, *Appl. Catal., A*, 2009, **353**, 101–106.
239 M. Xu, S. He, H. Chen, G. Cui, L. Zheng, B. Wang and M. Wei, *ACS Catal.*, 2017, **7**, 7600–7609.
240 F. Lin, X. Jiang, N. Boreriboon, Z. Wang, C. Song and K. Cen, *Appl. Catal., A*, 2019, **585**, 117210.
241 R. Hou, M. D. Porosoff, J. G. Chen and T. Wang, *Appl. Catal., A*, 2015, **490**, 17–23.
242 K. R. G. Lim, M. Aizenberg and J. Aizenberg, *J. Am. Chem. Soc.*, 2024, **146**, 22103–22121.
243 X. Li, X. I. Pereira-Hernandez, Y. Chen, J. Xu, J. Zhao, C. W. Pao, C. Y. Fang, J. Zeng, Y. Wang, B. C. Gates and J. Liu, *Nature*, 2022, **611**, 284–288.
244 Z. Zhang, C. Du, H. Li, J. Hu, F. Yang, J. Huang, S. Hu, W.-X. Li and H. Xiong, *Appl. Catal., B*, 2024, **358**, 124334.
245 S. Liu, Y. Li, X. Yu, S. Han, Y. Zhou, Y. Yang, H. Zhang, Z. Jiang, C. Zhu, W. X. Li, C. Woll, Y. Wang and W. Shen, *Nat. Commun.*, 2022, **13**, 4559.
246 A. Poungsombate, T. Imyen, P. Dittanet, B. Embley and P. Kongkachuichay, *J. Taiwan Inst. Chem. Eng.*, 2017, **80**, 16–24.
247 Y. Qin, L. Chen, L. Ge, Y. Zhu, W. Li, X. Cao, T. Wang, J. Li, W. Han and X. Chen, *Chem. Eng. Sci.*, 2025, **304**, 120990.

248 L. Li, W. Yang, Q. Yang, Q. Guan, J. Lu, S.-H. Yu and H.-L. Jiang, *ACS Catal.*, 2020, **10**, 7753–7762.
249 K. S. Park, Z. Ni, A. P. Côté, J. Y. Choi, R. Huang, F. J. Uribe-Romo, H. K. Chae, M. O'Keeffe and O. M. Yaghi, *Proc. Natl. Acad. Sci. U. S. A.*, 2006, **103**, 10186–10191.
250 M. Cargnello, C. Chen, B. T. Diroll, V. V. T. Doan-Nguyen, R. J. Gorte and C. B. Murray, *J. Am. Chem. Soc.*, 2015, **137**, 6906–6911.
251 M. Duan, J. Yu, J. Meng, B. Zhu, Y. Wang and Y. Gao, *Angew. Chem., Int. Ed.*, 2018, **57**, 6464–6469.
252 Z. Li, Y. Cui, Z. Wu, C. Milligan, L. Zhou, G. Mitchell, B. Xu, E. Shi, J. T. Miller, F. H. Ribeiro and Y. Wu, *Nat. Catal.*, 2018, **1**, 349–355.
253 W. Yuan, B. Zhu, K. Fang, X.-Y. Li, T. W. Hansen, Y. Ou, H. Yang, J. B. Wagner, Y. Gao, Y. Wang and Z. Zhang, *Science*, 2021, **371**, 517–521.